MINISTRY OF EDUCATION
TECHNICAL UNIVERSITY
OF CLUJ-NAPOCA, ROMANIA
FACULTY OF ELECTRICAL ENGINEERING

PhD THESIS

Multi-Physical Mathematical and Machine Learning Models for Electrical Motors Design and Performance Prediction

PhD Student:
Maria Raluca RAIA

PhD Supervisor:
Prof. Dr. Eng. Claudia MARȚIȘ

Examination committee:
Chair: Prof. Eng. **Claudia Păcurar**, PhD – Technical University of Cluj-Napoca;
PhD Supervisor: Prof. Eng. **Claudia Steluța Marțiș**, PhD – Technical University of Cluj-Napoca;
Members:
-Prof. Eng. **Nicolae Muntean**, PhD – Politehnica University Timisoara;
-Prof. Eng. **Ciprian Șorândaru**, PhD – Politehnica University Timisoara;
-Prof. Eng. **Lorand Szabo**, PhD – Technical University of Cluj-Napoca.

– Cluj-Napoca –
2023

str. Memorandumului nr. 28, 400114 Cluj-Napoca, România
tel. +40-264-401200, fax +40-264-592055, secretariat tel. +40-264-202209, fax +40-264-202280
www.utcluj.ro

ACKNOWLEDGMENTS

Over the past few years, since the beginning of my PhD journey, I have found myself thinking several times about this moment when I am close to the finish line with my thesis. I wondered not only what the thesis would look like, but especially the person I would become at the end of my PhD. Will I have become wiser, will I have found new skills, will I have enjoyed this journey, will I have become a better version of myself? If I look back at the person I was when I started this journey, I would answer yes to all the above questions, but they materialized in a totally unexpected way. This is mostly because of all the people I have met or worked with over the years who have shaped my character, from whom I have had the opportunity to learn and grow. I knew from the beginning that I would develop both professionally and personally, and looking back, these years were the most fruitful years of my professional life and the best years of my personal life.

All these would have not be real without my mentor and promoter, Professor Claudia MARTIS. She guided me, helped me grow by putting me in contact with the right people, gave shape to my professional life and I can't thank her more for that. I owe her a depth of gratitude for seeing the potential in me and believing in me.

I want to personally thank my thesis advisors and industrial supervisors. Dr. Fabien CHAUVICOURT, thank you for teaching me the importance of rigor, for your availability on discussing on my work, for your patience and for your valuable help whenever I needed it most. My sincere thanks also go to Sebastian CICEO who always pushed and motivated me to go beyond my limits, for sharing all the theoretical and practical knowledge and for making the work environment a fun one. It has been a pleasure working with both of you and I am looking forward for our future collaborations.

At the same time, I want to express my gratitude to Dr. Cristi IRMIA, the General Manager at Siemens Industry Software Romania, for his unconditional support during my last year of PhD and the possibility to work and grow within the Research and Development Group. A special thanks goes to Dr. Mircea RUBA. Thank you for your constant availability, for your help and support during my doctoral studies. I would like to express my thanks to Dr. Calin HUSAR, from Siemens Industry Software Romania, for his friendship and for the help offered during this journey.

I am also grateful for the people I met in university and company. To the people in Siemens, Leuven: Flavia, JP, Davide, Domenico, Ludovico, Bernardo, thank you for your friendship and wonderful memories. To all the people from the Engineering Services (ES) from Siemens Belgium and Research and Development from Siemens Brasov am grateful for the technical support.

To my dear friends, Teodora, Anamaria, Madalina. I am grateful to have you in my life and I want to thank you for being always by my side and for our wonderful memories together.

În final, vreau să le mulţumesc celor mai importante persoane din viaţa mea, celor din familia mea. Liniştea şi siguranţa pe care voi mi le-aţi dăruit constant m-au ajutat să devin persoana de astăzi.

Părinţilor mei, Maria si Constantin, le mulţumesc pentru iubirea infinită, pentru grija si devotamentul vostru şi pentru bucuria şi tihna pe care am simţit-o mereu în familie.

Surorilor mele, Diana şi Lucia, şi Pr. Mihai, vă mulţumesc pentru grija şi iubirea voastră. Mereu v-am avut pe voi drept exemplu.

Verişoarelor mele, Irina şi Simona, si verisorilor mei, Ştefan şi Dragoş, pentru că ati fost prezenţi cand am avut nevoie mai mare şi pentru discuţiile amuzante cu voi. Sunt extrem de recunoscatoare ca va am in viata mea!

Şi celor mai mici: Alexandru, Anastasia, Antonia, Nectaria, vă iubesc! Datorită vouă, am avut şansa să retrăiesc bucuria copilăriei şi uitându-mă la cum creşteţi, îmi reamintesc mereu că orice lucru bun în viaţă se dobândeşte in timp.

Cluj-Napoca, 2023 Maria Raluca RAIA

Contents

ABBREVIATIONS

PMSM	Permanent Magnet Synchronous Machine
IPMSM	Interior Permanent Magnet Synchronous Machines
PM	Permanent Magnet
ICE	Internal Combustion Engines
ADAS	Advanced Driver Assistance Systems
NVH	Noise, Vibration and Harshness
EV	Electrical Vehicle
FEA	Finite Element Analysis
EMF	Electromotive Force
LHS	Latin Hypercube Sampling
LUT	Lookup Table
ROM	Reduced Order Model
AI	Artificial Intelligence
ML	Machine Learning
ANN	Artificial Neural Network
DOF	Degree of Freedom
DOE	Design of Experiments
FFT	Fast Fourier Transform
SVR	Support Vector Regression
GBR	Gradient Boosting Regressor
GPR	Gaussian Process Regressor
LSTM	Long short-term memory network
SOM	Slot Openening Modulation
IoT	Internet of Things
MSE	Mean Square Error
FPM	Frozen Permeability Method
LMBPA	Levenberg-Marquardt Backpropagation Algorithm

1. Introduction

1.1 Research context

In the light of the increasing concerns about global warming, the automotive industry is facing stringent limits for pollution, gas emission and rigorous market demands. Therefore, greener technologies with increased performances and higher efficiency are developed as an alternative solution to the traditional ones. The classical Internal Combustion Engines (ICE) are now replaced by their electrical motors, while mechanical solutions used for auxiliary system are substituted with electrical ones to improve not only the efficiency, but also the maintenance process. Staring with early 2000s, the hydraulic power steering was replaced with the electric power steering that now is a standard for vehicles [1]. The newly developed vehicle technologies include Advanced Driver Assistance Systems (ADAS) that assist drivers during driving for a safer operation. This way, the collisions are avoided, the system is actively controlled to offer a safer and comfortable driving. For these applications, the electrical motors need to meet demanding requirements regarding Noise, Vibration and Harshness (NVH) levels. Compared with ICE, an electrical motor produces less noise, but the noise is perceived by human ear as annoying, due to its high frequency band. If this is added on top of electromagnetic, thermal and structural requirements, the process of designing an electrical motor becomes a challenge, especially as the multi-physical requirements come in conflict and an optimal trade-off between them must be found for a specific application.

Traditionally, the electrical motors are designed within different departments that deal with only one physics. The process is sequential and starts with the optimisation of electromagnetic targets, then the stress and thermal aspects are analysed in order to find an appropriate cooling system, leaving the analysis of structural performances at the end (i.e., in the late stage design). This leads to reduced possibilities to improve the NVH characteristics without affecting the electromagnetic targets. Usually, a trade-off between the two domains is determined. Another aspect that must be taken into account is the collaboration between experts coming from multiple departments. The design process passes through each department in an iterative way until an optimum configuration is reached, making it time and resource consuming.

Another approach is to bring the optimisation of all characteristics of an electrical motor in the early design stage. In this way, the traditional sequential process is transformed into a simultaneous workflow, where all the targets coming from the multi-physical domain have the same de-

sign space and a global objective function can be imposed. The analysis based on finite element (FE) method is one of the most popular procedure to analyse the performances of electrical machines. Even if the computational power of the new generation of computers is augmented and parallelization methods are employed, the high-fidelity models based on FE method are time consuming, leading to increased computational cost of optimisation process, especially as both 2D and 3D FE analysis are conducted to determine the multi-domain characteristics. This issue is overcame by using mathematical analytical methods or surrogate models to reduce the time costs of the design process. In this way, the optimisation process can become more complex, including multi-domain objectives, while keeping an acceptable computational costs. Thus, by including the multi-domain analysis even in the early design stage, the designer can identify the system's performances, robustness and find an optimal solution.

This work mainly focuses on developing mathematical and data-driven methods that ease and improves the design process of electromagnetic machines. Analytical, semi-analytical or FE methods are employed to generate data and their accuracy and feasibility is discussed. Geometric parametric models are used to evaluate the multi-physical performances of thousands electrical machines designs and build multi-attribute machine learning model.

1.2 Objectives of the thesis

The main objective of this thesis is to propose solutions to predict the characteristics of electrical machines coming from different physics involved and ease and improve the design process. Surrogate models are introduced in the designing phase of an electrical motor, known as an intricated problem due to the highly non-linear nature of the system caused by the saturation of iron in presence of high magnetic field strength values and to the requirements coming from different physics that compete against each other. The proposed methods (i.e., numerical, mathematical and machine learning based) must be evaluated in the context of decision making process during design phases and optimization stages. In light of these requirements, not only the accuracy is crucial, but also the computational time cost. Experimental test are used as a validation for the developed models. For surrogate models, the building process includes data acquisition, surrogate problem evaluation and model development.

1.3 Original Contributions

The author main contributions to the thesis subject are already publicly available by the work shared within international events, such as peer reviewed conferences publications and presentations, journal articles and book chapters. The research works are either already published and publicly available or in the process of publication. More details about the published papers can be found in the Section "List of Publications".

The author main original contributions are:

- The development of an automated multi-physics modelling workflow that allows a fast prediction of the electrical machine characteristics and a fast multi-objective optimization.
- Introduction of special effects that are not included in the classical analytical method for displacement computation, an evaluation of the error between the analytical and numerical methods.
- The improvement of the NVH characteristics of the machine under study by introduction of asymmetry on the slot opening geometry.
- A solution to detect the faults during the operation of an industrial system.

1.4 Structure of the thesis

The thesis is structured in three main parts. In the first part, the multi-physical phenomena that arises during the operation of electrical machines are described. At the same time, the best methods, numerical, analytical and data-driven, are discussed and compared. The second part is dedicated to the design and optimisation of electrical motors by taking into account the multi-physical characteristics using mathematical and machine learning methods. The modeling approaches are described and validated experimentally and the most important aspects that must be considered when designing an electrical motor are highlighted. An analysis of different machine learning algorithms is conducted in order to determine the best practices for multi-attributes predictions. Different methods to reduce the noise vibration and harshness of electrical machines are discussed in the end of second part. The third and last part of the thesis is dedicated to the modeling at system level of an electrical motor integrated into an industrial system. The prediction of different faults that may occur is introduced in this part.

Chapter 1 introduces the thesis subject within the research context, describes the problem at which the present thesis responds and discuss the main motivation of this work. The main objective of the thesis,

together with the author original contributions are underlined.

The content of **Chapter 2** describes the fundamental aspects that characterize the multi-physical behaviour of electrical machines. At the same time, the main methods used within the modeling and design process are described, together with the particularities of the machine under study. The parametric models of the stator and rotor of the machine under study, in both structural and electromagnetic domains, used for data generation process, are outlined.

Chapter 3 provides the modeling workflow of electrical machines in electromagnetic domain using both mathematical (i.e., numerical) and data driven approaches to build high fidelity reduced order models. The prediction of electromagnetic values using the two methods is discussed and the obtained results compared from accuracy and time cost perspective. The necessity of using the surrogate model for electromagnetic domain is emphasized, while experimental results support the investigations.

Chapter 4 focuses on the structural characteristics prediction of electrical motors. Two methods, the analytical method and the FE based approach, are introduced to compute the structural characteristics (i.e., stator mode-shapes and corresponding eigen-frequencies and stator vibration response). Based on parametric models, the analytical method is compared with the finite-element method, exploring the computational price and accuracy.

Chapter 5 is dedicated to the development of surrogate models able to evaluate multi-physical attributes of electrical machines from input geometrical parameters. Different values, starting from electromagnetic characteristics, going to motor losses and stator core eigen – frequencies, and ending with rotor stress and stator forced response, are investigated with the goal of developing machine learning models that are used in the early stage design of electrical motors. The last part of this chapter is dedicated to the integration of the developed surrogate models into optimisation loops. The results and the computational time are evaluated, taking as reference the results obtained from the finite element analysis based optimisation method.

Chapter 6 presents a method to decrease the NVH characteristics of electrical motors by performing geometrical design modifications. The motor cross-section geometry is shaped by introducing stator slot opening geometry asymmetry. The initial symmetrical slot opening geometry is adjusted by cutting soft magnetic material on one side of the tooth, while additional material is added on the other side. The improvements of the vibration response is quantified, while monitoring the electromagnetic torque evolution.

Chapter 7 presents the integration of an electrical motor in an industrial system and presents the problem of condition monitoring at system level. A method to perform condition monitoring of an industrial elevator using artificial intelligence and machine learning models by process big data sets is described in this section. The advantages of long Short-Term Memory models predicting failures are discussed.

Chapter 8 draws the final conclusions and proposes new ideas that can be investigated in the future.

2. The multi physical characteristics of electrical machines

Several fundamental aspects are introduced in this chapter in order to characterize and understand the behaviour of electrical machines. An overview of the characteristics coming from multiple domains is given together with the methods and tools needed for multi-physical analysis of electrical motors. In the end of this chapter, the electrical machine considered for this work and the parametrization of the stator and rotor necessary to generate big data for machine learning models are described.

2.1 Fundamentals of Electrical Machines

The rotating electrical motor is an energy converter that transforms electrical energy coming from an external source that can be either (DC or AC) into mechanical energy. The energy is converted in the space between the stationary part (i.e., stator) and the rotating part (i.e., rotor), so called air-gap. The electromagnetic field generated in the air-gap varies and creates radial and tangential forces. The tangential forces produce electromagnetic torque and the radial forces excite the stator and cause air-born NVH.

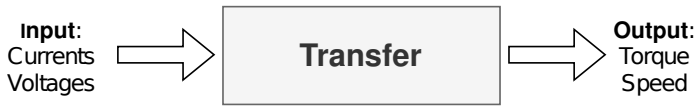

Figure 2.1: Motor operation of an electrical machine explained.

The electrical machines are composed in some main parts: the stator with conductors grouped in windings or with permanent magnets and the rotor with electromagnetic or permanent magnet excitation. Besides that, some components assure protection of the main parts, heat transfer, mechanical support, connection with exterior. An exploded view of a typical PMSM architecture can be identified in Fig. 2.2. The stator and rotor cores are made by a group of thin steel sheets, named laminations, that are pressed, resulting in laminated structures of stator and rotor cores. The shaft supports the rotor and transmits the mechanical energy to the exterior. The rotor is mounted on the bearings, while the housing and the end shields protects the systems, transfers the heat, reduces vibrations.

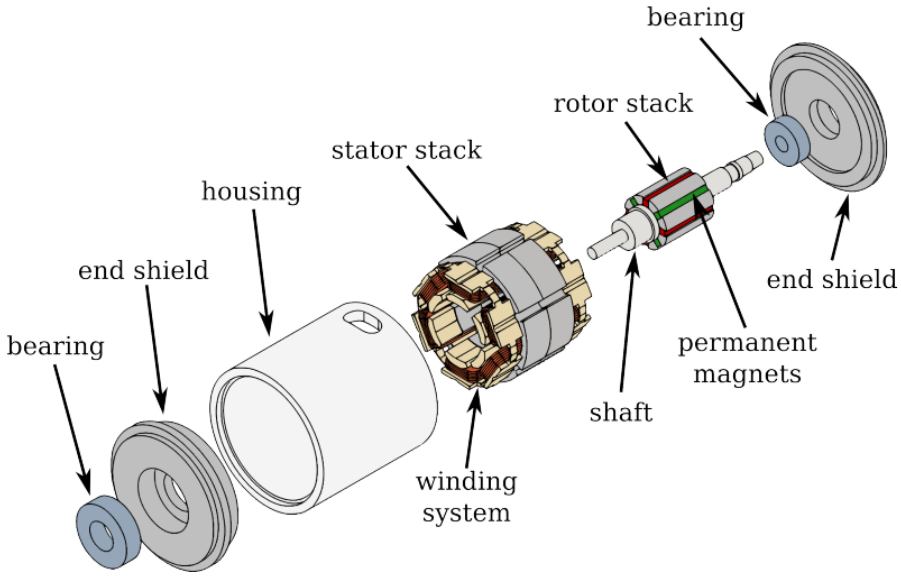

Figure 2.2: Components of a PMSM, exploded view [2]

2.1.1 PMSM Classification

Permanent magnet synchronous motors are three phase ac machines with the stator electromagnetically excited and permanent magnets in the rotor. Because of the field produced in the stator, the rotor tends to align itself with the rotating field. The PMSM can be classified based on the following topics:

- direction of air-gap flux ;
- rotor and stator positions;
- back-EMF waveform;
- position of permanent magnets;
- stator windings distribution;
- stator core configuration.

A schematic classification of PMSMs based on the discussed topics is identified in Fig. 2.3.

2.1.2 Electromagnetic phenomena in electrical machines

Considering a closed path of arbitrary contour placed in a magnetic field, the Ampere law give the connection between the magnetic field

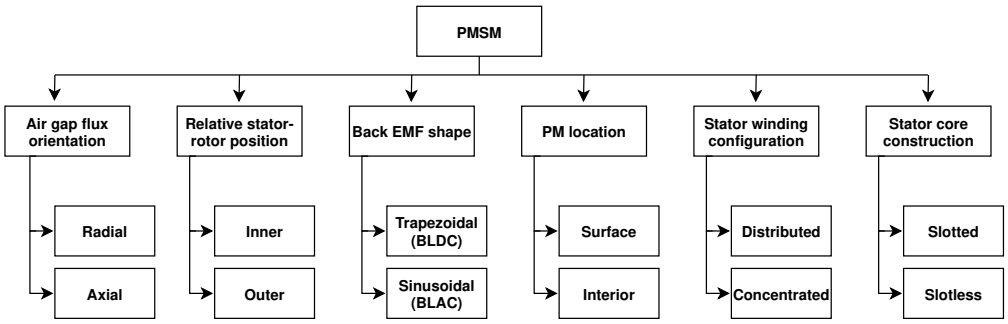

Figure 2.3: Classification of PMSMs.

intensity, H, that appears around a closed path and the sources of the field, the sum of currents enclosed by this path.

$$\oint H\,dl = I \tag{2.1}$$

The effect of H, related to the currents through Ampère's law is the magnetic flux density, B, associated with observable quantities such as force through the Lorentz equation. The expression of B is:

$$B = \mu H, \text{ in tesla(T)} \tag{2.2}$$

For a magnetic material of length l surrounded by a coil containing N turns carrying a current i, and assuming a magnetic field with constant magnitude H, the magneto-motive force mmf is defined as:

$$mmf = Hl \tag{2.3}$$

In order to quantify the amount of magnetic field that passes by a given area in the magnetic core, the magnetic flux (expressed in webber, Wb) is introduced:

$$\Phi = \int B\,dA \tag{2.4}$$

If the area is perpendicular to the field and the magnetic flux is expressed in function of magnetic reluctance, R_e, by the following expression, similar to Ohm's law:

$$\Phi = BA = \mu \frac{mmf}{l} A = \frac{mmf}{R_e} \tag{2.5}$$

The above equation is also known as the law of minimal reluctance. Similar to electric circuits, the flux (corresponding to electrical current)

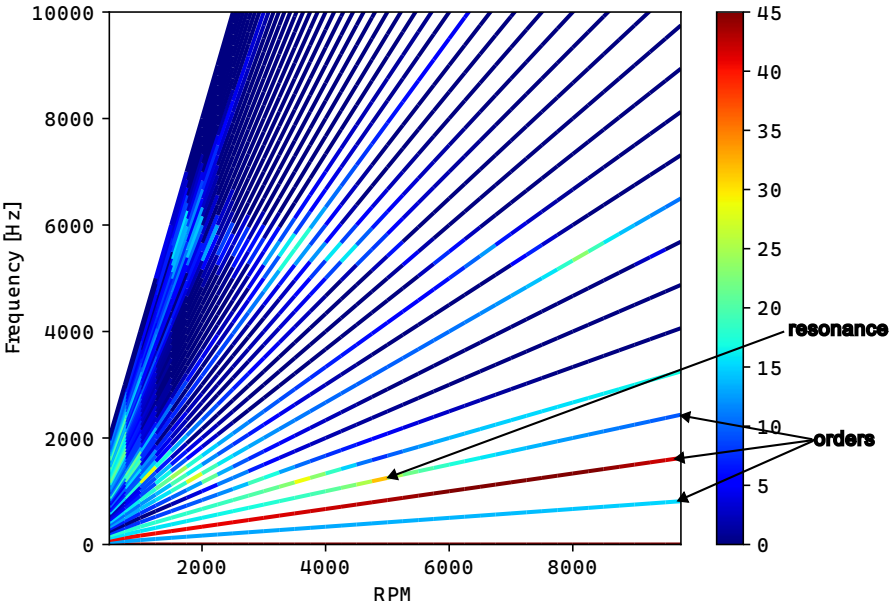

Figure 2.4: Vibration response during run-up.

finds the path with the lowest reluctance (corresponding to electrical resistance).

Now, considering that the magnetic field is kept uniform, with a constant magnitude, B, and that the conductor of length l that carries a current i is located within this field, in a direction perpendicular to B, there will be a force density, F (in N/m^3), exerted on the conductor, perpendicular to both the conductor and the field. This force, called Lorentz Force is given by:

$$F = i(l \times B) \tag{2.6}$$

2.1.3 Sources of Structure Borne Noise

The sources of vibration in an electrical machines come from three different physics domain and determine air – and structure – borne noise:

- electromagnetic sources: the electromagnetic forces located in the air-gap and created by the electromagnetic field. The forces act on the stator teeth, the vibration propagates through the structure and determines air-borne noise.
- mechanical domain sources: cogging torque, torque ripple, components that come in contact, unbalanced rotor. The transmission path is represented by the rotor, bearings and shaft. The propagated

Figure 2.5: Environmental noise levels [3].

displacement causes structure-borne noise. They excite the rotor.

- aerodynamic sources are caused by motor cooling fans that create air flow turbulence while rotating. The intensity of these vibration increase as the rotational speed of the rotor increases.

The electromagnetic noise is characterised by some attributes:

- the orders, represented by the number of times per second when a stator tooth meets a rotor pole. The orders numbers are specific to the pole-slots configuration and they change with the rotational speed.
- resonance frequency, occurring if the exciting frequency matches one of the structure eigen-frequency.
- electronically induced ripples caused by the power electronics, that are not considered in this thesis.

In Fig. 2.4, the vibration response during run-up (i.e., the machine is accelerating) is presented. Here, the oblique lines are representing the orders. The order number is given by the rotational speed multiplied by order number. This way, rotational speed times one is giving order 1, two times rotational speed gives order 2 and so on. The corresponding frequency of each order is expressed as a function of rotational speed n_s in [rpm], the number of rotor pole pairs, p, and the factor that gives the order number, n_o:

$$f_{\text{order}} = \frac{n_s}{60} p\, n_o \tag{2.7}$$

In the same figure, the indicated resonance phenomena occurring at 1200 [Hz] corresponds to the matching between the stator natural frequency corresponding to mode 2 (ovalisation) and the force wave with the same spatial order number.

When designing an electrical motor, the motor manufacturer must take care of the available standards on noise limits. The environmental noise levels are presented in Fig. 2.5. A specific system should not cross the dedicated maximum noise limits.

2.2 Electromagnetic forces computation

The electromagnetic forces and torque production is derived for most of the applications with the help of Maxwell's stress tensor method [4]. In an electrical machine, the flux lines cross the air gap, as it can be depicted in Fig. 2.6 a). The two components, radial and tangential, have different effects. The radial component produces radial forces that excite the structure causing noise and vibrations, whereas the tangential component produces tangential forces that determine electromagnetic torque. The surface force density for one stator tooth is presented in Fig. 2.6 b).

The Maxwell's stress tensor states that in the air-gap, the magnetic field strength creates a stress on a surface placed inside the air-gap. The force produced in the air-gap, F, is derived, according to the Maxwell's stress tensor, using the unit vector, n, that points outside surface S, and $\bar{\sigma}_{\text{Maxwell}}$ is the Maxwell stress tensor, as follows:

$$F = \int_S \bar{\sigma}_{\text{Maxwell}}\, n\, dS \tag{2.8}$$

$$\bar{\sigma}_{\text{Maxwell}} = \frac{1}{\mu_0}\begin{bmatrix} B_r^2 - B^2/2 & B_r B_\theta & B_r B_z \\ B_\theta B_r & B_\theta^2 - B^2/2 & B_\theta B_z \\ B_z B_r & B_z B_\theta & B_z^2 - B^2/2 \end{bmatrix} \tag{2.9}$$

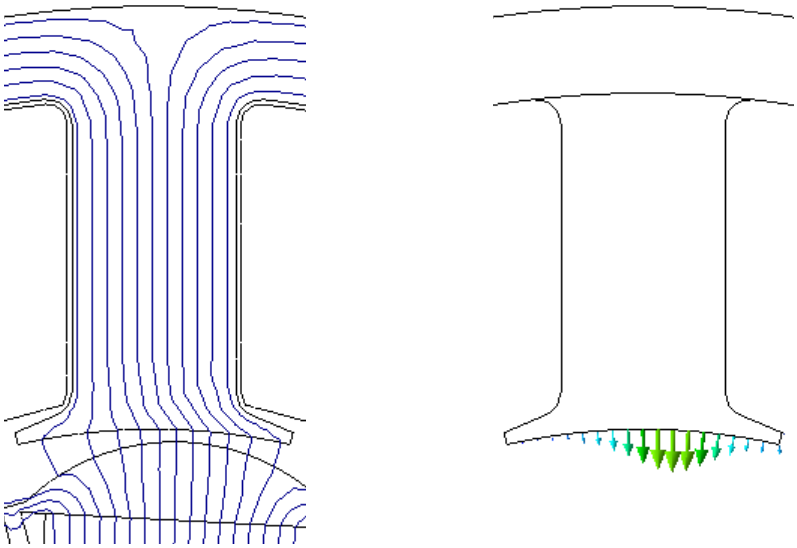

(a) (b)

Figure 2.6: Flux lines for load conditions of a IPMSM (a) and Surface force density expressed in [N/mm^2] (b).

where $B^2 = B_r^2 + B_\theta^2 + B_z$ is expressed using cylindrical coordinates components (r, θ, z). Figure 2.7 shows the surface line integration of the Maxwell's stress tensor.

2.3 Types of losses in electrical machines

The losses computation is an important step when designing and estimating the capabilities of an electrical motor. The machine performances are directly affected by the losses that appear in different parts of the system under analysis. The losses are dissipated through the machine and will create thermal stress on the machine components. The created heat and increased temperature of components can demagnetise the permanent magnets and modify the winding resistivity [5]. The thermal analysis of an electrical motor is a complex process with results that are highly influenced by the design parameters and also by the manufacturing tolerances [6]. Therefore, once the electrical machine losses are correctly estimated, the information about the materials thermal characteristics and the chosen cooling method are available, an analysis of temperature distribution in the interior of an electrical motor can be performed [7].

Analytical methods or FE analysis are the main methods employed for machine losses computation [8]. The main losses source in a PMSM is the stator windings (i.e., stator winding copper loss) [7]. The iron losses

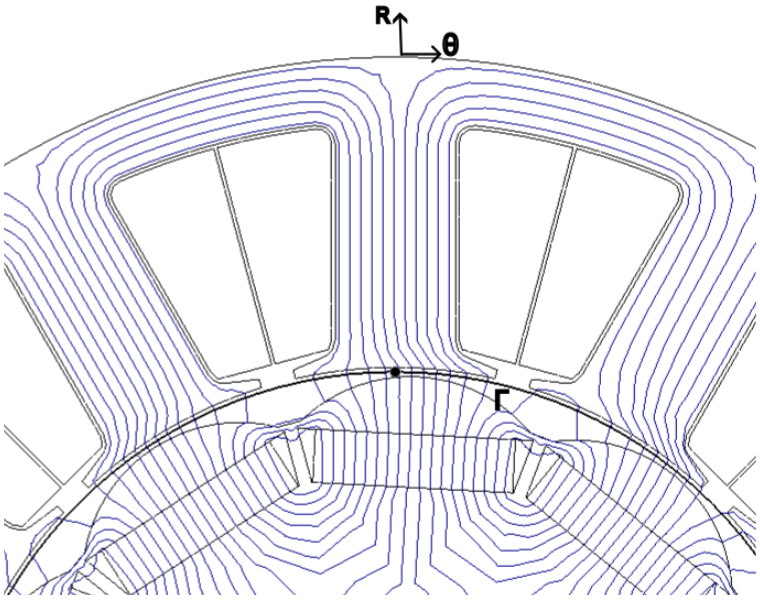

Figure 2.7: Surface line integration of the Maxwell stress tensor.

are derived as the sum of hysteresis, eddy–current and excess losses and have a large share in the over-all machine losses. Iron losses, consisting in hysteresis and eddy current (lamination) losses, are computed in a post-processing step utilising the Steinmetz model. The losses can also be classified based on the parts of the system where they originate from. The losses can come from the winding, the iron, stator back iron, stator teeth, rotor back iron and the magnet. By summing all the losses, the total losses can be computed. This individual classification of losses based on the stator components from which they originate is important, because the flux density is not constant in radial direction and the flux density manifest differently in different components (e.g., stator teeth and stator back iron) [9].

2.3.1 Stator winding losses

The stator copper loss is a value dependent on the stator winding current and resistance and on the environment temperature that affects both the current necessary to achieve the requested torque and the electrical resistivity of the material of the winding. The copper resistivity increases with the rise of temperature:

$$\rho = \rho_{20}[1 + \alpha(T - 20)] \tag{2.10}$$

where $\rho_{20} = 1.724 \times 10^{-8}\Omega$m is the copper resistivity at 20 degrees

and $\alpha = 0.00393/°\text{C}$ is the temperature coefficient. If the winding temperature rises with 50 °C, the resistance increases with 20% [7].

The Joule losses are determined as the square of the rms value of the stator winding current multiplied with the resistance

$$P_{js} = 3R_s I_s^2 \tag{2.11}$$

2.3.2 Stator iron losses

The iron losses consist of static (hysteresis) and dynamic (eddy-current or lamination) losses. Iron losses are approximated by the Steinmetz model that expresses the losses as a function of the frequency f and the magnetic flux density B taken to the power of predetermined exponents [10], [11], [12]:

$$p_{iron} = k_{hy} B^{\beta} f + k_{ec} B^2 f^2 \tag{2.12}$$

where k_{hy} and k_{ec} represent the hysteresis and the eddy current coefficient, f is the frequency of the flux density B and depends on motor speed and β is the Steinmetz constant.

Even if eq. 2.12 doesn't include a separate term for excess losses (i.e., dynamic losses of the Weiss domain that appear in a magnetic material subject to a variable magnetic field), it assumes that these losses cannot be separated from the eddy-current ones [13]. Therefore, k_{ec} is a coefficient that defines both eddy current and excess losses. These coefficients are derived as a constant coefficient [11] or for more accurate results, as a polynomial function of magnetic flux densities [12]. These constants are dependent on the material data sheet properties, on the operating frequencies and lamination thickness.

2.3.3 Tooth iron losses

In eq. 2.12, the magnetic flux density is considered to be sinusoidal. However, the flux density is distorted in the iron and this phenomenon is mainly observed in the stator teeth. For this situation, eq. 2.12 becomes:

$$p_{ec} = \frac{k_{ec}}{2\pi^2} \frac{\omega^2}{2\pi} \int_0^{2\pi} \left(\frac{\partial B}{\partial \theta} \right)^2 d\theta \tag{2.13}$$

It can be observed that only the eddy current losses were considered in the above equation, due to their main contribution to stator losses, as they are influenced by the square of frequency. By arranging the above equation, the final tooth iron losses has the flowing expression [14]:

$$p_{ec} = k_{ec} f^2 \sum B^2 h^2 \tag{2.14}$$

2.4 Electromagnetic Analysis Fundamentals

The electromagnetic evaluation of electrical machines is performed with high precision with the help of magnetic finite element (FE) analysis. The finite element analysis offers a high solution accuracy, for both two – dimensional and three – dimensional analysis, but depending on the model size, it can have high computational time. Due to the increase of the processing capacity of the present computers, 2D FE analysis are fast, but the 3D FE are still time consuming and memory intensive [15]. Therefore, even if the 3D FE analysis show the most accurate results, it cannot be used for complex models or in processes that require a lot of iteration steps, like an optimization routine or design of experiments. Two-dimensional analysis are commonly used to reduce the simulation burden, keeping a high level of accuracy [16], especially for small machines (e.g., steering motor) or traction motors that don't present high end effects [17]. The 2D problem simplification assumes that the model has a planar symmetry (i.e., the magnetic field is considered to be uniform along the z-axis of symmetry), the current density, J, and the magnetic potential, A, present component only in the axial direction, $J = (0,0,J_z)$ and $A = (0,0,A_z)$. As a consequence, the magnetic field strength H and the flux density B have the $x-y$ components, $H = (H_x, H_y, 0)$, $H = (B_x, B_y, 0)$ [9]. These assumptions lead to some simplifications: 3D phenomena as end-effects (i.e., end-windings and magnet overhang) or rotor skewing effect are not considered. In radial-flux machines, this is a common accepted simplification, as presented in literature [17], [18], [19].

In an electrical machine, the variation of electromagnetic field creates electromagnetic forces. These electromagnetic forces act on the stator teeth, excite the structure and cause air-born noise, vibration and harshness (NVH). The radial component of electromagnetic forces is the main contributor to the deflection of the yoke and acoustic noise, whereas the tangential component has a reduced impact, being the main contributor to the production of torque. Most of works from state of the art ignore the tangential component [20], [19], [21], [22]. However, the tangential force has a noticeable contribution to the displacement response and for accurate results, it should be taken into account [23], [24]. The values of electromagnetic forces are derived from the values of magnetic flux densities, obtained by conducting two-dimensional finite element (FE) electromagnetic analysis in Simcenter Motorsolve. For that, the electromagnetic model of the machine under study presented in Fig. 2.9. The magnetic

fields are computed at load conditions, for nominal speed, as a function of rotor position (time component) and air-gap position (space component), resulting in a two-dimensional matrix for each individual analysis. The values of the B fields are determined on an arc of a circle placed in the air-gap at a specific radius r. The value of this radius was chosen closer to the stator teeth, at 0.75 in the air-gap. Moreover, as the obtained values will be transferred to the frequency domain, the values of rotor position step $\delta\theta_{\mathrm{r}}$, expressed in degrees, and the discretisation of the air-gap α must be carefully chosen so that the obtained resolution is reliable. For a given rotor speed n_{r}, the rotor arrives in a specific position position $\theta_{\mathrm{r}}a$ in a time, τ, expressed in seconds:

$$\tau = \frac{\theta_{\mathrm{r}}}{n_{\mathrm{r}}60} \tag{2.15}$$

Besides that, $\delta\theta_{\mathrm{r}}$ is equal to θ_{r} divided with the number of imposed rotor positions. Therefore, the value of $\delta\theta$ must be chosen accordingly with the maximum frequency of interest. A rotor step increment of $\delta\theta_{\mathrm{r}} =$ 3deg and 1800 air-gap points where to compute the B field were selected.

Once the air-gap flux densities expressed in terms of time and space components, $B(\theta_{\mathrm{r}}, \alpha)_{rad,tan}$, the values of air-gap magnetic forces components, radial and tangential, are determined as specified by Maxwell's stress tensor [25]:

$$F_{\mathrm{tan}} = \frac{1}{\mu_0}\int_0^{2\pi} B_{tan}B_{rad}rdl \tag{2.16}$$

$$F_{\mathrm{rad}} = \frac{1}{2\mu_0}\int_0^{2\pi} ({B_{rad}}^2 - B_{tan}^2)rdl \tag{2.17}$$

where μ_0 stands for free space permeability, B_{rad} and B_{tan} represent the radial and tangential components of air-gap flux density and l represents the line in the air-gap where the force is determined. The air-gap force densities as a function of rotor position θ_{r} and air-gap position α obtained for i_{d}= 0A and i_{q}= 50A are displayed in Fig. 2.8 a).

2.5 Structural Domain Analysis

When designing a high-efficient electrical motor, besides the need to fulfill the electromagnetic targets, the system must be also dynamically characterised. This is done by deriving the system transfer function that indicates how the system transmit energy within frequency limits. The dynamic response is specific for a system and it is characterised by a particular geometry, materials and dynamic parameters.

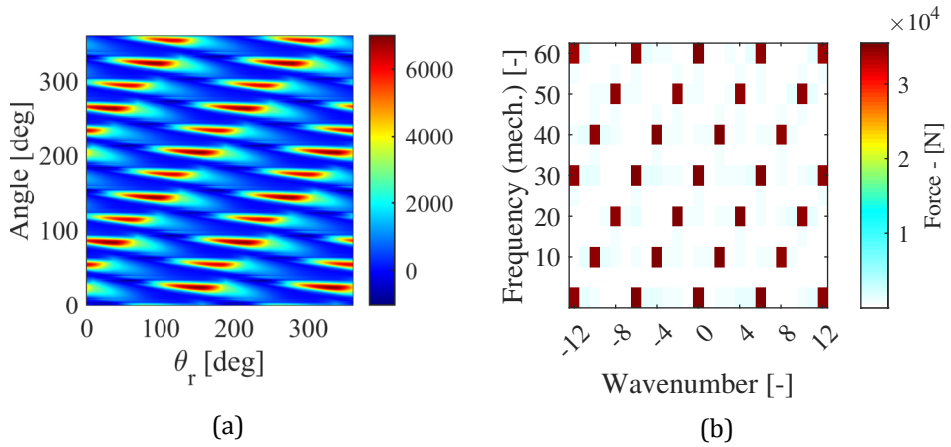

Figure 2.8: Air-gap force densities in time domain (a) and frequency domain (b).

2.5.1 Modal Analysis

The way electrical motor behaves dynamically (e.g., there is an excitation force) is specific to the system's mass, stiffness, damping, geometry, imposed boundary conditions. The dynamic behaviour is characterised by mode shapes. A mode shape is a specific deformation pattern that appears at a particular frequency, referred to in technical literature as natural frequency, resonance frequency or eigen-frequency. It is worth mentioning that a system with n degrees-of-freedom presents n mode shapes [26]. The identification of the structural characteristics (i.e., mode shapes and natural frequencies) is done through a modal analysis technique. Knowing the way the system vibrates help the designer to identify and eliminate the resonances. At resonance, the force frequencies match the structure natural frequencies, amplifying the noises and vibrations. Therefore, this undesirable phenomenon can be avoided by either modifying the stator structure that transmits the energy, and thus modify the stator structure eigen-frequencies so that they don't match the force frequencies, or by directly influencing the vibration source (i.e., the air-gap forces). However, the electrical machine operates at different speed ranges, at variable frequencies. In this case, it is almost impossible to avoid resonances created by the variable frequency forces that act on the stator tooth and excite the structure.

Modal analysis is usually employed to characterise the transfer path. The modal analysis relies on the general motion equation. Considering a system with N degrees-of-freedom, there is a force equilibrium between the inertial, damping, elastic and external forces [19]:

$$[M]\ddot{x}(t) + [B]\dot{x}(t) + [K]x(t) = f(t) \tag{2.18}$$

where $[M]$, $[B]$ and $[K]$ represent the system mass, damping and stiffness matrices of size $N \times N$. With $x(t)$ and $f(t)$ are denoted the displacement and force vectors of size $N \times 1$.

Assuming zero initial displacement and forces and free vibrations conditions, meaning that the damping matrix is a zero matrix and the force vector is null, eq. (2.18) transforms into:

$$[M]\ddot{x}(t) + [K]x(t) = 0 \tag{2.19}$$

2.5.2 Forced response computation

The stator deformation produced by the air-gap forces is the main contributor to the vibration and noise characteristics of PMSMs. Afterwards, this deformation makes the air that encloses the stator to move and generate pressure differences that are perceived as noise by the human ear [27]. In this analysis, it is studied only the interaction between the two domains, electromagnetic and structural, while the impact of the vibrational characteristics on the acoustic domain is not considered here. The couple between electromagnetic and structural domains is considered to be weak, meaning that the electromagnetic forces impact the structural system, but the structural change doesn't affect the electromagnetic characteristics. In this context, a multi-physical workflow of the machine under study is developed in order to allow to compute the vibration response of the system. For this purpose, two FEA models are coupled, a 2D electromagnetic model of the motor and a 3D structural model of the stator core.

In order to study the impact of electromagnetic forces on the stator, the forced response is derived using the vibration synthesis method [28]. The method consists in two parts: the time consuming 2D electromagnetic and 3D structural FE simulations are performed offline, in generic conditions, and the vibration results are obtained online, for operating conditions. For the offline process, the electromagnetic forces are calculated for a set of i_d-i_q currents at different rotor positions and at different locations in the air-gap, obtaining a time and space dependent waveform. Afterwards, the air-gap force, $F_{rad,tan}(t,\alpha)$, expressed as a function of time (t) and air-gap position (α), in both radial and tangential directions, is orthogonal decomposed into $sin - cos$ factors and identified as the superposition of the most important space orders (m, up to the M^{th} spatial component) with the help of Discrete Fourier Transform (DFT):

$$F_{rad,tan}(t,\alpha) = F_{rad,tan[DC]}(t) + \sum_{m}^{M} F_{rad,tan[cos,m]}(t)cos(m\alpha) + \sum_{m}^{M} F_{rad,tan[sin,m]}(t)sin(m\alpha) \tag{2.20}$$

In theory, for accurate results, the number of spatial harmonics, m taken into consideration should be close to M, the total spatial harmonics number. However, the most important contribution to the vibration response is given by the low harmonics and a truncation of the space harmonics can be done for computation simplification. At the same time, M is influenced and limited by the number of nodes on the mesh circumference.

The structural vibration response is numerically obtained offline in Simcenter 3D. A set of unitary force shapes (in both radial and tangential directions), $F_{[I],m}(f)$, with total energy per frequency line equal to 1 N, are applied on the structural 3D model [22]. The total energy of 1 N ultimately allows to have a generalised process and perform scaling in the vibration synthesis procedure. Because dynamic response analysis are performed on a linear structure, modal superposition technique is used to extract the contribution of individual force shape excitation to the forced response. The resulting vibration response for one spatial force excitation shape with unit amplitude, $v_{[I],m}(f)$, can be written as:

$$v_{[I],m}(f) = H(f)F_{[I],m}(f), \tag{2.21}$$

where $H(f)$ represents the system transfer function, usually derived from modal analysis, that characterise the connection between excitation forces and the vibration result.

The online simulations follow the described process: the obtained electromagnetic forces that are extracted from 2D electromagnetic simulations are decomposed, as described in eq. 2.20. Afterwards, the force decomposition factors are used to scale the frequency response obtained for a specific unitary force shape. Ultimately, the final vibration response, $v_{[I]}(f)$, is given by the superposition of all frequency vibration responses $v_{[I],m}(f)$, obtained for each individual unitary force shape (m), scaled with the corresponding sin-cos frequency domain amplitude factors:

$$v(f) = v_{[I],DC}(f)F_{DC}(f) + \sum_{m}^{M}(v_{[I],cos_m}(f)F_{cos,m}(f) + v_{[I],sin_m}(f)F_{sin,m}(f) \tag{2.22}$$

Therefore, the online sequence of the vibration synthesis method

is fast and doesn't require computational effort. The time consuming process is placed in the offline simulation part.

2.5.3 Rotor stress analysis

Predicting the stress and deformation that appear in the motor structure in the early stage design of an electrical machine is a necessary task. The stress appears especially in rotors, due to the inertial loads applied during the rotation and it is amplified at high speed levels. The values of displacement and stress can increase that much that the structure integrity can be periclitated. Therefore, knowing in advance (i.e., early-stage design) if a rotor structure maintains its integrity at high speed saves both time and resources. In the case of PMSM with flux barrier structure, the structural strength assessments must be carefully analysed in order to decide if the iron bridges are wide enough so that the rotor keeps its structural integrity. The rotor saliency is increased by introduction of flux barriers and the electromagnetic torque is improved. The inserted flux barriers limit the d-axis armature reaction flux, while the q-axis flux remains unchanged and can have a positive impact on the harmonic content of the torque [29]. Even if the electromagnetic characteristics are improved, the structural strength of the rotor is diminished by the introduction of air spaces inside the structure. The two targets are conflicting: minimize the iron bridges that connect two flux barriers to improve the electromagnetic characteristics and increase them to keep a high structural strength and maintain rotor integrity especially at high speed (the worst-case condition) [30], [31]. Hence, it is necessary to study the behaviour of rotor designs at maximum machine speed (the worst-case condition) and analyse the may maximum stress points evolve.

2.6 Machine under study

The investigations performed in this study are focused on Interior Permanent Magnet Synchronous Machines (IPMSM). The analysis are conducted on a specific machine, dedicated for automotive applications (i.e., steering applications) that presents a twelve slots, ten poles classical topology. This topology enables to obtain high torque density values, reduced cogging torque given by the number of slot-poles combination and reduced torque ripples. The stator windings are concentrated and connected in a star configuration. The parameters of the machine under study are displayed in Table 2.1. The cross section of the IPMSM under study is identified in Fig. 2.9.

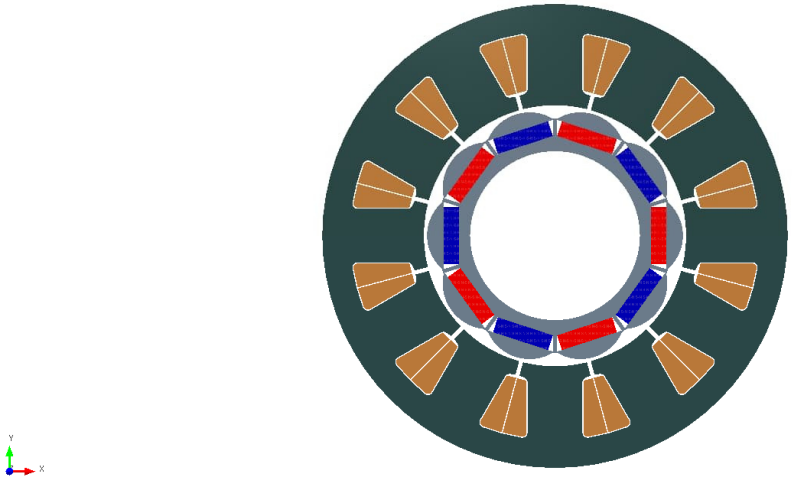

Figure 2.9: Motor cross section.

Table 2.1: Important Parameters of IPMSM.

Parameter	**Value**
Rated Power	800 W
Base Speed	1650 rpm
Maximum Speed	4000 rpm
Rated Current	110 A (rms)
DC Link Voltage	12 V
Minimum Airgap	0.5 mm
Stack Length	58 mm

2.6.1 Electromagnetic parametric model

The electromagnetic model of the machine under study is used to generate data necessary for the multi-physical methods proposed in the next chapters. The electromagnetic model is parameterised, allowing to change the stator geometrical parameters, leaving the rotor geometry fixed. The reason behind this decision is that the stator core is the energy main transmission path and it is the most influenced by the air-gap forces. Hence, the air-gap forces computed in function of stator geometry are among values exported from electromagnetic analysis. Besides that, the electromagnetic torque, back electromagnetic force and motor losses are values of interest. The electromagnetic model presented in Fig. 2.9 is developed in Simcenter Motorsolve, having a 2D discretisation and ignoring 3D effects.

2.6.2 Stator parametric model

In the incipient phase of designing an electrical motor, the engineer has only a few information about the system, and most of it consists in requirements and targets that must be achieved. Among the first information that the designer owns are about the stator core. The stator core is the transmission path for vibrations caused by air-gap forces and has a significant contribution to the total vibro-acoustic characteristics of the machine. Consequently, in the early stage of the design process, the stator core is analysed during structural tests, while the rest of components, such as housing, rotor, winding are left aside.

The stator capability to transmit energy to exterior is defined by the stator structural transfer function, H. In order to characterize the stator, three-dimensional structural analysis are carried out in Simcenter 3D. The numerical analysis is performed on a 3D model of the stator core, build as a virtual replica of the real stator, based on its geometry and material characteristics. Moreover, in order to allow generation of big amount of data, the structural model is fully parameterized, allowing a fast and automatic design change. The parametrisation process for the structural domain follows the same routine as for the electromagnetic domain parametrization [32], keeping the same number of degrees-of-freedom (DOFs) in both cases. This allows to have relevant multi-physic analysis and optimization processes, as both domains are modified similar. The stator geometry parametrisation, together with the corresponding DOFs are presented in Fig. 2.10. Here, the fixed DOFs are stator outer radius, R_a, and stator inner radius, R, whereas the variable DOFs, yoke thickness YT, tooth width TWS, tooth tip angle SOAng, tooth tip height TGD, slot opening SO, are represented with red.

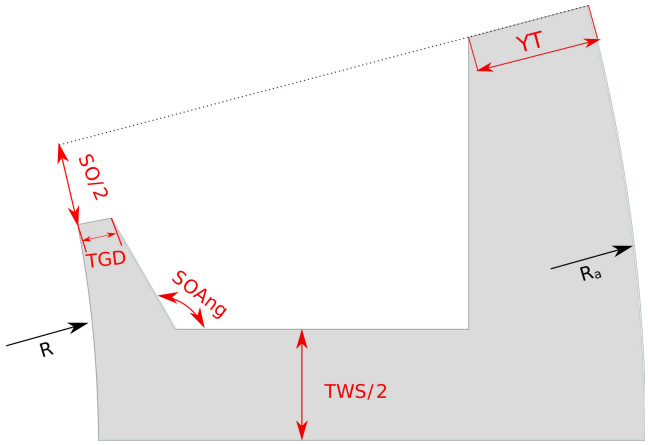

Figure 2.10: The stator parametrization. There are two types of DOFs: fixed – marked with black and variable – DOFs marked with red [33].

Based on the developed parameterised model, thousands of designs created by the combination of different values of geometry parameters can be generated, allowing to generate big data. The variable DOFs are modified within imposed limits in order to generate only feasible designs, with a step that allows to manufacture a generated design. The permitted deviation from the nominal value of each individual geometrical parameter is presented in Table 2.2, where both lower (LB) and upper (UB) boundaries are shown. Besides the stator inner and outer radii, an additional DOF, stator length (L_{stk}), remains unchainged during the analysis. Moreover, for big data generation process, the feasible designs are obtained by filling the input space using sampling techniques. For this study, Latin Hypercube Sampling Technique (LHS) is chosen.

Table 2.2: Stator geometrical parameters and their lower and upper variation boundaries.

Parameter	**LB [%]**	**UB [%]**
JT	-5.56	25
SO	-50	0
SOAng	-2.65	15
TGD	0	100
TWS	-2.94	11.765

The variation of the geometrical parameters have a significant influence on both structural and electromagnetic capabilities of the machine under study. The modification of the yoke thickness results in a change of the structure stiffness that influences the stator vibration re-

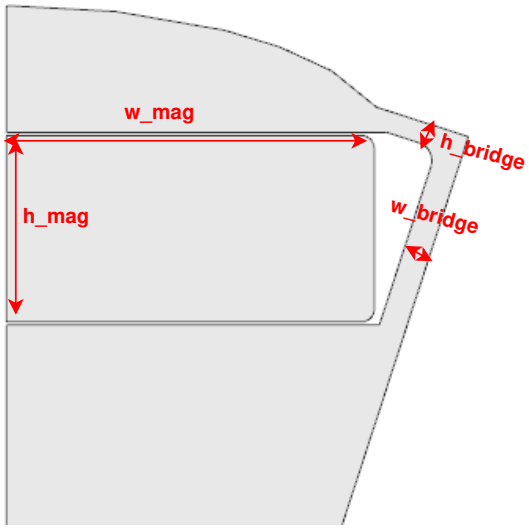

Figure 2.11: Rotor cross-section parameterization. The DOFs marked with red are varied.

sponse. The stator stiffness increases proportionally with the value of yoke size, enlarging the values of natural frequencies. The variation of yoke thickness has a massive impact especially on Mode 0, known as breathing mode. A second parameter that has a consistent influence on the structural characteristics is the tooth width. The tooth width affects the tooth stiffness and can cause local bending modes that generate high displacement amplitude if they are excited by corresponding tangential forces. At the same time, the variations of yoke thickness and tooth width are carefully chosen based on PMSM design rules that helps to avoid machine saturation. As for other design DOFs, such as slot opening, tooth tip height, slot opening angle and tooth tip, their variation interval impacts the electromagnetic values, especially the iron saturation and the flux density harmonic spectrum. It is important to underline that the modification of the flux density harmonics indirectly affects the vibration response.

2.6.3 Rotor parametric model

When designing an electrical motor, the expert must have in mind that the rotor may be subject to high level of stress, depending on the geometry parameters. The stress distribution is assessed at the worst case condition – the maximum rotational speed and has its peaks in the iron bridges. For the stress analysis, only the rotor core, together with the magnets, are modeled, leaving the other components (e.g., housing, stator, winding) aside. Therefore, in order to analyse this problem, a three-

dimensional rotor FE model is build in Simcenter 3D. Material specifications, geometrical limits and boundary conditions are assigned to the developed 3D FE model. As in the case of stator model, the parametrisation is performed with the degrees-of-freedom imposed in the electromagnetic parametrisation process. The parametrisation of the rotor cross section can be identified in Fig. 2.11, where w_{mag} represents the magnet width, h_{mag} is the magnet height, w_{bridge} stands for the rotor iron bridge width, and h_{bridge} is the rotor iron bridge height. Once the parameterised model is created, the process of generating high amount of feasible designs to obtain big data for surrogate model development can be started. The span interval of the described design parameters, w_{mag}, h_{mag}, w_{bridge}, h_{bridge} is chosen in order to generate feasible designs. The fixed DOFs are the stack length (L_{stk}), the rotor inner and outer radii. The design of experiments is conducted using Latin Hypercube Sampling Technique (LHS). The variation interval of the rotor parameters, defined by lower (LB) and upper (UB) variation limits, is identified in Table 2.3.

The variable DOFs are chosen based on their impact on the structural stress characteristics. The bridge width and height are the main contributor to the rotor stress distribution. A thinner bridge translates into increased stress levels.

Table 2.3: Rotor geometry parameters and their lower and upper variation limits.

Parameter	**LB [%]**	**UB [%]**
w_{mag}	-75	12.5
h_{mag}	-66	0
w_{bridge}	-86	66
h_{bridge}	-5	8

3. Electromagnetic Modeling of Electrical Machines

The most common way, used both in industry and academia, to characterize, predict and design an electrical motor is simulation based on Finite Element Analysis. This method reaches high accuracy, allowing for high-fidelity models, but they need long time for developing and computing phases. At the same time, the FE models are not suitable for real-time applications, where the running time is crucial, or for introduction in optimization loops used in the design process, as the computational cost increases dramatically for high numbers of analyzed designs. This means that less designs can be evaluated in a given time, while potential designs with better behaviours are left aside [34]. Therefore, high fidelity motor models able to perform dynamically must be developed. Reduced order models (ROMs) allow to include the data necessary to recreate the behaviour of physical system at a high precision, while the running time is negligible. Typically, the ROMs of electrical machines are developed on generic voltage equations, where the data is obtained from electromagnetic simulations and included in the dyamic environment using multi-dimensional lookup tables (LUTs).

The general voltage equation that is the base for the electromagnetic model of an electrical machine can expressed in different forms. In function of the variable used as state space, the models can be either current or flux-linkage state variable models [35]. The electromagnetic model derives and predicts the winding currents and the electromagnetic torque for different values of winding voltage.

For such models, the accuracy is highly dependent on the data accumulated into LUTs. Moreover, they present operational limits given by the current conditions imposed to extract the data. The dynamic simulations must be kept inside this limits so that the errors caused by LUTs extrapolations, that are not negligible especially due to the highly non-linear behaviour of electrical machines, to be avoided. Therefore, the data computational and extraction time is increased if the motor current is chosen to be several times bigger than the nominal one in order to bring the motor in the non-linear zone and eliminate the extrapolation errors.

Artificial Inteligence (AI) and Machine Learning Methods enters the picture here by proposing a new solution for the classical LUTs based reduced electromagnetic models. The relationships between currents – fluxes and currents – electromagnetic torque can be modeled with the help of machine learning algorithms, resulting in a high-fidelity model with instant run time. This method is suitable for real-time applications

or for optimization process due to its diminished run time that allows to evaluate thousands of design with a reduced computational cost [36].

In the first part of this chapter, two quadrature (dq) based electromagnetic reduced models are described. The two current state variable models use inductances and fluxes extracted from electromagnetic simulations to replicate the behaviour of the real machine. The two classical models are compared from the point of view of their accuracy and computational effort. For the second model, two methods used to perform tables inversions are presented and the errors are identified. Based on the results, the most accurate inversion method is selected. The last part of this chapter is dedicated to developing of reduced order models for electromagnetic targets based on artificial neural networks (ANNs). Moreover, data dimensionality reduction methods are employed in order to diminished the time dedicated for data computation and model training. The efficiency of such a method is evaluated by comparing the prediction accuracy and evaluation costs with the FEA approach. In the end, the feasibility of presented solution is proven by comparing the simulation dynamic results with the experimental ones.

3.1 Inductance-based PMSM model

3.1.1 Machine equations

In order to build the electromagnetic model of the PMSM under study, some common related to the power supply assumptions are made. The supply system used to feed the PMSM is assumed to be three-phased and perfectly balanced. For the star winding connection, the PMSM under study can be mathematical expressed, in dq rotor reference frame, by the voltage equations:

$$\begin{aligned} v_{\mathrm{d}} &= R_{\mathrm{s}} i_{\mathrm{d}} + L_{\mathrm{d}} \frac{di_d}{\mathrm{d}t} + L_{\mathrm{dq}} \frac{di_q}{\mathrm{d}t} - \omega_r L_q i_{\mathrm{q}} \\ v_{\mathrm{q}} &= R_{\mathrm{s}} i_{\mathrm{q}} + L_{\mathrm{q}} \frac{di_q}{\mathrm{d}t} + L_{\mathrm{qd}} \frac{di_d}{\mathrm{d}t} + \omega_r L_d i_{\mathrm{d}} + \psi_{\mathrm{md}} \omega_r \end{aligned} \tag{3.1}$$

where v_{d} and v_{q} the are the windings voltages, i_{d} and i_{q} represent the armature currents, L_{d} and L_{q} are the d- and q-axis inductances, L_{dq} and L_{qd} are the mutual d- and q- axes inductances, ω_r is the angular speed and ψ_{md} is the flux exhibited by the PMs.

Usually, the motor models designed for HiL integration don't include the motor parameters dependence on the rotor position, but for the applications where the motor works in a wide speed-torque broad, high-fidelity models, that provides results similar to FEM ones, are developed. These models take into account, besides the variation of the parameters

in function of armature currents, the parameters variation in function of rotor position, which means that the voltage equation can be expressed in matrix form as in (3.3), after taking into account the term expressed in (3.2).

$$\frac{dL_{\mathrm{x}}(i_{\mathrm{d}}, i_{\mathrm{q}}, \theta_{\mathrm{r}})}{d\theta_{\mathrm{r}}} \neq 0 \tag{3.2}$$

with

$$\begin{bmatrix} v_{\mathrm{d}} \\ v_{\mathrm{q}} \end{bmatrix} = \begin{bmatrix} R_{\mathrm{s}} & 0 \\ 0 & R_{\mathrm{s}} \end{bmatrix} \begin{bmatrix} i_{\mathrm{a}} \\ i_{\mathrm{b}} \end{bmatrix} + \begin{bmatrix} L_{\mathrm{d}} & L_{\mathrm{dq}} \\ L_{\mathrm{qd}} & L_{\mathrm{q}} \end{bmatrix} \frac{\mathrm{d}}{\mathrm{d}t} \begin{bmatrix} i_{\mathrm{d}} \\ i_{\mathrm{q}} \end{bmatrix}$$
$$+ \frac{\mathrm{d}}{\mathrm{d}\theta_{\mathrm{r}}} \begin{bmatrix} L_{\mathrm{d}} & L_{\mathrm{dq}} \\ L_{\mathrm{qd}} & L_{\mathrm{q}} \end{bmatrix} \begin{bmatrix} i_{\mathrm{d}} \\ i_{\mathrm{q}} \end{bmatrix} \omega_{\mathrm{r}} + \begin{bmatrix} -\omega_r L_q i_{\mathrm{q}} \\ \omega_r L_d i_{\mathrm{d}} + \psi_{\mathrm{md}} \omega_r \end{bmatrix} \tag{3.3}$$

In this context, the implementation of the electromagnetic model, based on the dq-frame, starts from a series of electromagnetic simulations performed on the machine under study at different rotor positions and armature currents. The winding inductances expressed in dq reference frame and electromagnetic torque values obtained during the FE simulations are stored in 3D lookup tables (LUTs), and then included in the dynamical model. The derivatives of the motor inductances are computed during a post-processing step and then included in LUTs in the dynamical model.

3.1.2 Frozen Permeability Method

A widely used method for inductance and PM-flux calculation, as well as to divide the machine flux linkage and torque into their components (produced by the PMs or by the stator currents), is the Frozen Permeability Method (FPM). The motor inductances, dependent on the d-, q-currents, were computed using the FPM, by performing a series of steps:

1. An initial non-linear analysis is performed to obtain obtain and store the permeabilities of the motor finite elements that will be later used in a linear analysis.
2. Afterwards, a linear computation is performed by taken into account only the contribution of the PMs, while the stator currents values are imposed to be null. This analysis uses the stored finite element permeabilities to extract the flux generated by the PMs.
3. Finally, the d- and q- fluxes (produced by the armature currents) are extracted by conducting two calculations, by successive setting one of the d- and q- current to non-zero, while the other one to zero. Simultaneously, the permanent magnets are demagnetised by fixing

the remanent flux density to zero. Once the direct and quadrature fluxes are known, the inductances can be derived as follows:

$$L_{\mathrm{x}} = \frac{\Psi_x}{i_x} \quad L_{\mathrm{xy}} = \frac{\Psi_x}{i_y} \tag{3.4}$$

where x,y $\in \{d, q\}$.

3.2 Flux-linkage-based PMSM model

3.2.1 Machine equations

The PMSM under study can be dynamically represented at system level by using a rotor related quadrature axis system of equations. The electromagnetic model uses the dq0 reference frame in order to model as accurate as possible machines with windings connected in delta or star configuration [37]. Based on the precomputed FE results and the variables used as states variables, we can distinguish PMSM electromagnetic dynamic models with either flux linkage or current states variables [38]. The current based state space model with its corresponding equations is identified in eq. (3.5):

$$\begin{aligned} v_{\mathrm{d}} &= R_{\mathrm{s}} i_{\mathrm{d}} + \frac{\mathrm{d}\Psi_{\mathrm{d}}}{\mathrm{dt}} - \omega_r \Psi_{\mathrm{q}} \\ v_{\mathrm{q}} &= R_{\mathrm{s}} i_{\mathrm{q}} + \frac{\mathrm{d}\Psi_{\mathrm{q}}}{\mathrm{dt}} + \omega_r \Psi_{\mathrm{d}} \\ v_0 &= R_{\mathrm{s}} i_0 + \frac{\mathrm{d}\Psi_0}{\mathrm{dt}} \end{aligned} \tag{3.5}$$

where v_{d}, v_{q} and v_0 are the quadrature voltages, i_{d}, i_{q} and i_0 are the machine armature currents expressed in dq0 reference, R_{s} represents the stator phase resistance, ω_r represents the angular speed and ψ_{d}, ψ_{q} and ψ_0 are the flux-linkage.

A common simplification when modeling an electrical motor is to consider that the supply system is perfectly balanced. Moreover, as the machine under study has star connected windings, the 0 components is neglected from the dq0 equation presented in (3.5). Besides that, as it can be observed, the equation system described in (3.5) has as states variables the fluxes on d- and q- axis. The voltage equation is expressed in differential form, where a derivative of flux linkage is introduced. Hence, for the motor dynamic modelling process, a derivative block is introduced in the dynamic model, or the derivative of the flux linkage is performed in a post-processing step and the resulting values are included through LUTs. However, the derivation process introduces undesirable numerical

errors that are not negligible. To avoid them, a change of state variables, from $\psi_{\mathrm{d}}(i_{\mathrm{d}}, i_{\mathrm{q}}, \theta_{\mathrm{r}})$ and $\psi_{\mathrm{q}}(i_{\mathrm{d}}, i_{\mathrm{q}}, \theta_{\mathrm{r}})$, to $i_{\mathrm{d}}(\psi_{\mathrm{d}}, \psi_{\mathrm{q}}, \theta_{\mathrm{r}})$ and $i_{\mathrm{q}}(\psi_{\mathrm{d}}, \psi_{\mathrm{q}}, \theta_{\mathrm{r}})$ can be performed. The changing of the state variable relies on the bijective relationship between the flux linkage and the current $\psi = f_i(i_{\mathrm{d}}, i_{\mathrm{q}}, \theta_{\mathrm{r}}) \longleftrightarrow i = f_{\psi}(\psi_{\mathrm{d}}, \psi_{\mathrm{q}}, \theta_{\mathrm{r}})$. The bijective relationship states that each value from one set is paired to a single value of the other set, and each value of the other set is assigned to exactly one value of the first set, meaning that for every rotor position, for a given d- and q- current combination, a single flux value can be found, and for a combination of ψ_{d} and ψ_{d}, a unique current value is found for every rotor position.

The implication of this is that the d- and q- axis currents can be evaluated at a set of breaking points, that consist of the evenly spaced points between the d- and q-axis fluxes global minimum and maximum. Therefore, by changing the state variable, the voltage equation can be written in its integral form, where θ_{r} stands for rotor position expressed in degrees, as follows:

$$\begin{aligned} \psi_{\mathrm{d}} &= \int (v_{\mathrm{d}} - R_{\mathrm{s}} i_{\mathrm{d}}(\psi_{\mathrm{d}}, \psi_{\mathrm{q}}, \theta_{\mathrm{r}}) + \omega_r \Psi_{\mathrm{q}})\, \mathrm{d}t \\ \psi_{\mathrm{q}} &= \int (v_{\mathrm{q}} - R_{\mathrm{s}} i_{\mathrm{q}}(\psi_{\mathrm{d}}, \psi_{\mathrm{q}}, \theta_{\mathrm{r}}) - \omega_r \Psi_{\mathrm{d}})\, \mathrm{d}t \end{aligned} \tag{3.6}$$

The electromagnetic torque can be also modeled dynamically in a specialised software. For that, the torque is computed as an average value, based on the rates of fluxes and armature currents. This means that the cogging torque or the effect of distortion due to the sinusoidal waveform of the magnetomotive force (MMF) caused by the stator winding distribution are not taken into consideration. The expression of the average value of the electromagnetic torque, where with p it is denoted the number of pole pairs, is:

$$T_{\mathrm{e}m} = \frac{3}{2} p(\psi_{\mathrm{d}} i_{\mathrm{q}} - \psi_{\mathrm{q}} i_{\mathrm{d}}) \tag{3.7}$$

The way the electromagnetic torque is computed as an everage value is a major simplification. Even if for most of the HiL application, the accuracy given by such a model is sufficient, for high-fidelity applications, a dynamic machine model, able to exhibit results close to FE analysis is required. For such a model, the torque ripples given by the cogging and distortion effects must be included. Different approaches to accurately model the electromagnetic torque are presented in literature. In [39], the contribution of the cogging torque and non-sinusoidal MMF to the torque waveform is modeled independently as an additional voltage source to the existing dq-model of the PMSM. Another method, presented in [40],

is to determine the torque value as the variation of the magnetic energy with rotor position, but this results in additional computations, increasing both model complexity and computational time. To overcome this, the torque data, that is already available at the end of the FE analysis, is extracted and stored in 3D LUTs as a function of d- and q-axis currents and rotor position, similar as for other motor parameters (e.g., inductances or fluxes). The procedure is presented in [41], where the torque values are exported as 3D look-up table (LUT) in function of stator currents and rotor position.

Therefore, the electromagnetic reduced order model (ROM) is obtained by extracting data from electromagnetic analysis and importing it in dynamic environments with the help of multi-dimensional LUTs, that can be seen as black boxes, where the output is determined by the input value. Moreover, the accuracy of such models is dependent on the amount of the stored data and on the current span interval imposed for electromagnetic simulations. To avoid the errors introduced during the extrapolation process, when machine is working under overload conditions, the current range used to generate data must be considerably greater than the rated value. On top of that, the model accuracy is directly proportional with the current range decimation: the greater the number of current steps the greater the accuracy. These discussed issues lead to additional computations and increased time to extract data.

3.2.2 Flux-linkage tables inversion based on the non-linear equations

The first method used for flux linkage table inversion consists in solving a non-liniar system defined by two equations (3.8), where having the values of the flux linkages expressed as a function of d- and q-axis currents and rotor position, $\psi_{\mathrm{d}}(i_{\mathrm{d}}, i_{\mathrm{q}}, \theta)$ and $\psi_{\mathrm{q}}(i_{\mathrm{d}}, i_{\mathrm{q}}, \theta_{\mathrm{r}})$, the corresponding currents, $i_{\mathrm{d}}(\psi_{\mathrm{d}}, \psi_{\mathrm{q}}, \theta_{\mathrm{r}})$ and $i_{\mathrm{q}}(\psi_{\mathrm{d}}, \psi_{\mathrm{q}}, \theta_{\mathrm{r}})$ are computed at a series of points that will became the inverted LUTs braking points, $\psi_{\mathrm{d}}^{bp}(i_{\mathrm{d}}, i_{\mathrm{q}}, \theta_{\mathrm{r}})$ and $\psi_{\mathrm{q}}^{bp}(i_{\mathrm{d}}, i_{\mathrm{q}}, \theta_{\mathrm{r}})$.

$$\begin{aligned} \psi_{\mathrm{d}}(i_{\mathrm{d}}, i_{\mathrm{q}}, \theta) - \psi_{\mathrm{d}}^{bp}(i_{\mathrm{d}}, i_{\mathrm{q}}, \theta) = 0 \\ \psi_{\mathrm{q}}(i_{\mathrm{d}}, i_{\mathrm{q}}, \theta) - \psi_{\mathrm{q}}^{bp}(i_{\mathrm{d}}, i_{\mathrm{q}}, \theta) = 0 \end{aligned} \tag{3.8}$$

Since we are talking about non-liniar equations, in order to solve (3.8) and determine the current values, a non liniar solver must be used. At the same time, the solution depends on the initial condition, meaning that if the initial solution is arbitrary chosen, the solution may be different from the right one. A key to this issue is to use, as initial condition, the

already generated FEA data.

Despite its accuracy, the method have a main drawback: the computational time for one table inversion at a specific rotor position is not insignificant, meaning that taking in consideration the third dimension of the LUTs (i.e. rotor position), the time dedicated to table inversion is significantly high (couple of hours).

3.2.3 Flux-linkage tables inversion based on the bijective property between the flux-linkage and current

An equivalent method to inverse the flux tables and obtain the current tables in function of the quadrature currents and rotor position is inversion based on the property of bijection between the flux linkage and the current $\psi = f_i(i_\mathrm{d}, i_\mathrm{q}, \theta_\mathrm{r}) \longleftrightarrow i = f_\psi(\psi_\mathrm{d}, \psi_\mathrm{q}, \theta_\mathrm{r})$. The bijective relationship states that each value from one set is paired to a single value of the other set, and each value of the other set is assigned to exactly one value of the first set, meaning that for every rotor position, for a given d- and q-current combination, a single flux value can be found, and for a combination of ψ_d and ψ_d, a unique current value is found for every rotor position.

The implication of this is that the d- and q- axis currents can be evaluated at a set of breaking points, that consist of the evenly spaced points between the d- and q-axis fluxes global minimum and maximum. As a result, since each combination of $(\psi_\mathrm{d}, \psi_\mathrm{q}, \theta_\mathrm{r})$, resulted from the FEM, is paired to a combination of $(i_\mathrm{d}, i_\mathrm{q})$, the current values $(i_\mathrm{d}^x, i_\mathrm{q}^x)$ linked to the imposed flux breaking points vector $(\psi_\mathrm{d}^x, \psi_\mathrm{q}^x, \theta_\mathrm{r})$, can be obtained using a biharmonic spline interpolation.

The advantage of this method is that it offers accurate results in a very short amount of time, including the case where the third dimension (rotor position) is taken into account.

3.2.4 Flux-linkage inversion methods comparison

The accuracy of the inversion methods are tested by setting a series of d- and q- current values as input at the d and q flux linkage LUTs, while the results are feeding the currents LUTs (obtained from inversion). Afterwards, the imposed current, i_x^*, is compared with the resulting current $\tilde{i}_\mathrm{x}$, for both d- and q- components, obtaining the current absolute error(3.9), whose values, in function of d- and q-axis current and rotor position, in the the following pictures.

$$err_{\mathrm{i_x}} = |i_\mathrm{x}^* - \tilde{i}_\mathrm{x}| \tag{3.9}$$

with x $\in \{d, q\}$.

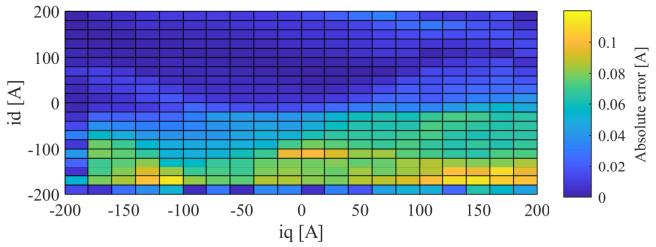

(a)

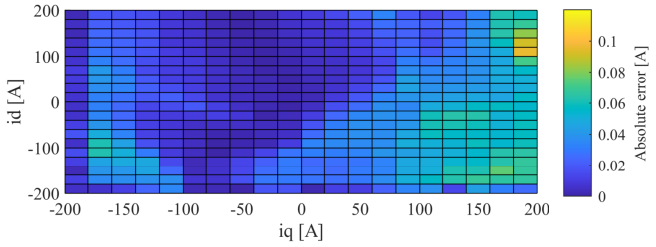

(b)

Figure 3.1: (a) i_{d} and (b) i_{q} absolute current error (expressed in [A]) for the nonlinear equations LUTs inversion method at $\theta_{\mathrm{r}} = 0$ for all current combinations.

The absolute current error obtained for the first flux-linkage LUTs inversion method is presented in Fig. 3.1 for the initial rotor position. Because the flux-linkages were extracted as a function of various armature currents and rotor position, different errors are obtained for various instances. One can see that the maximum error can be found at the extreme values of d- and q-axis currents. At the same time, the maximum absolute error obtained for the d-axis is 0.128 [A] and 0.101 [A] for the q-axis, while the mean absolute current error is 0.017 [A] for the d-axis and 0.014 [A] for the q-axis.

The accuracy of the second presented method dedicated to LUTs flux-linkage inversion can be identified in Fig. 3.2 a) and b) for the d-axis and q-axis currents errors, respectively. It is worth to notice that the errors are decreased significantly, with one order of magnitude in both d- and q- axis, compared with the previously described method, while the error distribution tends to remain the same, the highest errors being situated at the extreme values. However, the outlined errors distribution does not influence the quality of the results because the data used for LUTs was obtained for a current range selected as seven times the rated current in order to avoid the extrapolation of data if the motor is over-

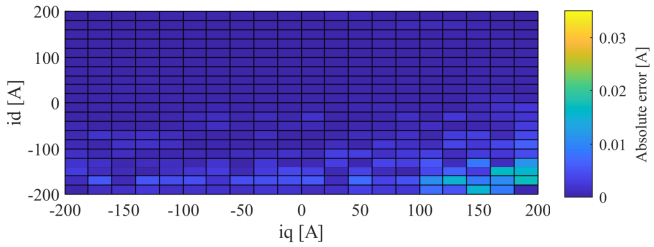

(a)

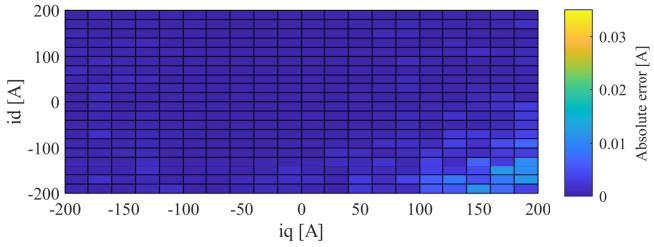

(b)

Figure 3.2: (a) i_{d} and (b) i_{q} absolute current error (expressed in [A]) for the bijective relationship LUTs inversion method at $\theta_{\mathrm{r}} = 0$ for all current combinations.

loaded and create a robust model, but for normal operating conditions, the machine is not exceeding its rated current and the maximum errors will not be reached. Focusing on the error values, one can observe that the maximum absolute error obtained for the d-axis is 0.038 [A] and 0.026 [A] for the q-axis, while the mean absolute current error is 0.0017 [A] for the d-axis and 0.0012 [A] for the q-axis.

3.3 Machine Learning based Electromagnetic Model

An alternative to the classical LUTs based ROM is to make use of the machine learning methods. An artificial neural network (ANN) can be trained to fit the relationships between current – flux and current – electromagnetic torque. It is already known that ANN has an increased capability to find patterns in data and fit non-linear functions, providing a fast characterization of the system [42].

A surrogate model of the PMSM under study can be obtained without using the classical LUT approach using artificial neural networks. This way, the development time is reduced, while, accuracy is still maintained closed to the FEA level and the torque ripple prediction is assured with-

out additional computations. The process of building the surrogate model requires to generate the necessary data from a series of electromagnetic FE analysis, post-process the obtained data and harness it, and ends with the training and validation phases. The proposed surrogate model is obtained using two multi-layer artificial neural network models (i.e., one for fluxes and another one for electromagnetic torque). Data dimensionality reduction methods are applied on the developed models in order to reduce the development time.

3.3.1 Data Generation

Electromagnetic FE analysis are performed on the PMSM under study with the purpose of obtaining the electromagnetic quantities (i.e., dq values of fluxes and electromagnetic torque). The geometrical parameters of both rotor and stator are kept constant, while the d- and q- axis currents are varied from -200 A to 200 A with a step of 20 A step. The rotor position is swept from 0 to 36 mechanical degrees. Therefore, the electromagnetic values are exported as functions dependent on rotor position and saturation effects (i.e., given by the current). All the analysis are conducted for the nominal speed value. The mesh size is chosen so that a high accuracy solution is obtained in a reasonable amount of time. Therefore, the 2D analysis is performed at speed–accuracy ratio of 3, where the maximum is 10, corresponding to the most accurate results, and the minimum is 1, corresponding to the fastest solution. For this speed – accuracy trade-off, one electromagnetic analysis lasts around 3.5 min.

3.3.2 Electromagnetic Surrogate Model

The implementation of the electromagnetic surrogate model starts with data generation. Afterwards, the data is harnessed with the help of machine learning algorithms chosen to fit time-varying values. In this case, an artificial neural network algorithm was chosen to fit the fluxes and electromagnetic torque values. ANNs are often used in the field of electrical machines for machine control, anomaly detection, fault diagnosis, magnetic field approximation [43]- [47]. When building the surrogate model, the ANN model inputs and outputs, together with the model's architecture, must be specified.

Furthermore, the computational cost of building a surrogate model can be drastically reduced when data dimensionality reduction techniques from the field of machine learning are employed. By employing data dimensionality reduction, the learning process stops when a desired accuracy level is reached, resulting in fast and high-accuracy models. An example is discussed in [46], where various input data samples are compared

and their impact on the accuracy of an ANN model for torque estimation is discussed.

3.3.2.1 Artificial Neural Network Description

The capabilities of the artificial neural network to fit non-linear functions, together with its ability to perform extrapolation, make this machine learning algorithm a proper method for surrogate models of electrical machines [43]. A typical ANN model presents one of the following two architectures: a single-layer configuration where the neurons from the first layer are directly connected to the output layer, and the multi-layers configuration, where additional hidden neuronal layers are interleaved between the input and output neurons [42]. Usually, due to architecture complexity and training time reasons, no more than three hidden layers are used [48].

For the problem described in this chapter, an ANN architecture with a multi-layer configuration is employed. The chosen ANN is a feed-forward model, where the data flows in an unique direction, from the input layer to the output one, without any feed-back information. The first layer (i.e., input layer) receives the information and then transmits and distributes it to the neurons belonging to the intermediate layer. Next, in the intermediate layer, the data is processed and the result is passed to the output layer.

The basic architecture of a multi-layer ANN is presented in Fig. 3.3. Here, the connection between different layers can be observed. It is worth mentioning that the nodes belonging to the same layer are not interconnected. The hidden layers fit the data by modifying some constants called weights and biases. The information x_i arrives in the input layer, it is distributed to the hidden layers where it is augmented with weights values and then added over bias constants. The result of this process, z, is mathematically expressed as a function of weights w_{ij} and biases b_{ij} between the i^{th} input neuron and the j^{th} hidden neuron, where with n it is denoted the number of inputs:

$$z_j = \sum_{j}^{n} \sum_{i}^{n} w_{ij} x_i + b_{ij} \tag{3.10}$$

The resulting value, z, is introduced in the expression of a transfer function, called activation function, to obtain the neural network's output. For this particular electromagnetic problem, the output layer uses the non-linear activation function – the sigmoid function:

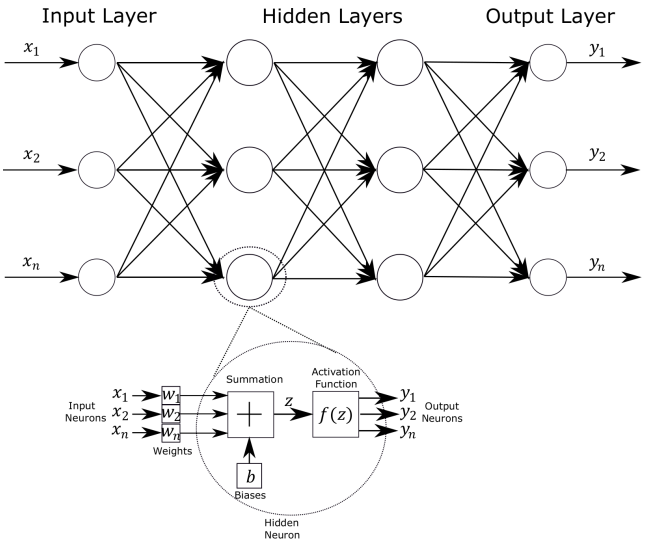

Figure 3.3: Neural network structure [49].

$$f(z) = \frac{1}{1+e^{-z}} \tag{3.11}$$

3.3.2.2 Model implementation

Two individual surrogate models are developed, one for electromagnetic torque estimation and one for d- and q- axies flux-linkage values. The first ANN model estimates the current from flux-linkage values and rotor position, while the other one predicts the electromagnetic torque from d- and q-axis currents and rotor position. A visual description of the process in dq reference frame is presented in Fig. 3.4. The first ANN based surrogate model for current prediction presents a structure characterised by four layers. The first layer has 3 input neurons, 60 neurons are imposed in the first hidden layer, while the second hidden layer is made of 20 neurons. Additionally, 2 neurons are defining the output layer. The input values are the dq flux-linkages and the rotor position exported from the 2D FE electromagnetic analysis, while the output are the dq currents. The advantage of the ANN-based surrogate model over the LUTs-based model is that the data doesn't require time consuming post processing procedures. In the case of (LUTs)-based model, the data needs to be post-process by applying tables inversion, that is time consuming and can reach, for the described data-set from one to two hours. On the other hand, if the network is properly learned, it gives accurate outputs and the process of flux-linkage tables inversion is avoided, saving time.

The second ANN based surrogate model network is trained to esti-

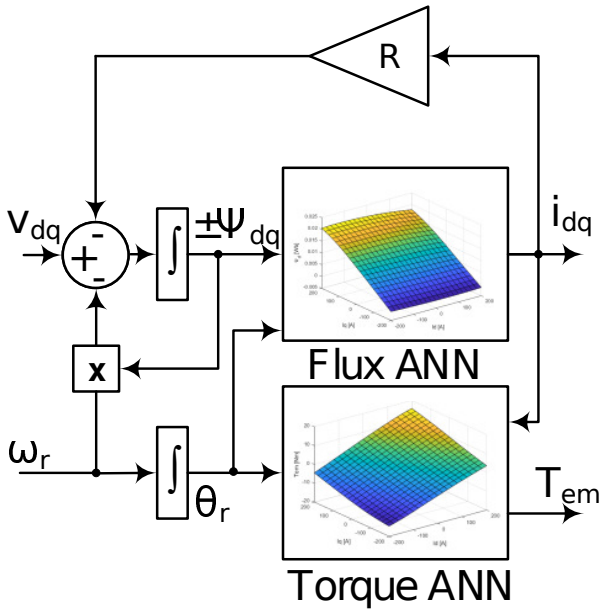

Figure 3.4: Graphical representation of the proposed surrogate model.

mate electromagnetic torque. This model has a straightforward topology, defined by three layers. The first layer contains 3 neurons, the middle layer is defined by one hundred neurons and the third layer is formed by one neuron. The input of the torque surrogate model are the d- and q-axis currents, i_{d} and i_{q}, and the rotor position, θ_{r}, while the output is represented by torque values.

3.3.2.3 Levenberg-Marquardt backpropagation algorithm

The most commonly algorithm for biases and weights update in multi-layer feed-forward ANNs is the Levenberg-Marquardt backpropagation algorithm (LMBPA). This algorithm, derived from Newton method to minimise non-linear functions, solves least-squares of nonlinear problems [50]. The function is minimised by updating the weights and the biases based on the function Hessian matrix ($\nabla^2 F$) and function gradient matrix (∇F):

$$w_{k+1} = w_k - (\nabla^2 F)^{-1} \nabla F_k \tag{3.12}$$

By expressing the objective function F as the sum of squared errors, $e_{t,n}^2$ obtained for the training sample t at output n, the Levenberg-Marquardt algorithm is minimising the error function, E regarding a vector (in this study, weight vector) [51]:

$$E(x,w) = \frac{1}{2}\sum_{t=1}^{T}\sum_{n=1}^{N} e_{t,n}^2 \tag{3.13}$$

where x represents the input signal, w is the weight vector, t corresponds to training sample. The difference is given by computing the absolute error, in the training phase, given by the difference between the expected value (output reference) and the resulting value:

$$e_{t,n} = y_{t,n}^* - y_{t,n} \tag{3.14}$$

The function Hessian matrix is given by performing the function's second derivative, and it is used in the objective function minimisation process:

$$H = \begin{bmatrix} \frac{\partial^2 E}{\partial w_1^2} & \cdots & \frac{\partial^2 E}{\partial w_1 w_n} \\ \cdots & \cdots & \cdots \\ \frac{\partial^2 E}{\partial w_n w_1} & \cdots & \frac{\partial^2 E}{\partial w_n^2} \end{bmatrix} \tag{3.15}$$

In the Levenberg-Marquardt algorithm approach, the Hessian matrix is derived from the Jacobian matrix, J, the μ constant and the identity matrix, I, as it is expressed in (3.16). For small values of μ, the Levenberg-Marquardt algorithm transforms into Gauss-Newton algorithm.

$$H = \nabla^2 E = J^T J + \mu I \tag{3.16}$$

where the Jacobian matrix is expressed as:

$$J = \begin{bmatrix} \frac{\partial e_1}{\partial w_1} & \cdots & \frac{\partial e_1}{\partial w_n} \\ \cdots & \cdots & \cdots \\ \frac{\partial e_n}{\partial w_1} & \cdots & \frac{\partial e_n}{\partial w_n} \end{bmatrix} \tag{3.17}$$

The gradient function is computed in a small amount of time by using the function Jacobian:

$$\begin{aligned} g_i = \frac{\partial E}{\partial w_i} &= \frac{\partial(\sum_{t=1}^{T}\sum_{n=1}^{N} e_{t,n}^2)}{\partial w_i} \\ &= \sum_{t=1}^{T}\sum_{n=1}^{N} \frac{\partial e_{t,n}}{\partial w_i} e_{t,n} = Je \end{aligned} \tag{3.18}$$

The Levenberg-Marquardt algorithm method is derived by substituting (3.16) and (3.18) in (3.12) [52]:

$$w_{k+1} = w_k - (J_k^T J_k + \mu I)^{-1} J_k e_k \tag{3.19}$$

3.3.2.4 Neural Network Overfitting

When training a neural network, two situations may appear: underfitting – the network doesn't behave as expected and is not able to characterise the right input – output relationship; and overfitting, the network is trained to obtain perfect results for the training data, learns its particularities and doesn't have the ability to generalize and adapt to unseen data. For the overfitting situation, even if the model will perform with increased accuracy for the training data, it will not be able to behave well when new input data is provided to the model. Therefore, the effort invested when training the neural network must be optimised in order to avoid the two situations. To avoid issues introduced by overfitting, multiple networks can be trained with different values for the weights and biases and data can be divided in different training, validation and test samples ratios. In the end, their generalization capability is tested. A most common approach to avoid overfitting is to use an "early stopping" algorithm. The data is still divided based on its purpose into training, validation and testing sets. The first set, training data, is applied for weights and biases computation. During the training process, the validation and training errors are evaluated and their evolution trend is analysed in order to quantify the generalisation capacity of the network. During the training process, the errors normally decrease. However, if overfitting becomes an issue, the validation error increases. This is the moment when the early stopping algorithm steps in and the learning process finishes [53]. The early stopping algorithm usually intervene after the validation error increased during some successive iteration and stops the algorithm based on the stopping criterion (the number of iterations in which the validation error increased) chosen by the user.

For the developed surrogate models, the data exported from the 2D electromagnetic simulations are split in 70 [%] destined for model learning, 15 [%] for validation and 15 [%] for test phase. During the training phase, an early stopping criterion is used. The learning is stopped if the validation error increased in more than 300 successive iterations. The weights and the biases values are given by the iteration where a minimum validation error appeared. The developed neural networks generalization capability is assessed by imposing aleatory inputs and computing the results error, where the reference ones are the FEA simulations outputs.

3.3.3 Data Dimensionality Reduction

Normally, when generating big data used to build the surrogate models of electrical machines, the data is extracted from electromagnetic 2D simulations with user pre-defined input conditions (i.e., a fixed range

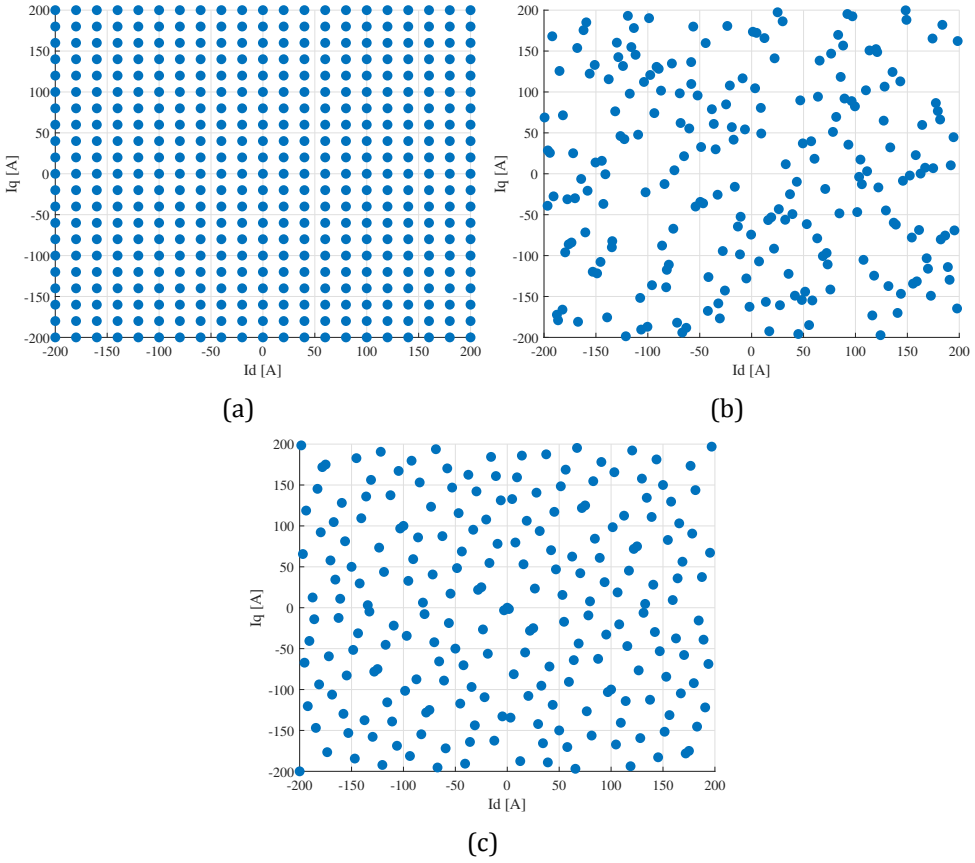

Figure 3.5: Space discretisation methods: (a) EDD with 441 samples, (b) LHS with 220 samples and (c) Sobol sequence with 220 points.

of d- and q-axis currents and rotor positions). This means that the data is generated in a non-adaptive process and the input conditions space is not changed during the data generation process, but it is fixed and defined by equal separation ranges, as it can be seen in Fig. 3.5 a), where a number of 441 i_{d} and i_{q} samples, per one rotor step, are used to generate data needed to train the neural network. In this case, as the data is computed and extracted in only one procedure, the size of data generated can exceed the model needs to obtain accurate results. Therefore, to overcome this problem and reduce the computational time, machine leaning methods, known as adaptive data generation methods, can be implemented.

3.3.3.1 Adaptive Data Generation Process

The dimension of the data generation and the dedicated process time are reduced using an active learning method – the adaptive samples generation. By using this method, the network is trained with data

extracted during multiples steps. In a first step, a small amount of data are extracted from electromagnetic simulations, the surrogate model is trained and the output result error is analysed. Based on the obtained error value, additional data is generated, if the error is bigger than a fixed threshold, or the process is stopped and the surrogate model is considered mature, if the error is small enough. The described process is an iterative one and the data is generated until the model achieves a desired fidelity.

During an adaptive data generation process, a pseudo-random algorithm to generate the input samples is used. This algorithm fills the input space uniformly so that the clusters or big slots between samples are avoided. The most common sampling methods used are Latin Hypercube Sampling (LHS) method, Monte Carlo (MC) algorithm and Sobol sequence [54]. Among the three sampling methods, the Sobol sequence presents the capability to spread the data, even for higher dimensions. Figure 3.5 c) presents the input space sampled using this technique. Compared with the LHS method, presented in Fig. 3.5 b), it can be seen that the input space is filled more uniform. The main advantages of Sobol sequence are: the capacity to fill the space uniformly increases with the number of sample points; a good organization of data in the space for small data sets; the algorithm converges fast.

3.3.3.2 Implementation

An iterative adaptive data generation process with the goal to obtain ANN based surrogate models with relative error under 1 [%] is employed using LHS and Sobol sequence techniques. The initial data set is set to 100 i_d-i_q samples for each rotor step, and the data size is increased until a desired level of accuracy is achieved. The torque and flux errors given by different data sets are depicted in Fig. 3.6 a) for Sobol sequence method and in Fig. 3.6 b) for the LHS method. In both cases it can be observed that the error values reduce as the number of input i_d - i_q increases. Moreover, for Sobol sequence method, the results start to be accurate if the input dimension reaches 200 i_d-i_q combinations. The mean relative error get from the torque model (represented with black) and flux model (depicted with red curve) is small for 200 i_d-i_q training samples. For this input dimension, the Flux ANN model presents a maximum error (marked with green line) of less than 1 [%], but the Torque ANN model presents a relative error that reaches a highest value of 2.84 [%], that exceeds the imposed maximum value. This value drops under 1 [%] when the input dimension is enlarged with 20 points.

Therefore, the dimension of the data used to train the torque and

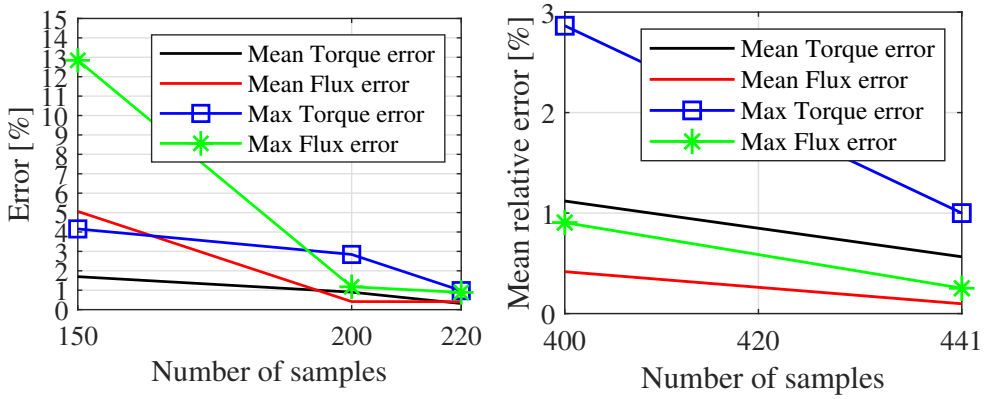

(a) Sobol sequence

(b) LHS

Figure 3.6: Relative errors [%] in function of number of samples.

flux-linkage ANNs was reduced to 200 points, keeping the model accuracy, by generating data flexible using Sobol technique. This means a 50 [%] reduction of the imput space, compared with the conventional way of generating information, Equally Distributed Data (EDD), visible in Fig. 3.5 a), where the input is defined by 441 data points. Therefore, the data dimension and its generation time is significantly reduced. The quantification of the time saving on both data generation through FE analysis and on the training time is presented in Table 3.1. As it can be observed, both time values are reduced with almost 50 [%], compared to the classical case, the non-adaptive one. In addition to that, the correlation between the training time and the size of data samples can be identified in Fig. 3.7. Here, starting from 150 samples per rotor position to 441 samples, the training time increases notably with the increasing of the number of samples. The training time of the Flux ANN model is higher, compared with the Torque ANN model and this is caused by the increased number of layers and neurons. Analysing the problem, it can be seen that the results obtained for the surrogate model that used Sobol sequence method to obtain data is the most accurate, while the computational resources are diminished.

Additionally, if LHS method is employed for data generation, the surrogate models present high fidelity results only for more than 400 training samples. This is easily explained by looking at the data distribution in the input space, where big gaps between points and a lack of points on the upper and lower limits are encountered, as it can be remarked in Fig. 3.5 c). A quantification of the relative errors given by Torque ANN and Flux ANN trained with data obtained by performing LHS can be identified in Fig. 3.6 b). It is visible that the error decreases when the number of input sampling increases, however even for 400 samples, the maximum error is

Table 3.1: Time necessary to build the ANNs.

Data type	Nb. samples	FE Analysis	ANN training	Total time
EDD	441x61	558 [min]	90 [min]	648 [min]
LHS	400x61	506 [min]	70 [min]	576[min]
LHS	441x61	558 [min]	75 [min]	633 [min]
Sobol	150x61	190 [min]	20 [min]	210 [min]
Sobol	200x61	253 [min]	39 [min]	292 [min]
Sobol	220x61	279 [min]	46 [min]	325 [min]

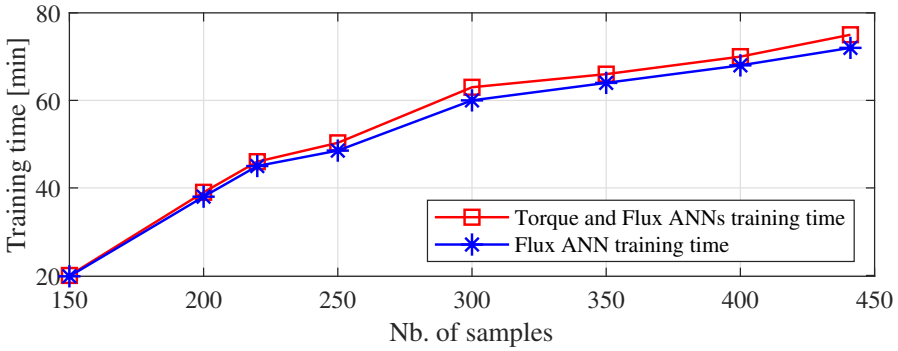

Figure 3.7: The time dedicated to train the ANNs.

above 1 [%] (e.g., Torque ANN relative error present a mean value of 1.1 [%] and a highest value of 2.9 [%]). The errors are decreased under the 1 [%] threshold when the number of samples is increased to 441. Therefore, the adaptive data generation using LHS method doesn't diminish the computational burden needed to generate information and develop the ANN.

A comparison between the FEA results, taken as reference, and the results acquired by running the surrogate models successively developed using EDD data and reduced size data obtained through Sobol sequence (with 220 samples) and LHS (with 441 samples) is presented in Fig. 3.8. Figure 3.8 a) presents the torque values in function of rotor position, in steady state at rated speed, while Fig. 3.8 b) depicts the corresponding instantaneous errors. By analysing the results, it can be observed that the Sobol 220 network performs the best and behaves similar to FEA, while reducing the over-all necessary time with 50 [%].

3.3.4 Sobol 220 network model validation

As it was underlined in the previous section, the Sobol 220 sequence, henceforth referred to as Sobol 220 network model, present the

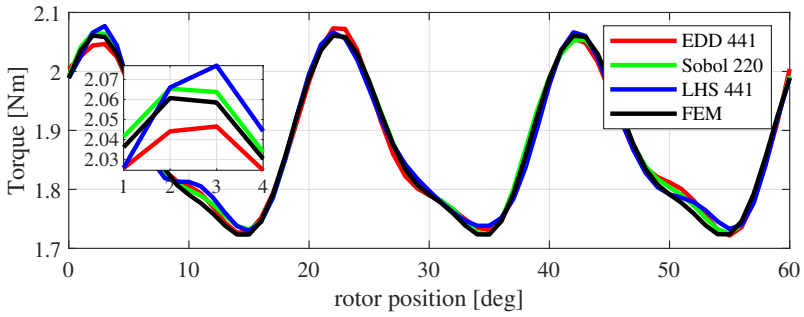

(a)

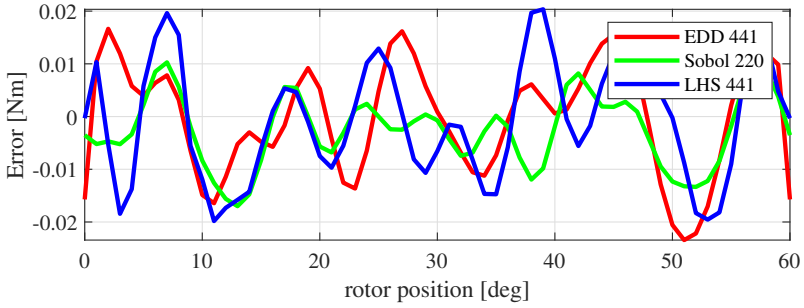

(b)

Figure 3.8: FEA vs surrogate model results: (a) electromagnetic torque and (b) instantaneous error, at steady state conditions.

closest results to FEA and reduces the total time with 50 [%]. In order to validate the network capabilities to exhibit good results under any operation conditions, different validation scenarios are employed. The first validation scenario is at rated conditions (current and speed). The resulting values can be observed in Fig. 3.9 a), where the Sobol 220 network model predicts the torque value, even the torque ripple. For a more in-depth analysis, the harmonic content of the obtained torque is examined in Fig. 3.9 b). By evaluating the harmonic spectrum, it can be noticed that the harmonics amplitudes are insignificantly changed, compared with FEA, for most important orders and new harmonic orders are not introduced.

The next step consist in testing the model capability to fit the results for the high saturation case. For this case, the machine is taken to the nonlinear operating point by multiplying the phase current firstly with a factor equal to five and then with a factor of eight. The latter case is not belonging to the current variation interval used to generate data from FEA. This case is used to demonstrate the generalization capacity of the model under test. The torque values derived by imposing a current amplitude of $5I_{rated}$ are identified in Fig. 3.10 a) and the ones obtained for by imposing a current amplitude of $8I_{rated}$ are shown in Fig. 3.11 a). For both

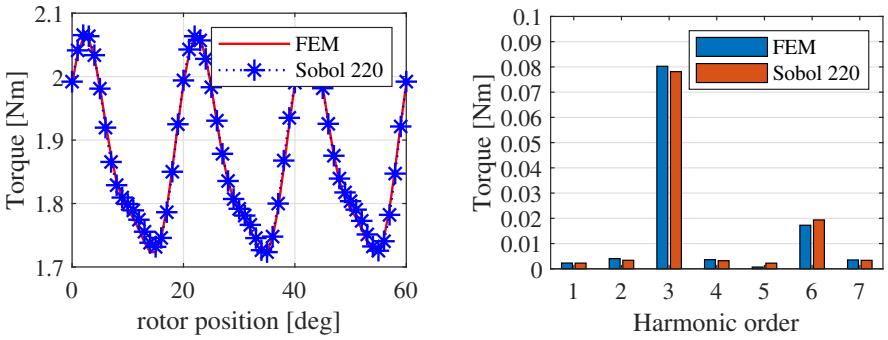

Figure 3.9: FEM vs. ANN Torque results: electromagnetic torque at rated current (a) FEM vs ANN Torque comparison obtained for rated current (a) Waveform and (b) Frequency spectrum.

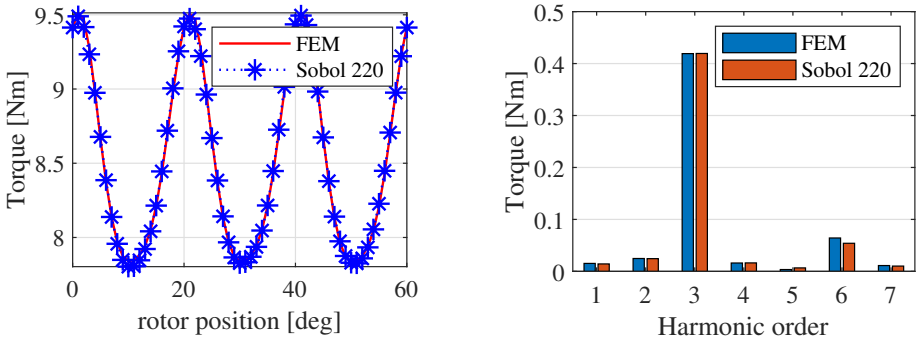

Figure 3.10: FEM vs. ANN Torque results: electromagnetic torque at $5I_{rated}$ (a) FEM vs ANN Torque comparison obtained for rated current (a) Waveform and (b) Frequency spectrum.

presented examples, the surrogate model is able to present close to FEA results, keeping an error under 1 [%]. In addition to that, it is notable that the surrogate model is capable of predicting the torque ripples created by the distorted magnetic field and cogging effect, even when the machine is highly saturated. The harmonic spectrum of the electromagnetic torques obtained through the discussed two methods are presented in Fig. 3.10 b) and Fig. 3.11 b). Compared with the rated current condition, the amplitude of the harmonics is negligibly changed, and no addition of substraction of harmonic orders is encountered. This demonstrates that the Sobol 220 ANN model can accurately predict the electromagnetic torque with high accuracy under normal or high saturation conditions.

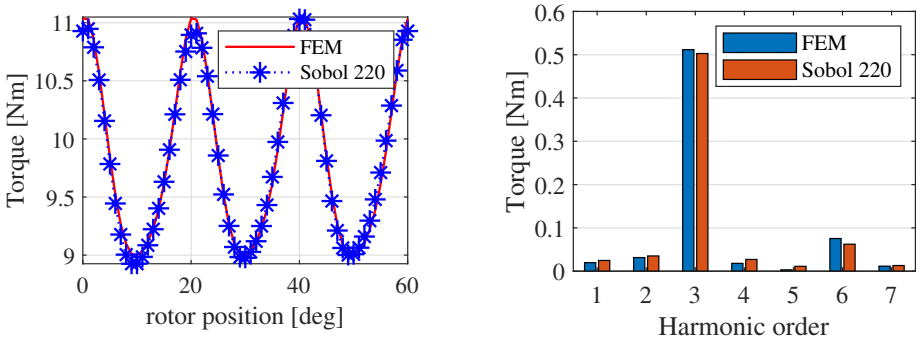

(a) (b)

Figure 3.11: FEM vs. ANN Torque results: electromagnetic torque at $8I_{rated}$ (a) FEM vs ANN Torque comparison obtained for rated current (a) Waveform and (b) Frequency spectrum.

3.4 Linear vs. surrogate electromagnetic model

A comparison between the classical LUTs based electromagnetic model and the surrogate model based on artificial neural network with flux linkage as state variable is performed in order to quantify the improvements given by the latter. The classical LUTs based electromagnetic model used for this comparison is the linear model that uses inductances extracted from FE electromagnetic analysis. Knowing that the motor has a star winding connection and assuming that the three-phase currents system is perfectly balanced, the voltage equations of the linear model can be expressed in dq reference frame, using quadrature currents as state variables as it is expressed in eq. 3.1.

The motor electromagnetic values (i.e., quadrature inductances) are determined from 2D electromagnetic simulations as a function of d- and q-axis currents using frozen permeability method (FPM) [55]- [56]. Afterwards, the obtained inductances are introduced in the dynamic model with the help of 2D LUTs. Additionally, the torque ripple is predicted by including a three dimensional table where the torque exported from FE analysis presents d- and q-axis currents and rotor position dependency.

The accuracy of the flux-linkage model developed is compared with the inductance model, presenting also the FEA results as reference. For a fair comparison, all three models are supplied with a sinusoidal 3-phase voltage system:

$$v_k = v_d \cos(\theta_r + \alpha) - v_q \sin(\theta_r + \alpha) \tag{3.20}$$

where $k \in \{a,b,c\}$ and $\alpha \in \{0, 2\pi/3, -2\pi/3\}$.

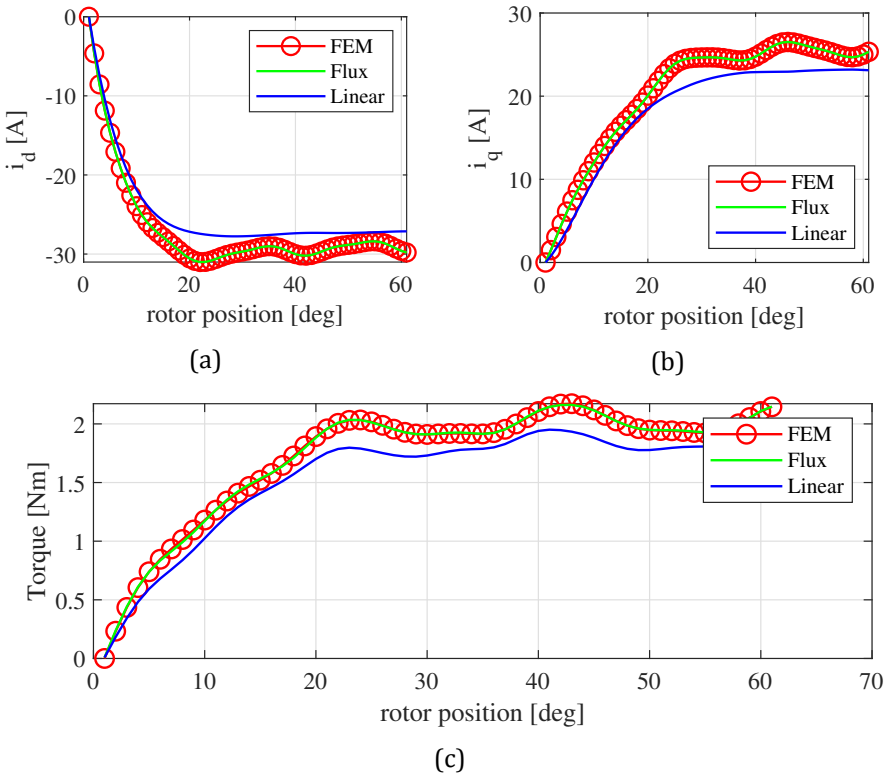

Figure 3.12: Flux-linkage and linear ANN-based models (a) d- axis current (b) q-axis current and (c) electromagnetic torque waveforms.

The obtained d- and q-axis currents and electromagnetic torque resulting by applying a source of voltage defined by $v_{\mathrm{d}} = 0[V]$ and $v_{\mathrm{q}} = 4.4[V]$, with the rotor spinning at a constant speed of 1500 [rpm] can be depicted in Fig. 3.12. As it can be observed in Fig. 3.12 a) and Fig. 3.12 b), the linear model is not capable to accurately compute the armature currents. This is due to the fact that saturation effects and the voltage drop due to motion are not taken into account in the mathematical model. On the contrary, the surrogate model predicts with high precision the armature currents, as it can be observed in the Fig. 3.12 (a) and (b), where the obtained results are matching the FEA ones. Figure 3.12 c) presents the resulting electromagnetic torque and underlines the capacity of the surrogate model to predict the values, taking into account the torque ripples as well. Moreover, the linear model doesn't succeed to perform at the same level. The electromagnetic torque is not predicted well, even if a 3D LUT is used to store the rotor position and armature current dependent torque data. The cause of this situation is the low accuracy of the model to predict the currents, as the model was based on a linear expres-

sion of voltage equations. As the surrogate model behaves the best, the flux-linkage ANN-based model will be further validated by comparing its results with experimentally obtained data.

3.5 Experimental validation

The accuracy and performances of the developed electromagnetic surrogate model is finally tested by comparing the simulation results with the experimental ones. For that, the dynamical surrogate model is developed within Matlab/Simulink software environment. For this study, the surrogate models developed based on Sobol 220 networks is used due to its accuracy, compared to FEA, and reduced computational time, as presented in Section 3.3.3.

The dynamic model that incorporates the surrogate models is build based on the PMSM dynamic model that uses currents as state variables. The PMSM dynamic simulation model developed within Matlab/Simulink is presented in Fig. 3.13. An initial condition is required for the two integrators included in the model. The two initial conditions are the corresponding quadrature values of the permanent magnet flux-linkage. These values are derived from a no-load analysis, for the rotor fixed at initial position. Besides the developed PMSM model, in Matlab/Simulink the motor's electronic control unit is modeled. The electronic control that relies on the Field Oriented Control (FOC) is used to force the machine to follow the imposed reference values [57]. The FOC algorithm [58] determines the voltages needed to be supplied so that the the machine follows the imposed reference speed trajectory independent of the applied load torque. Once both systems are modelled within the dynamic software, on both dynamic model and experimental benchmark, arbitrary speed and load torque variations are applied.

The testing benchmark is identified in Fig. 3.14. The testing facilities include the PMSM under study and its 3-phase inverter, a DC machine used as load machine and connected to a programmable load. Besides that, a series of sensors are connected to the test-bench to perform the measurements and a NI RSeries FPGA is used as a general controller.

Figure 3.15 presents the speed and torque variations obtained by performing virtually measurements on the dynamic model and real measurements on the test-bench. The measured values are compared with the reference ones. As it can be observed, the values obtained for the velocity are overlapping. For the electromagnetic torque, a very good agreement between the results can be distinguished. It has to be underlined that no filtering procedure was applied on the measured values in order to have a fair comparison between the measured and simulated data. It

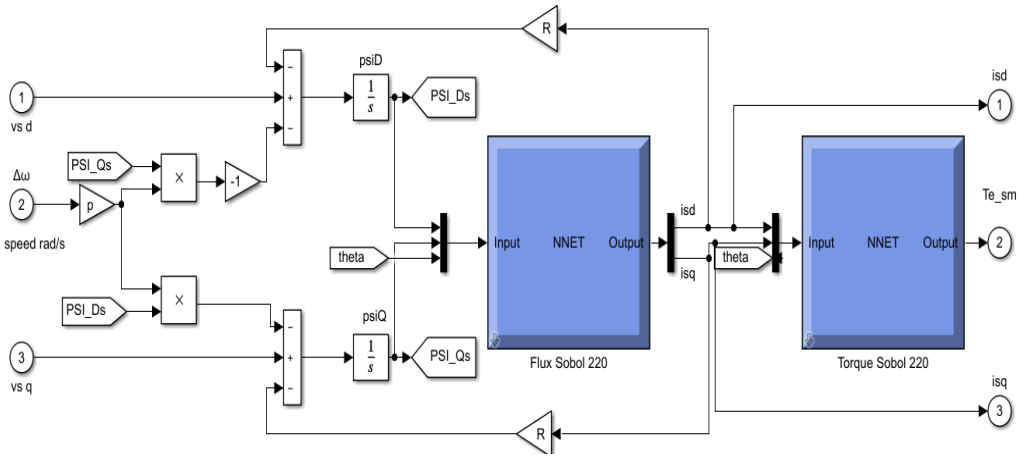

Figure 3.13: The Matlab Simulink PMSM model.

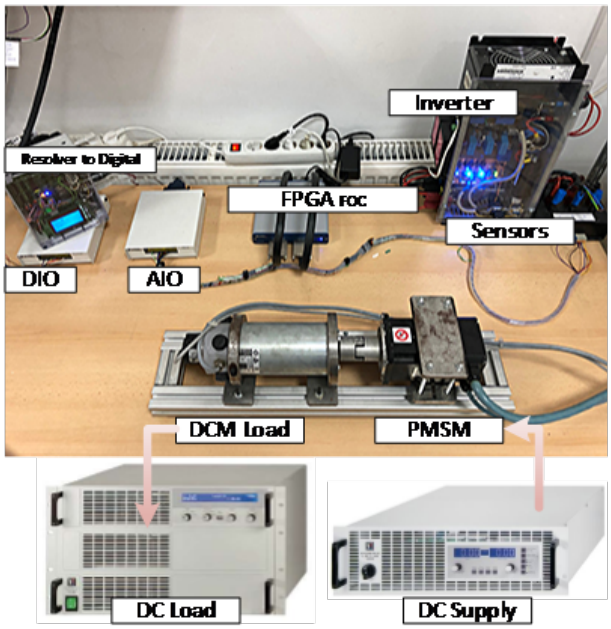

Figure 3.14: The laboratory test-bench setup.

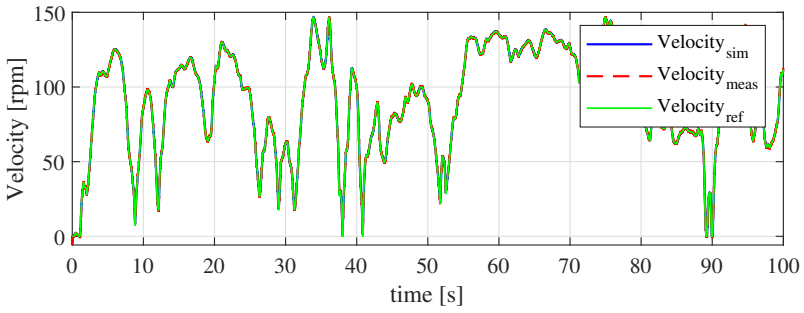

(a)

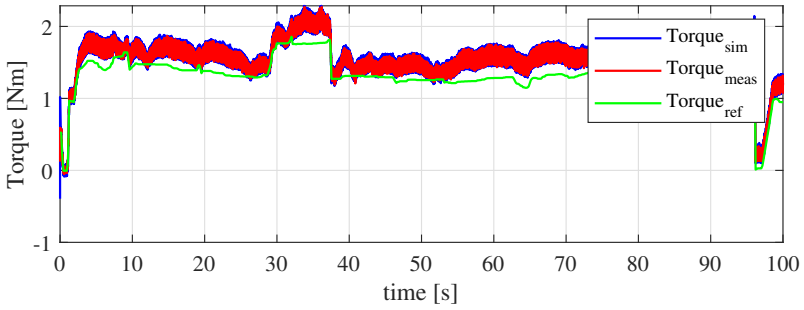

(b)

Figure 3.15: Motor speed (a) and torque (b).

can be noticed that the developed electromagnetic torque is bigger than the reference one because the machine has to deal, in addition to the load torque, with frictional forces that occur during its operation. As it is difficult to have a correct measurement of the electromagnetic torque, the developed is estimated based on the measured d- and q- axis currents. By considering the discussed aspects, it can be concluded that the the dynamical model created based on the surrogate models is able to produce results close to the experimental ones. Moreover, Fig. 3.16 presents the simulated and measured i_{d} and i_{q} currents. By examine the results, it is clear that the dynamic model performs with high accuracy, giving results close to the experimental ones.

3.6 Intermediate conclusions

The electromagnetic modeling methods of electrical machines were investigated here. The two classical models, the inductance based model and the flux linkage method were described. For the first model, the most simple one, the data is extracted using Frozen Permeability Method from electromagnetic simulations conducted at different currents and rotor positions. The second method, the flux linkage based model, uses fluxes ex-

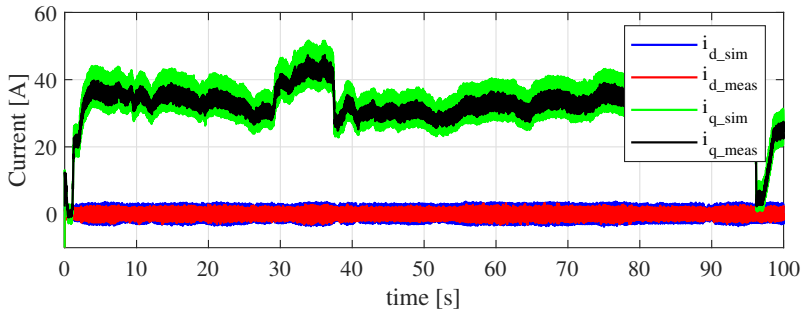

Figure 3.16: Predicted vs. measured quadrature currents.

tracted from electromagnetic simulations and included in the dynamical model with the help of 3D LUTs. Both models used for electromagnetic torque prediction (e.g., both average and ripple values) the torque values extracted from 2D FE simulations that are stored in LUTs. For the second model, two table inversion methods were compared and their accuracy was discussed. The third reduced order model proposed in this chapter relies on artificial neural networks. The model was constructed based on the flux linkage model, where the relationships between currents – flux linkage and currents – torque were emulated by an artificial neural network based model. The improvement brought by the introduced method was demonstrated by comparing it with the inductance based model (i.e., linear model) that showed a reduced capacity to predict both currents and torque ripples.

The machine learning based model was obtained by training the ANNs model using an adaptation data generation method. For that, the most suitable data dimensionality reduction technique was chosen. The two methods tested were Latin Hypercube Sampling and the Sobol sequence. The adaptive data generation process stopped when a prediction error under 1 [%] was reached. Two ANNs models were developed, one for currents prediction and the second one for electromagnetic torque prediction. By comparing the results obtained for different data sets, it was observed that the networks trained with data dimension of 220x61, where 220 represents the number of $i_d - i_q$ combinations and 61 the number of rotor positions, performed the best. For a more in-depth analysis, the 220 Sobol network was compared with the FE analysis. The results showed that by using the 220 Sobol network, the results were close to the FE ones, considered as reference, keeping the relative error under 1[%]. Moreover, the harmonic content of analyzed waveforms was not changed, compared with the FE results. At the same time, the computational cost was diminished with 50[%], meaning that the data set needed to build the surrogate model has been reduced by half using adaptive sampling, while

keeping the FE accuracy.

Regarding the real-time capability, because the model run time is negligible and the computational burden has been moved in the training stage, the developed dynamic model could be included in a real-time platform. The dynamic results were compared with the measured ones, showing that the proposed model is precise and suitable for hardware in the loop (HiL) test.

4. Analytical modeling and prediction of motor vibrations

The vibro-acoustic characteristics of electrical motors can be evaluated by either FE methods, analytical or semi-analytical methods. Even if the FE methods provide accurate results, considering non-linearity introduced by magnetic materials or specific geometries of the motor components, they are computational expensive and require some apriori knowledge coming from the expert. To prevent this, analytical methods can be used. Analytical methods are useful, especially in the concept stage, for the first evaluation of performance characteristics, where a fast computation is needed, or when the product is introduced in an optimization loop where thousand of designs are evaluated and the time cost is crucial. Therefore, analytical methods are employed to predict performance characteristics due to their ease of implementation and fast computations, saving precious time and resources and allowing an enhanced time-to-market.

Analytical approaches for estimating the vibro-acoustic behaviour of electrical machines have been discussed in several studies. In [59], the analytical method based on the theory of a simple supported beam carrying a sinusoidal distributed load. The same approach is identified in [20]. On the other hand, in [60], the analytical model for noise and vibration computation is derived from the theory of a cylindrical shell with ends free of constraints excited by a force harmonic.

This chapter presents an analytical method used to predict the stator deformations that occur at specific frequencies, called natural frequencies and the stator forced response. The analytical method uses a ring model to determine the structural characteristics. In the first sections, the analytical method used to compute the stator eigen-frequencies is compared with the FE method, taking into account two metrics - accuracy and time cost. For an objective analysis, the error for the first six global mode-shapes between the FE method and analytical one is performed. The last part presents the analytical and the semi-analytical methods to predict the stator vibrations. The analytical method uses the mode-shapes eigen-frequency results obtained from the analytical method, whereas the semi-analytical method uses natural-frequencies results from FE method in the analytical formulation of displacement computation. Two improvements in the semi-analytical formulation are introduced (i.e., introduction of tangential forces as radially exciters and consideration of tooth modulation effect in radial displacement formula). The comparison between semi-analytical and FE methods is performed for one design at steady state

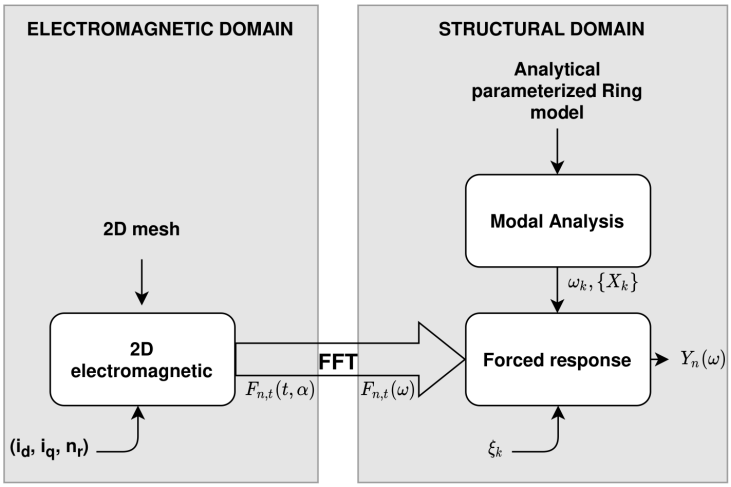

Figure 4.1: Analytical modeling workflow [19].

and during run-ups. The workflow of the analytical method for structural characteristics of the electrical motor under study is presented in Fig. 4.1. Once the electromagnetic forces are computed in an initial phase in electromagnetic domain, they are post-processed to obtain their frequency components. In parallel, the natural frequencies are determined in the structural domain. The remaining task is to use the resulting values and compute the forced response.

Therefore, the structural characteristics that are computed with the analytical method are the stator natural frequencies corresponding to stator global mode-shapes and the forced vibration response. The latter requires an external force to excite the structure and determine an oscillation at a specific frequency. This excitation forces are represented by the electromagnetic forces that are coming from the electromagnetic domain, where 2D FE electromagnetic analysis are conducted, as presented in Chapter 2.

4.1 Stator natural frequencies

The determination of stator natural frequencies is of most importance in the vibration analysis of electrical motors. The vibration characteristics of the motor are defined by the natural modes and their corresponding eigen-frequencies. The analytical model can be used to roughly estimate the stator eigen-frequencies quickly. Different approaches have been used to analytically estimate these values. In [61], the stator core is treated as a thin ring. The stator teeth and stator windings can be considered as additional masses [60] or as individual entities with own mode-

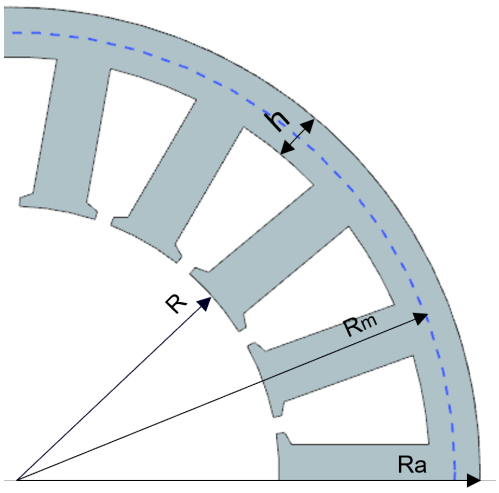

Figure 4.2: Stator ring and teeth geometry.

shapes [59]. An accurate prediction of motor eigen-frequencies is a complex process mostly because of the geometry complexity and non-linear material properties. For this purpose, in this thesis, the stator structure, composed by core, teeth, winding and frame, is simplified to a ring model [59], graphically represented in Fig. 4.2. The windings and the teeth are taken into account in this analysis as additional masses.

For the considered metal ring, the deformation patterns can be identified in Fig. 4.3. Mode 0 or breathing mode caused by the spatial harmonics of the electromagnetic forces of order 0 is depicted in Fig. 4.3 (a). Mode 2 caused by a exciting force of order 2 is presented in Fig. 4.3 (b), Mode 3 in Fig. 4.3 (c) and Mode 4 in Fig. 4.3 (d). All presented modes are represented when the stator doesn't deflect in axial direction. Mode 0 (breathing mode) is characterised by a uniform deflection of the stator in the radial direction. Mode 2 (ovalisation mode) is distinguished by the deflection on an elliptical trajectory, with four poles. Mode 3 is represented by a triangularisation of the structure, while mode 4 deflects on a eight pole pattern.

Considering the geometry presented in Fig. 4.2, the global eigen-frequencies $f(n,0)$ of the stator are determined analytical as follows:

$$f(n,0) = \begin{cases} f(0,0) = \frac{1}{2\pi R_m}\sqrt{\frac{E}{\Delta\rho}} \text{ for } n = 0 \\ f(1,0) = f(0,0)\sqrt{\frac{2}{1+k^2\frac{\Delta_m}{\Delta}}} \text{ for } n = 1 \\ f(0,0) = k\frac{n(n^2-1)}{\sqrt{n^2+1}}\frac{1}{\sqrt{1+k^2\left(\frac{n^2-1}{n^2+1}\right)\left[3+n^2\left(4+\frac{\Delta_m}{\Delta}\right)\right]}} \\ \text{for } n \geq 2 \end{cases} \tag{4.1}$$

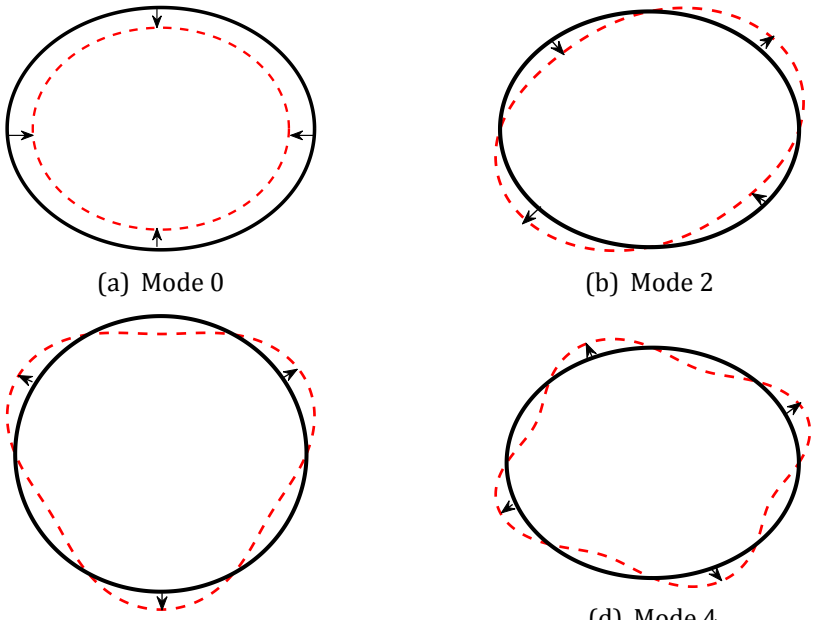

(a) Mode 0 (b) Mode 2

(c) Mode 3 (d) Mode 4

Figure 4.3: Generic metal ring mode shapes.

where: n represents the stator global mode-shape, R_m is the stator mean radius, E represents the stator material Young's modulus and ρ stands for its mass density.

The constant k is defined by a function of the stator yoke height h and the stator mean radius:

$$k = \frac{1}{2\sqrt{3}} \frac{h}{R_m}, \tag{4.2}$$

In 4.1, the stator weight is taken into account by the introduction of two additional constant, Δ and Δ_m, defined by:

$$\begin{aligned} \Delta &= 1 + \frac{G_z + G_w}{G_y}, \\ \Delta_m &= 1 + \frac{Q_s}{2\pi R_m} \frac{12 b_z h_s^3}{h^3} \left[\frac{1}{3} + \frac{h}{2h_s} + \left(\frac{h}{2h_s} \right)^2 \right] \frac{G_z + G_w}{G_z}. \end{aligned} \tag{4.3}$$

where h_s is the stator tooth height, b_z is the mean tooth width , G_z stands for the teeth weight, G_y represents the yoke weight, G_y represents the windings weight and Q_s is the number of stator slots.

It is worth mentioning that the analytical ring model can only be applied for isotropic materials in order to determine the natural frequencies of the stator ring. Moreover, it can capture only the in-plane global

modes. The global modes are characterised by a deformation of the ring model as a simple beam vibrating in a transverse direction, a bar in torsion or as a rod deflecting in longitudinal direction [62], [19].

4.1.1 Natural frequency results comparison

The analytical model is compared with the FE model in terms of eigen-frequency results in order to determine its accuracy. For that, the natural frequencies obtained for the motor under study (one stator design case) that in analytical method is seen as a steel ring with the parameters presented in Table 4.1, are analysed and compared with the FE method. The eigen-frequency relative error, $f_{(x,0)_{err}}$, between analytical method results, $f_{(x,0)_a}$, and FE based analysis eigen-frequencies, $f_{(x,0)_{FE}}$, is determined as: $f_{(x,0)_{err}} = 100 \cdot (f_{(x,0)_a} - f_{(x,0)_{FE}})/f_{(x,0)_{FE}}$. The resulting natural frequencies of the first six global modes are presented in Table 4.2. Here, the relative error between the analytical and the FE model is presented, where the FE results are considered as reference. As it can be observed, the analytical values are lower than the FE results. In terms of accuracy, the analytical method gives the most accurate results for mode 0. In this case, the natural frequency of mode 6 is also computed with a decreased error, while for the other mode shapes, the error is high, taking values bigger than 18[%]. However, for a fair comparison between the analytical and FE methods, an analysis for more than one design was conducted and the statistical distribution of errors identified in [63].

Table 4.1: Stator ring parameters

Parameter	**Value**	**Unit**
E	2.07×10^5	$\mathrm{N/mm^2}$
ρ	7829	$\mathrm{kg/m^3}$
$\mathrm{R_m}$	0.0412	m
$\mathrm{b_z}$	0.0068	m
$\mathrm{G_y}$	0.387	kg
$\mathrm{G_z}$	0.471	kg
$\mathrm{G_w}$	0	kg
$\mathrm{Q_s}$	12	-
h	0.053	m

By analysing the results, a general conclusion that can be drawn is that the analytical method underestimates the values of the global eigen-frequencies. Moreover, it can be observed that the smallest relative error is for mode-shape (0,0), where the mean error is -1.86%. This is because mode 0 of vibration is more influenced by the yoke width, which is the

Table 4.2: Natural Frequencies Results

Method	Mode 0	Mode 2	Mode 3	Mode 4	Mode 5	Mode 6
FE	13592	1184	3091	5337	7347	8229
Analytical	13338	868.7521	2295	4045	5970	7979
Error	-1.86%	-26.62%	-25.75%	-24.2%	-18.74%	-3%

main parameter that influences the ring frame in the analytical method. Therefore, as the analytical method approximates the stator as a ring model with the width given by the yoke dimensions, the analytical method has the biggest accuracy in this case. Other modes of vibration are more influenced by the tooth geometry parameters, which are hard to capture by the analytical method, where their influence is given by a tooth mass factor. The biggest error is encountered for the cases of global modes 2 and 3, where the mean error is -26.62% and 25.75%, respectively.

4.2 Stator vibration response

As described in the previous sections, the air-gap electromagnetic force with their radial and tangential components, excite the structure and cause vibrations. When the frequency of the exciting forces are close to the stator natural frequencies, the vibration amplitudes are high and is often described as the resonance phenomenon. In an electrical machine, the radial component is approximately one order of magnitude higher than the tangential one, thus the tangential component is usually neglected when computing the displacement. The radial and tangential force densities expressed in $[N/m^2]$, extracted at initial rotor position for the full air-gap length, computed at nominal conditions can be identified in Fig. 4.4.

When computing the vibrations of the stator, firstly the air-gap forces are extracted from 2D FE analysis. Once the forces are generated, they are post-processed using Fast Fourier Transform (FFT) to obtain the frequency – domain values. Afterwards, the displacement amplitudes are determined based on the theory for a simply supported beam carrying a sinusoidally distributed load [59]. Because the error between the eigen-frequencies obtained with analytical method and FE is not insignificant, as presented above, for the displacement computation, a semi-analytical method is used. For that, the semi-analytical forced response model combines the eigen-frequencies values obtained from a FE based modal analysis with the analytical displacement method. In the Maliti's analytical method, it is considered that the deformation coming from every mode n has an equal contribution to the total output displacement. The vibra-

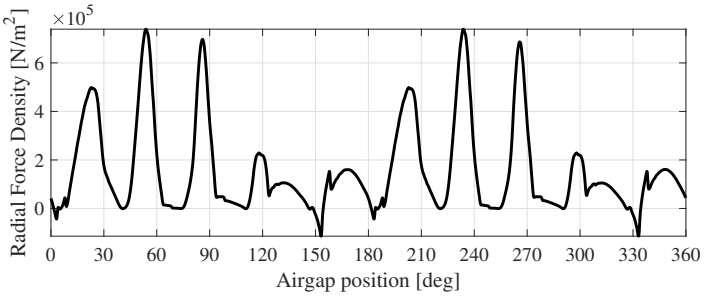

(a)

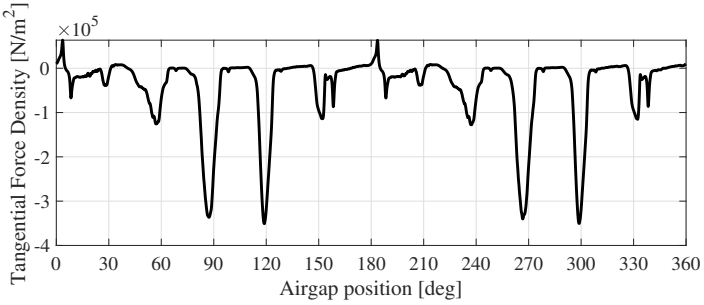

(b)

Figure 4.4: Air-gap a) radial and b) tangential force densities at initial rotor position.

tion displacement amplitude Y_n for each mode n, obtained by applying the exciting force, can be written as [59], [20]:

$$Y_n(\omega) = \begin{cases} \frac{RR_m}{Eh} F_{r,n}(\omega)\eta_n, \text{ for } n = 0,1 \\ \frac{RR_m}{Eh}\left[\frac{1+3k^2(k^2-1)}{k^2(k^2-1)^2}\right] F_{r,n}(\omega)\eta_n(\omega) \text{ for } n \geq 2 \end{cases} \tag{4.4}$$

where $F_{r,n}(\omega)$ is the n^{th} spatial – harmonic amplitude of the radial force density F_r in the frequency domain, h is the stator height and η_n is the resonance factor that allows to introduce dynamic effects for the same harmonic:

$$\eta_n(\omega) = \frac{1}{\sqrt{\left(1-\left(\frac{\omega}{\omega_n}\right)^2\right)^2 + \left(\frac{2\xi_n\omega}{\omega_n}\right)^2}} \tag{4.5}$$

where $\omega_{n,F}$ is the frequency at which $F_{r,n}$ occurs and ξ_n is the mode n damping factor.

The final vibration response, $Y(\omega)$, is given by the sum of all displacements $Y_n(\omega)$, obtained for each mode-shape n.

$$Y(\omega) = \sum_{k=0}^{n} Y_k(\omega) \tag{4.6}$$

4.2.1 Improvements in the semi-analytical method

Even if the analytical method allows fast determination of stator natural frequencies and vibrations, being the most affordable computational method, it also relies on some simplifications that lead to errors, when comparing with FE method. Two major simplifications are performed when computing the displacement analytically. The first one is to not consider the tangential component of the air-gap forces that can excite the stator structure radially, from now on called tangential effect, and the second one is the assumption that a spatially – distributed force waveform of order n can only excite the circumferential mode shape of the same order. However, recent research work show that both effects can impact the displacement response and for different combination of slots-pole pairs, it can drastically impact the results.

4.2.1.1 Tangential effect

In the analytical method for vibration computation, a common simplification is to take into consideration only the radial component of the air-gap force density, because the tangential component is smaller than the radial one [60].

However, even if the tangential force is approximately an order of magnitude smaller than the radial force, the tangential forces also contribute to the excitation and the radial deformation of the stator yoke. The tangential force of order $n = 0$ contributes to the torque production and has a negligible effect on the yoke deformation. Higher force waves orders, with $n \geq 1$, can excite, together with the radial component, the stator and create vibration of the structure [64]. Therefore, as the tangential forces are able to excite the structure, their effect on the vibration characteristics of the stator can also be considered, together with the radial component, to compute the forced response.

The insertion of tangential forces components in the analytical computation method is done by converting the tangential force to an equivalent radial force using a tangential factor, G_{t}, dependent on the stator geometric parameters [64]:

$$G_{\mathrm{t}} = Q_{\mathrm{s}} \frac{R_m - R}{2\pi R_m} \tag{4.7}$$

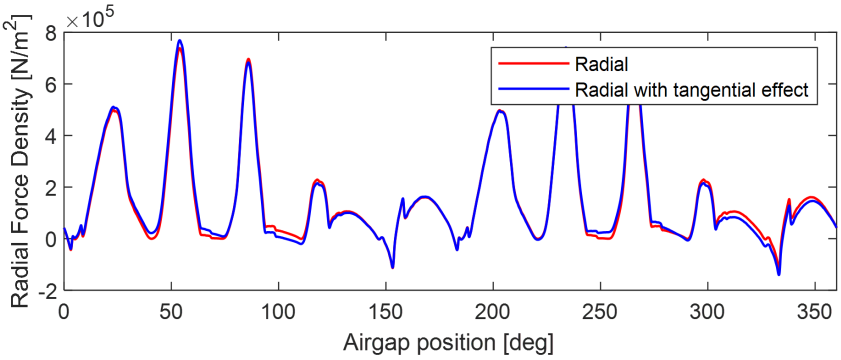

Figure 4.5: Radial force density.

The tangential factor is applied only on the tangential force components ($F_{\mathrm{t,n}}$) of order n, where $n \geq 1$ and $n \leq Q_{\mathrm{s}}/2$. For $n = 0$ and $n > Q_{\mathrm{s}}/2$, the tangential factor is zero. Hence, the force spectrum that takes into account both radial and tangential components of air-gap forces, $F^{*}_{\mathrm{r,n}}(\omega)$, is obtained as follows:

$$F^{*}_{\mathrm{r,n}}(\omega) = F_{\mathrm{r,n}}(\omega) - 2jG_{\mathrm{t}}sin(\frac{n\tau_Q}{2})F_{\mathrm{t,n}}(\omega) \tag{4.8}$$

where τ_Q represents the slot pitch angle, $\tau_{\mathrm{Q}} = (2\pi)/\ Q_{\mathrm{s}}$.

Comparing with the FE method, where both air-gap force components can be used to excite the structure, in the analytical method, the tangential forces are introduced in the mathematical expression with the help of the tangential factor. Afterwards, the tangential forces multiplied with the tangential factor are added on top of the radial forces. Figure 4.5 presents with red the radial forces exported from the FE electromagnetic analysis for one rotor position, whereas with blue, it can be identified the force used in the analytical method after the tangential effect was included in the radial force.

4.2.1.2 Modulation effect

In classical analytical approaches, it is generally considered that the principal contribution to the vibration response is given by the air-gap forces with low spatial orders and that the force waveform of order n only excites the circumferential mode with the same order [65]. For that reason, the high-order air-gap forces are neglected. However, recent studies demonstrate that a high force wavenumber could also cause a low circumferential mode deformation, in a same way as a low force wavenumber does. This phenomenon, known as the stator tooth modulation effect, can have a significant impact on the stator vibration characteristics,

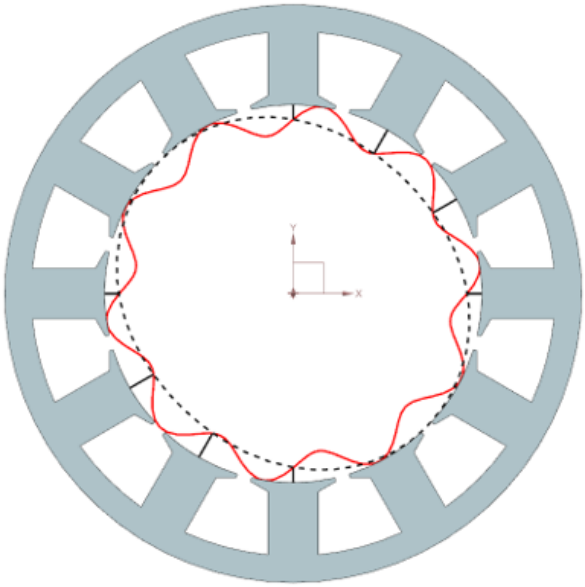

Figure 4.6: Illustration of stator tooth modulation.

as shown in literature. Therefore, the conventional analytical methods present increased errors, especially for machines like fractional-slot concentrated windings that present increased modulation effects. In [66], [67] and [68], the authors present analytical methods, validated by finite-element analysis and by experimental measurements, that take into consideration the effect of teeth modulation on the vibration results of PM motors. The presented results show that high force spatial orders also induce a low circumferential mode deformation. At the same time, it was proven that in order to obtain accurate results using analytical methods, this effect should be considered in the analytical vibration computation model.

The stator tooth modulation effect describes the way a high force spatial waveform number n is modulated into a lower order m, with $m = n - kQ_s$, where k is an integer chosen so that the modulated waveform number, m, is always within the Nyquist frequency. Based on the Nyquist-Shannon sampling theory, the modulated waveform number should be smaller than the Nyquist frequency, $|m| \leq |Q_s/2|$. This phenomenon is illustrated in Fig. 4.6, where for a 12 slots PMSM, a wavenumber of spatial order $n = 10$, represented with red line, is seen, after lumping the force, as a wavenumber of spatial order $n = -2$, depicted with dotted black curve.

The described effect is introduced in the analytical formulation of displacement computation by a modulation function [69], graphically represented in Fig. 4.7 for 60 wavenumbers. The modulation function

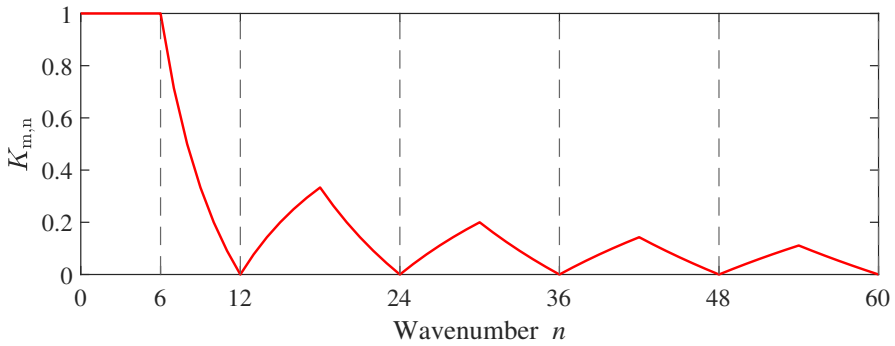

Figure 4.7: Modulation function.

has unitary value for waveforms smaller than $Q_s/2$, is null for multiples of Q_s and it is mathematically expressed as follows:

$$K_{m,n} = \frac{m}{n} \frac{sin(n\pi/Q_s)}{sin(m\pi/Q_s} \tag{4.9}$$

The modulation function is applied on the force spectrum modified with the tangential factor, $F^*_{r,n}(\omega)$, as expressed in (4.10). The force waveform of order n is adjusted to a force of order m, as described below:

$$F''_{r,m}(\omega) = K_{m,n} F^*_{r,n}(\omega) \tag{4.10}$$

4.2.2 Displacement Response Results Comparison

The displacement obtained using the semi-analytical approach is confronted with the forced response obtained by performing vibration synthesis analysis, with the workflow presented in Section 2.5.2. For the semi-analytical method, all four cases, without additional effects, from now on denoted with standard method, with tangential effect included known as tangential method, with modulation effect involved in the computation, denoted as modulation method and with both tangential and modulation effects (tangential and modulation model) are investigated. An examination at steady-state conditions of the motor under study, for 1800 rpm and forces extracted for $i_d = 0$A and $i_q = 50$A is performed, with the results, expressed in dB scale, shown in Fig. 4.8 only for the multiples of baseline frequency.

The presented results obtained for one design case at nominal and steady-state conditions show that the semi-analytical method tends to exhibit lower values of the displacement, compared with the vibration synthesis method. This is not the case at 900 Hz. At the same case, an improvement in the forced response results is obtained when additional

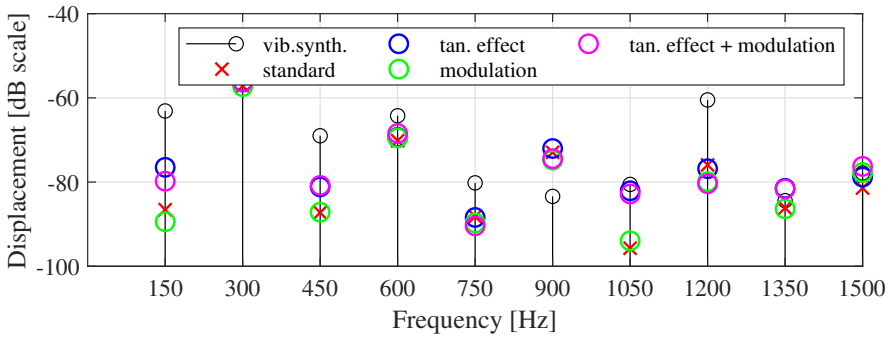

Figure 4.8: Comparison of displacement results for the vibration-synthesis and semi-analytical methods at 1800rpm.

effects are introduced, but a more substantial improvement is obtained when the tangential effect is included, as shown in Table 4.3. The displacement relative error $Y_{m,err}$ for each significant mechanical order m between the vibration-synthesis and semi-analytical results ($Y_{m,VS}$ and $Y_{m,SA}$) is determined as: $Y_{m,err} = 100 \cdot (Y_{m,SA} - Y_{m,VS})/Y_{m,VS}$. For the modulation effect, the results for this particular type of PMSM with 12 slots are not improved, but for topologies with increased number of slots, the introduction of modulation effect highly affects the result accuracy. As a conclusion, for the presented conditions of the machine under study, the analytical method with introduced modulation effect exhibits the closest results to the baseline method, the vibration synthesis.

Table 4.3: Displacement results errors expressed in percents ([%]) for one design at 1800rpm.

	Standard	**Tan. effect**	**Modulation**	**Tan. effect + mod.**
Peak 1	37	21	41.6	26.4
Peak 2	19.5	17	19.8	17.6
Peak 3	26.4	17	26.3	17
Peak 4	9.2	7.9	8.1	6.5
Peak 5	9.9	10.2	11.8	12.7
Peak 6	-12.5	-13.6	-10.3	-10.7
Peak 7	18.8	1.8	16.6	2.8
Peak 8	25.5	27	32	32.9
Peak 9	2	-3.4	2.3	-3.2
Peak 10	4	1.2	-0.15	-2

The results presented above are obtained for one specific rpm. However, the machine never operated at constant speed condition. Therefore, for a better understanding of the results values, the run-up obtained at

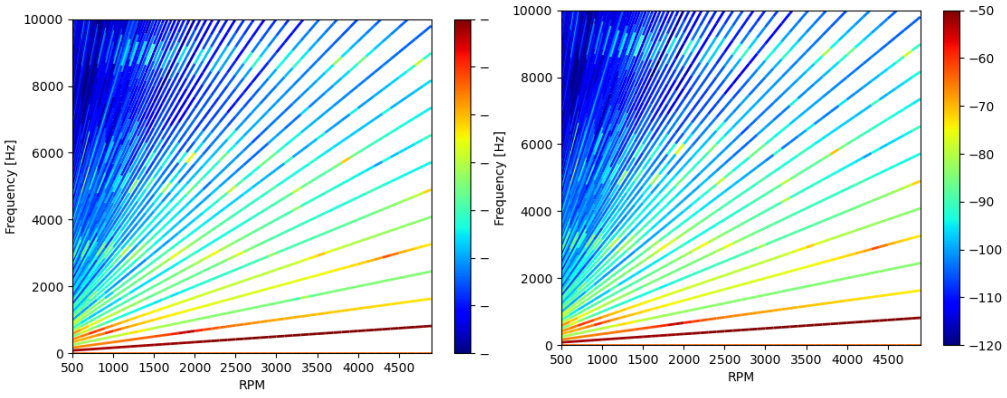

(a) Standard

(b) Tangential effect

Figure 4.9: Analytical methods comparison - Standard vs. Tangential effect.

different speeds is analysed. Figure 4.9 presents the standard analytical method in comparison with the tangential analytical one. From the run-ups, the orders are extracted. The mechanical orders of the standard analytical method is presented with red curves, while for the analytical method that includes the tangential effects, the orders are displayed with blue. A more significant difference is obtained for order 30 and order 60, as it can be seen in Fig. 4.10 (c) and (f), for specific rpms.

The run-ups for the analytical method that adds both modulation and tangential effects versus the standard method are presented in Fig 4.11. By extracting the orders and displaying the mechanical orders of the standard analytical method with red and for the analytical method that includes the tangential and modulation effects with blue, a clearer difference is identified. Figure 4.12 shows that the analytical method with both discussed effects tends to give lower values for all presented orders.

As it can be observed in Table 4.3, the semi-analytical method tends to overestimate the vibration displacement values, compared with vibration synthesis method. The biggest error is found for the first mechanical order, where the maximum error is 21%.

4.3 Computational time considerations

The computational cost of both FE based and analytical analysis is an important indicator, especially in the early design stage. The computational time of each method is evaluated for a workstation with Intel Core

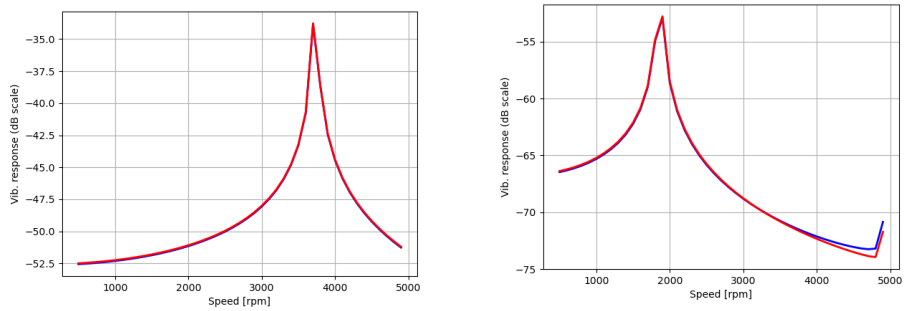

(a) order 10 (b) order 20

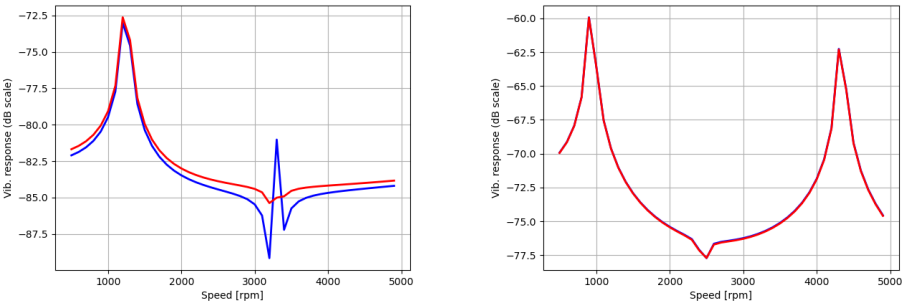

(c) order 30 (d) order 40

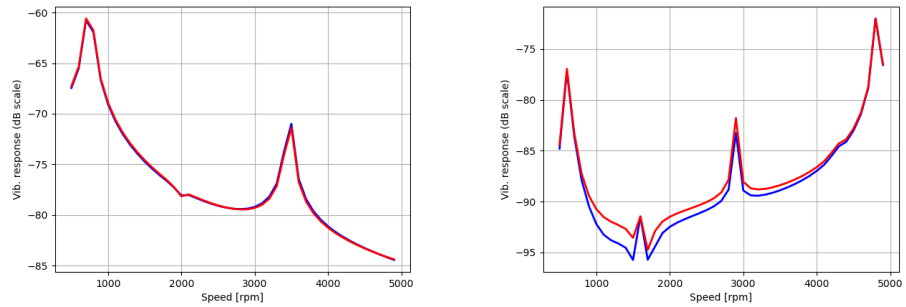

(e) order 50 (f) order 60

Figure 4.10: Mechanical orders for the standard analytical method (red) and tangential method (blue).

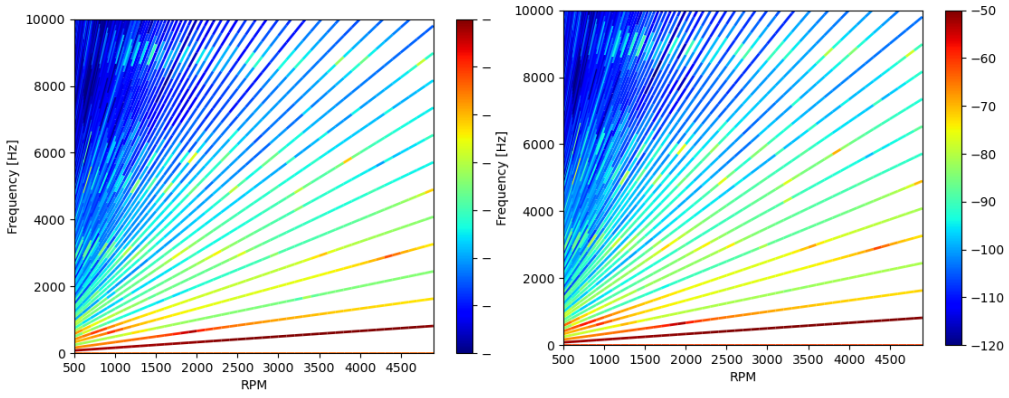

(a) No effects

(b) Tangential effect

Figure 4.11: Analytical methods comparison - Standard vs. Modulation and Tangential effects

i7-9850H CPU, 9^{th} generation, running at a frequency of 2.6 GHz, with 32 GB of RAM. Table 4.4 presents the computational burden expressed in seconds for one motor case, evaluated at steady state, for one operational point.

Table 4.4: Computational Time Comparison

Analysis	**Analytical**	**FE based**
Force Computation	161 s	161 s
Modal Analysis	0.2 s	102 s
Displacement Response Standard	0.36 s	183 s
Displacement Response Tangential	0.44 s	183 s
Displacement Response Modulation	0.5 s	183 s
Displacement Response Tan+Mod	0.6 s	183 s

For the displacement response using analytical method, the forces are extracted from an electromagnetic analysis. By analysing the results, it can be noticed that the FE models are more time consuming, comparing with the analytical ones. It is worth mentioning that both standard analytical approach and the improved methods (with included tangential, modulation, modulation and tangential effects) have close computational times. Besides the presented computational time, the designer has to have some a-priori knowledge and also consider that the FE models require additional time for building, parametrisation, meshing, analysis setup. In comparison, the analytical methods are easy to implement and

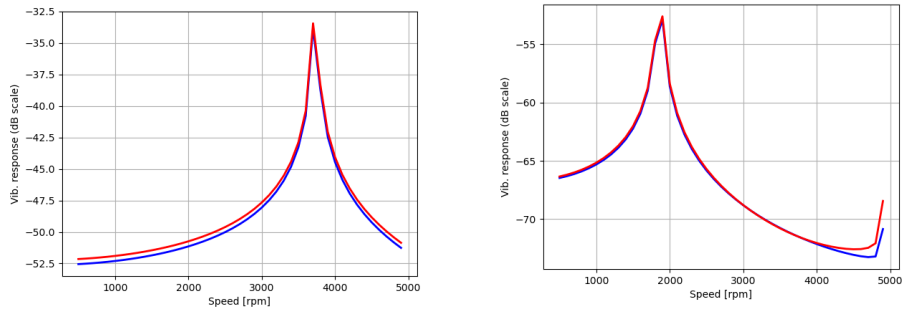

(a) order 10 (b) order 20

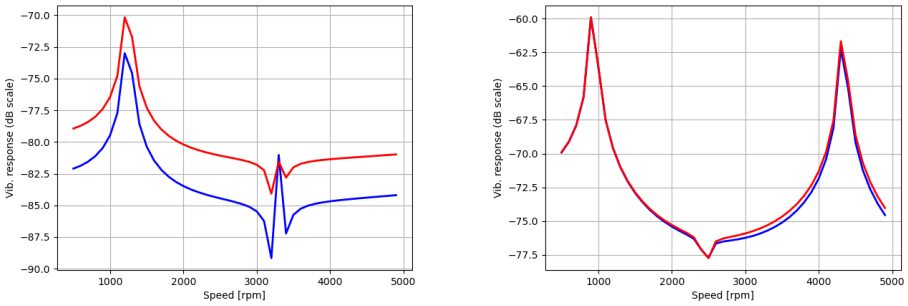

(c) order 30 (d) order 40

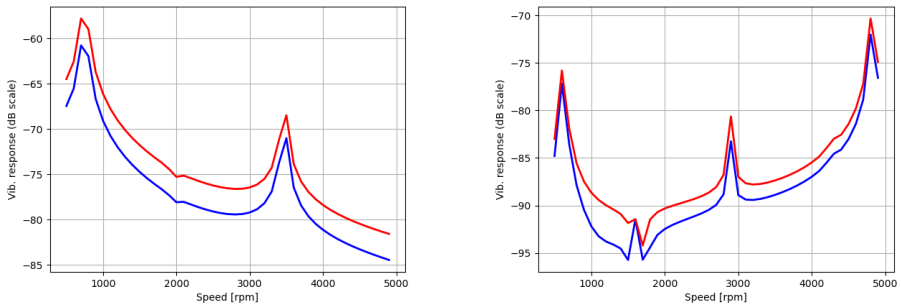

(e) order 50 (f) order 60

Figure 4.12: Mechanical orders for the standard analytical method (red) and modulation+tangential method (blue).

easy to use.

4.4 Intermediate Conclusions

The analytical method for prediction of motor structural characteristics (i.e., the stator natural frequencies corresponding to stator global mode-shapes and the forced vibration response) was discussed in this chapter. For this purpose, the stator structure was simplified to a ring model with the windings and teeth taken into account in the analytical method as additional mass factors.

For the natural frequencies, the relative error between the analytical and the FE model, considered as reference show that the analytical values are lower than the FE results. By analyzing the eigen-frequency relative error, $f_{(x,0)_{err}}$, between analytical method results, $f_{(x,0)_a}$, and FE based analysis eigen-frequencies, $f_{(x,0)_{FE}}$, it was observed that the analytical method underestimates the values of the global eigen-frequencies. The smallest relative error encountered was for mode-shape (0,0), where the mean error was -1.86%. The biggest error was encountered for the cases of global modes 2 and 3, where the mean error was -26.62% and 25.75%, respectively.

The stator vibration computation started by extracting the air-gap forces from 2D FE analysis that are post-processed using FFT to obtain the frequency – domain values. The displacement amplitudes were determined based on the theory for a simply supported beam carrying a sinusoidally distributed load. Two major simplifications are commonly accepted are to not consider the tangential component of the air-gap forces that can excite the stator structure radially, from now on called tangential effect, and the assumption that a spatially – distributed force waveform of order n can only excite the circumferential mode shape of the same order. However, for this work, both effects are taken into account for the displacement response. The conclusion about the displacement methods accuracy can be drawn by computing the displacement relative error $Y_{m,err}$ for each significant mechanical order m between the vibration-synthesis and semi-analytical results ($Y_{m,VS}$ and $Y_{m,SA}$). The results show that the semi-analytical method tends to overestimate the vibration displacement values, compared with vibration synthesis method. The biggest error is found for the first mechanical order, where the mean error is 22.1%. The semi-analytical method that includes the tangential effect give the most accurate results.

Finally it was noticed that the computational cost of FE models is higher. By comparing the two methods, it was noticed that once the forces are extracted from FE analysis, the analytical method computes the dis-

placement response instantly, in less than one second, whereas the FE method requires two more minutes. Analytical methods are fast and less accurate, compared with FE models. They can be used to evaluate the characteristics of a system, when the computational time is crucial, while keeping a margin of error for the results. The analytical methods ae suitable especially in the design stage, for the first evaluation of performance characteristics, where a fast computation is needed, or when the product is introduced in an optimization loop where thousand of designs are evaluated and the time cost is critical.

5. Surrogate models to ease the design process

The design process of an electrical motor is a complex task that involves contribution from different departments that focus only on one domain. This makes the design process a multi-physic, multi-disciplinary problem, where different physics must be analysed to develop a reliable, robust and high-performance design. In a first stage, the electromagnetic expert tries to obtain the best electromagnetic characteristics from one design. However, that design needs to met thermal, structural and NVH requirements that are in conflict with the electromagnetic targets, competing against each-other. Limited possibilities are available at the end of the design process to optimise the NVH characteristics and keep the electromagnetic performances. Besides that, the computational cost of the design process is high due to the iterative steps and the involvement within optimisation loops of 2D and 3D FE models, known as time consuming.

An original solution to the classical design workflow is presented in this Chapter. The proposed solution allows to predict the multi-physical characteristics of electrical machines, ease the decision making early in the design stage and reduce the product time-to-market.

This Chapter is structured as follows: in the first section, the available current solutions for electrical machines characteristics prediction are reviewed. Afterwards, the developed original workflow that allows for multi-physical forecasting of electrical machines attributes is described thoroughly. The last part is dedicated to the validation of the proposed solution by comparing the predicted results of optimised designs with the FE based ones, taking into account accuracy and time cost. The final conclusions are drawn in Section 5.9.

5.1 Surrogate models applied in the design process

The conventional method to design an electrical machine relies on optimisation [70], where the geometric parameters of a model, most of the times a FE model, are automatically modified within a design space with specified intervals and constraints. The FE method allows to model complex behaviours and elaborated geometries, but they come at the expense of high computational cost. When evaluating the optimal design of a model with high number of DOFs, the traditional optimisation process can jeopardize the result quality. This is because the number of optimisation designs are decreased, in order to reduce the time cost, and the global optimum combination of DOFs is not reached. On top of that, the

process is not scalable. If a minor change is performed in the optimisation conditions, the process must be repeated [71].

A solution to the discussed issues comes from machine learning (ML) domain. Fast models, also known as surrogate models or data-driven models, have been developed in the recent years to emulate the bevahiour of electrical machines and predict their characteristics [52]. Sampling methods are used to fill the input space of FE models and extract the data used to train the machine learning models. Therefore, looking from the optimisation design perspective, the computational burden is moved from the design stage to the data generation phase and the prediction process becomes instantaneous, as ML models running time is negligible. In this context, multiples characteristics coming from different domains can be identified earlier in the design cycle and an optimal, robust design can be achieved by identifying and reducing the system's sensitivities.

Methods based on machine learning models that aim to reduce the FE method computational time are proposed in studies published in the last years. Surrogate models based on artificial neural networks or statistical analysis that use multiple correlation coefficients present reduced computational effort and improved optimisation results [72], [73]. Surrogate models have been successfully applied to perform tolerance and sensitivity analyses of machine designs, reducing the FE dependance of the conducted multi-objective optimisations [74]. It has been shown that the electromagnetic targets, such as average torque and torque ripple, back electromotive force or magnetic field can be approximated as well from design parameters values using surrogate models [75], [76], [36].

For the structural and NVH targets, various works focused on surrogate models. In [77], the electrical machines airborne vibrations are modeled using a data-driven structural model. The developed model is successfully integrated in both design stage for optimisation purposes and system-level simulations. The vibro-acoustic behaviour of electrical machines, focusing on sound pressure levels, are predicted with the help of machine learning models in [78] and [79]. It is also proven the advantages of replacing FEA with surrogate models for future design and optimization problems of the same motor.

However, all the above described examples focus on only one physics, either electromagnetic, thermal or structural. A multi-physical approach is not discussed. The multi-physical characteristics prediction is found only in [80], where a series of KPIs, maximum torque, critical field strength, costs of active parts and sound power are included in a data-aided, deep learning meta-model. The model takes motor cross-section images as input to build the machine learning model. Even the results are predicted with high precision, the accuracy of this method directly influenced by

model hyper-parameters settings and input image resolution. The hyper-parameters can be indeed optimised during a sensitivity analysis, but the precision of the input data still remains a problem that affect results accuracy, training costs, storage memory and model running time. As expected, the presented results show that the model performs well only when the training data set has a high pixel resolution., meaning that this method is memory intensive, which should not be neglected.

5.2 Motivation

The proposed method aims at developing a solution that helps the experts to make decisions during the design stage of an electrical motor and ease the optimisation process to allow a faster time-to-market. This way, all the targets coming from different physics, electromagnetic, thermal, structural, NVH are brought earlier in the design cycle, where they can be optimised together and the designer can know if a design meets imposed targets or not. For example, a design can have excellent electromagnetic characteristics, but poor NVH levels. By knowing this behaviour in the early stage design, the motor is optimised until it reaches the best trade-off between analysed targets. This way, it is not needed to go with a cross-section design in the late stage design or even in prototyping phase to know its behaviour, reducing both costs and time-to-market.

The proposed solution relies on developing machine learning models that predict the motor performances, such as torque, back emf, losses, stator natural frequencies, maximum stress experienced by rotor, vibration characteristics from input geometrical parameters, in the early stage design. The main difference between the presented machine learning model and the ones found in the literature is the multi-physical feature of the developed model. Another important feature of the developed model is to predict the NVH characteristics during run-up. Geometric parametric models are employed to evaluate the multi-physical performances of an electrical machine and generate training data. Individual machine learning models are developed for each physics involved that are latter integrated into optimisation routine to enable the design process.

5.3 Methodology

Predicting the machine performances, such as electromagnetic values, losses, structural characteristics, is essential when designing an electrical motor in order to propose suitable solution to improve the behavior as soon as possible, in the early stage design, and save time and resources. However, in order to achieve this, a multi-physical modeling approach is

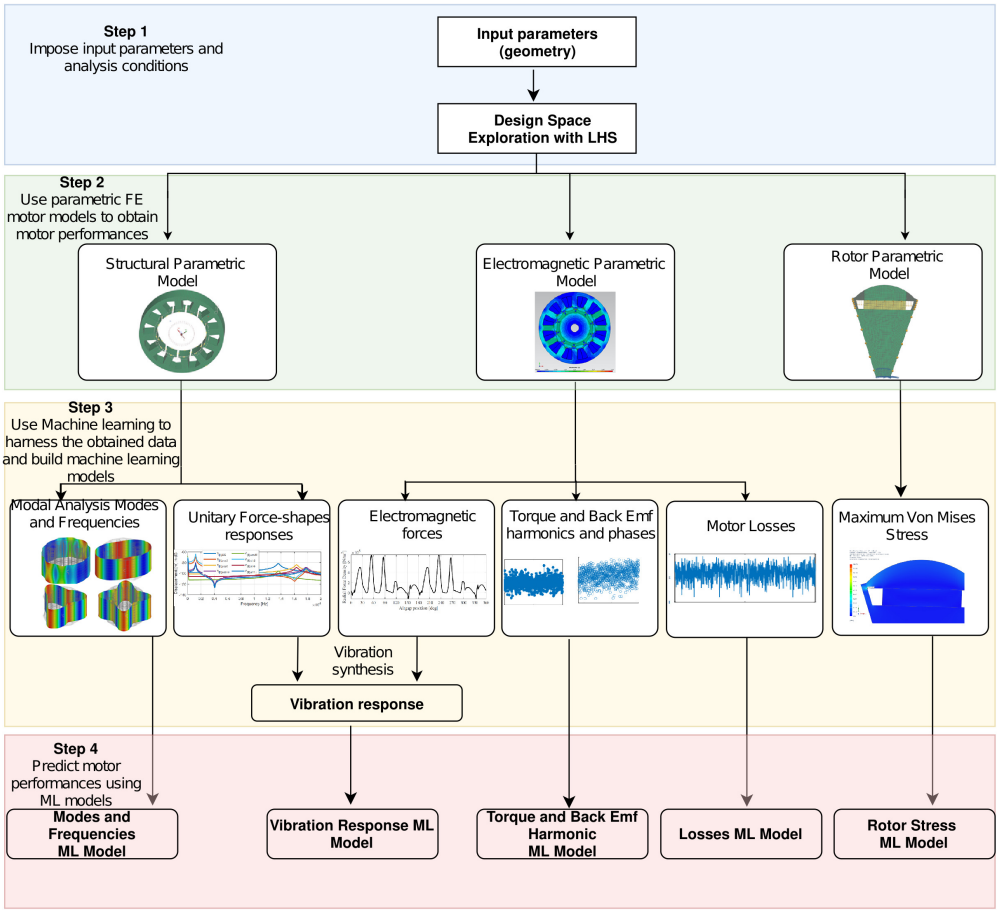

Figure 5.1: The process of generating Multi-attribute machine learning models.

needed to evaluate the motor performances. The proposed multi-physical modeling workflow is presented in Fig. 5.1.

Firstly, the input space is sampled using Design of Experiments (DoE) techniques. Afterwards, FE analysis are performed in multiples domains to obtain the data needed to train the machine learning models. Parametric 2D FE motor model is employed for electromagnetic analysis, the structural analysis make use of 3D parametric stator model and the 3D rotor parametric model is used to obtain the rotor maximum stress values. The 3D stator parametric model can be identified in Fig. 2.10, the 3D rotor parametric model is depicted in Fig. 2.11, while the 2D motor parametric model is shown in Fig. 2.9.

The 2D electromagnetic model is introduced in a data generation loop with the objective to extract electromagnetic performances (i.e., electromagnetic torque, back electromotive force) and motor losses. The elec-

tromagnetic analysis is performed at steady-state operation conditions (i.e., 1800 rpm, i_{d}=0A and i_{q}=50A). During the 2D electromagnetic analysis, only the stator DOFs are modified, while the rotor and magnet geometry parameters and material properties are kept constant. The stator DOFs are modified in the same manner in the electromagnetic and structural domains. In parallel, the 3D structural stator parameterised model allows the extraction of structural characteristics (i.e., mode-shapes and their corresponding natural frequencies and stator vibration response). The data is obtained by modifying the model geometry parameters according to the input space samples. The sampling technique determines a variation series of motor original geometry. New designs are generated by changing the stator DOFs (i.e., TWS, YT, SOAng, TGD and SO) using the LHS sampling method, while the stack length (L_{stk}), the inner and outer radii, together with material properties remain invariant, as explained in Section 2.6.2. Therefore, the stator structural mode-shapes and their corresponding eigen-frequencies are obtained from 3D FE modal analysis simulations carried out on the stator core.

Another parallel process consists in analysing and extracting the rotor Von Mises maximum stress values that appear under maximum inertial loads conditions. The four dimensional input space defined by rotor DOFs, $\mathrm{w_{mag}}$, $\mathrm{h_{mag}}$, $\mathrm{w_{bridge}}$, $\mathrm{h_{bridge}}$, is sampled using the same technique, LHS. The rotor DOFs variation limits are presented in Table 2.3. A series of designs are generated based on the original 3D rotor parametric model.

Afterwards, once the data is generated, the resulting electrical motor performances are harnessed by approaching various machine learning algorithms. For each physics involved, multiple algorithms are used to developed machine learning models. The prediction capacity and accuracy metrics of the resulting models are test in order to obtain the optimal machine learning model for each physics.

5.4 Data Generation

5.4.1 Electromagnetic Analysis

2D FE electromagnetic analysis are fulfilled in Simcenter Motorsolve. In order to capture all the important phenomena, a mesh with a proper density is defined. As the mesh density is inversely proportional to the solving time and impacts the results accuracy, this metrics must be carefully chosen. Therefore, the mesh characteristics are set based on the speed-accuracy trade-off that gives the association between analysis time and model fidelity. Each simulation is conducted at a speed-accuracy trade-off of 3 out of 10, where 1 is the fastest and 10 has the most accurate

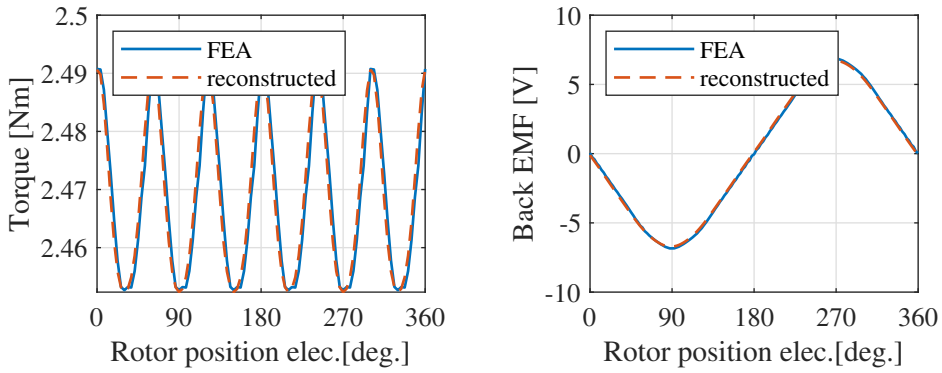

Figure 5.2: Electromagnetic torque and the back emf wave-forms extracted from electromagnetic FE analysis (blue line) for JT=4.39935 mm, TWS=6.9565 mm,SO=1.8815 mm, SOAng=116.65 deg., TGD= 0.98125 mm and the corresponding reconstructed wave-forms from the most important harmonics (red line).

level. An increased mesh refinement is employed in the air-gap. Based on these assumptions, for the selected accuracy level, one 2D analysis time lasts approximately 3.5 minutes. Each analysis is done for the nominal operation conditions, with a fixed value of speed equal to the nominal one and correlated with the nominal currents expressed in the $d-q$ reference frame.

The models are introduced in a data generation loop and at the end, the data is stored and post-processed. The values intended to be obtained from the 2D analysis are the electromagnetic motor performances - generated torque and back electromotive force (back emf), simultaneously with the machine losses. The obtained electromagnetic targets extracted from the FE numerical evaluation of the motor under study with following imposed geometry parameters, JT=4.39935 mm, TWS=6.9565 mm,SO=1.881 mm, SOAng= 116.65 deg, TGD= 0.98125 mm are displayed in Fig. 5.2 with blue lines.

The process of developing multi-attribute machine learning models that help with the decision making in the design process assumes that an appropriate algorithm is used at the lowest computational time cost. By analysing the data obtained for the 2D analysis, it can be observed that the results are time-dependent. Therefore, a machine learning algorithm appropriate for time-series data should be considered. However, this type of models introduce additional complexity and have high training times, as they include the time as one of the dimension [81]. To simplify the problem, a harmonic model can be used instead, removing the time-dependency of data. The resulting data set will be discrete. Hence,

a machine learning algorithm suitable for discrete data sets is chosen, reducing the model complexity and the computational burden in the learning phase, in contrast with the time-dependent machine learning model case.

The electromagnetic data sets is therefore post-process by applying the discrete Fourier decomposition on the torque and back electromotive force wave-forms. The obtained discrete data-set, consisting of harmonic order amplitudes and phases in function of design parameters, is stored for its later use. The harmonic spectrum corresponding to the electromagnetic torque and back emf wave-forms presented in Fig. 5.2 and obtained for a combination of parametric design of JT=4.39935 mm, TWS=6.9565 mm,SO=1.8815 mm, SOAng=116.65 deg., TGD= 0.98125 mm is presented in Fig. 5.3. The figure introduces with blue the DC component of electromagnetic torque and the 1^{st} harmonic order of the back emf, and with red harmonics of higher orders that have diminished amplitudes. By analysing the figure, it can be observed that the DC, 6^{th} and 12^{th} harmonic orders have the most important contribution to the torque spectrum, while for the back emf, the most influential harmonic orders are the 1^{st}, 3^{rd} and 11^{th} orders. Therefore, in the training process, only the first three most influential harmonics, together with its phases, will be taken into consideration. This assumption is relevant, as we selected the harmonic order based on their amplitude in descendant arrangement while the other neglected harmonics have the amplitude close to zero. This observation is highlighted in Fig. 5.2, where with red lines are displayed the reconstructed torque and back emf time dependent wave-forms using the highest influential harmonic orders (with their corresponding amplitudes and phases). For the presented case, the torque trajectory was reconstructed using, besides the harmonics amplitudes, the harmonics phases (i.e., 0 deg. phase for the DC component, -5.83 deg. for the 6^{th} harmonic and 18.94 deg. for the 11^{th} harmonic order). The sames applies for the back emf. The wave-form was reconstructed using the 91.2 deg. for the 1^{st} harmonic, -86 deg. for the 3^{rd} one and -74.5 deg. for the 11^{th} harmonic. Moreover, as the wave-form of the back emf doesn't differ from on e design to another in term of phase, but only in term of amplitude, the three phases are constant and can be used accordingly for all the design of experiments cases.

5.4.2 Structural Analysis

The structural characterisation of the electrical motor under study is performed with the help of FE analysis. For that, a 3D structural parametric model of the stator is built within Simcenter 3D. The stator rep-

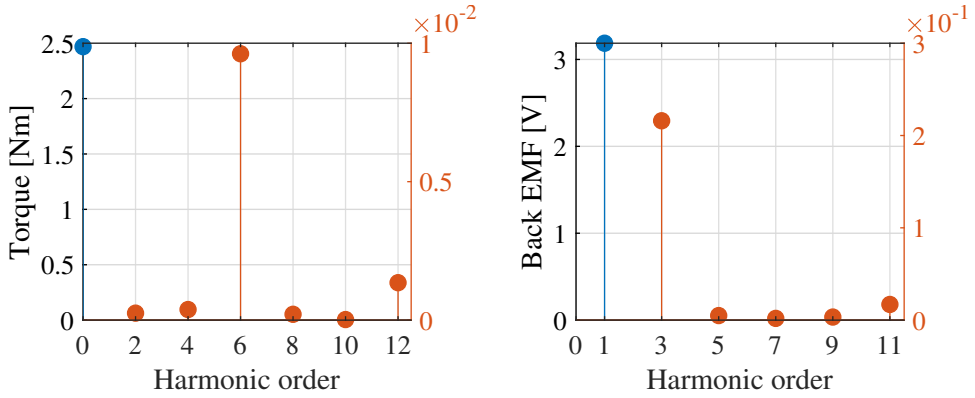

Figure 5.3: Electromagnetic torque and back emf harmonic orders obtained by applying FFT on wave-forms for JT=4.39935 mm, TWS=6.9565 mm,SO=1.8815 mm, SOAng=116.65 deg., TGD= 0.98125 mm.

resents the energy transfer path and it will be modeled alone, without considering other parts of the motor.

The first step in performing the modal analysis is to create the discretisation system. Starting from the parameterised CAD model, the 3D model is discretised into mesh elements, considering a trade-off between accuracy and calculation time. The number of elements on the outer stator diameter must be enough to identify all the desired mode shapes. Therefore, the 3D structural discretisation system is built with a mesh element of 1 mm size on the stator cross-section, 180 elements on the stator outer diameter and 8 mesh elements along the stack length. The total resulting mesh network consists in 14.568 3D eight-noded hexahedral solid (found under the CHEXA(8) name in Simcenter 3D glossary) and in 19.521 nodes. After the discretisation network is created, the material used to manufacture the stator is assigned to the stator model. Fo this particular case, the stator is made of steel with isotropic properties and a mass density of 7,829 kg.m^3. The value for Young's modulus is 206.940 GPa and the Poisson ration is equal to 0,288. The modal analysis is performed under free–free boundary conditions. The stator 3D structural model and the corresponding discretisation network are depicted in Fig. 5.4. Additionally, the analysis is conducted for a frequency band of 20 Hz to 20 kHz, representing the human hearing range. The modal analysis computational effort per one discretized 3D structural mesh, on a workstation having an Intel Core i7-9850H CPU running at 2.6 GHz, with 32 GB of RAM is approximately 2 min (1 min and 38 s).

The multi-physical analysis of the machine under study is conducted automatically, without needing human intervention to move from one do-

Table 5.1: Stator core mode-shapes.

FE Results	
(0,0)	(0,1)
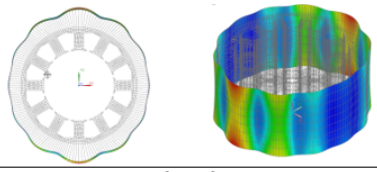	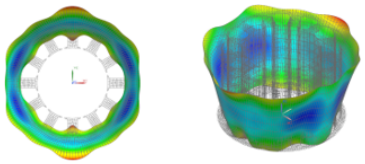
(2,0)	(2,1)
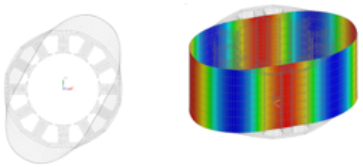	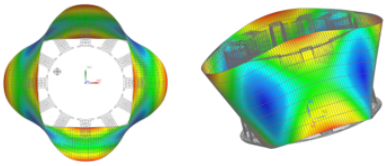
(3,0)	(3,1)
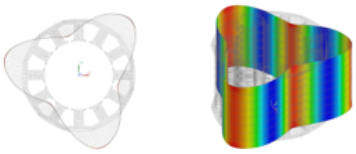	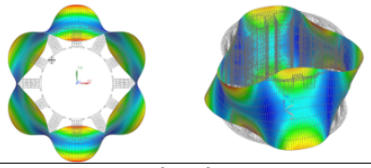
(4,0)	(4,1)
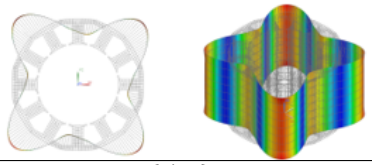	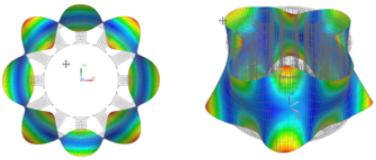
(5,0)	(5,1)
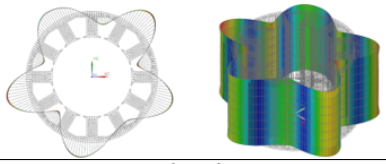	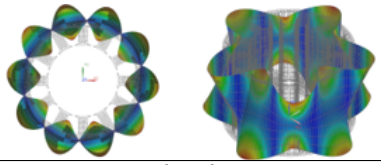
(6,0)	(6,1)
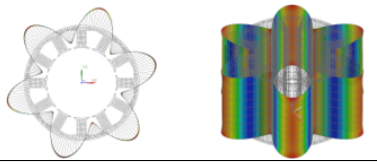	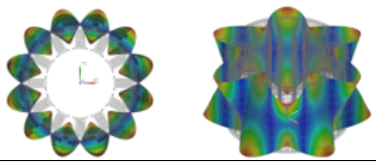

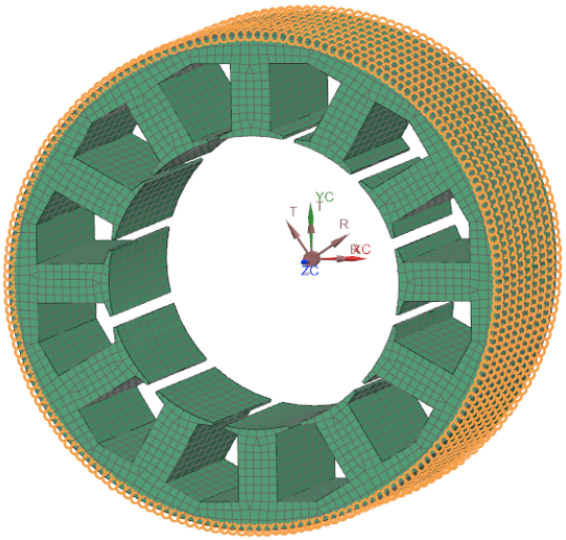

Figure 5.4: Parametric stator mesh discretisation network and the output nodes (marked with orange).

main to another, post-process the data or distinguish between the mode-shapes. The process allows to run massive simulations as well. The automathed workflow is enabled through a series of Python scripts that use the NX Open library supported by Simcenter 3D journaling tab. For the modal analysis, the automated process of identifying the mode-shapes follows a sequential procedure. Firstly, a new Simcenter 3D session is opened and the user specifications related to the analysis conditions, geometry parameters, mesh size, used materials, etc., are imposed to the model. Afterwards, the problem is solved taking into account the simulation requirements and the results are exported and post-process in order to get the mode-shapes and natural frequencies. More specific, the mode-shapes are identified by analysing the displacements of the nodes situated on the outer stator circumference (i.e., output nodes), marked in Figure 5.4 with orange, in radial, tangential and axial direction. The deformation pattern of the output nodes in all three directions is evaluated and the mode-shapes are recognized. Additionally, a selection between global and local modes is performed and the user can get the desired number of global modes. For this study, only the first six stator global modes were considered, as they have the most significant contribution to the vibration displacement response. The automated workflow is graphically represented in Fig. 5.5.

The stator mode-shapes for the baseline design that are recognized by the automated process by considering the deflections of the out-

put nodes are shown in Table 5.1. The mode-shapes present both circumferential deflection, m, and longitudinal deflection, n, and it is defined by the combination of both, (m,n).

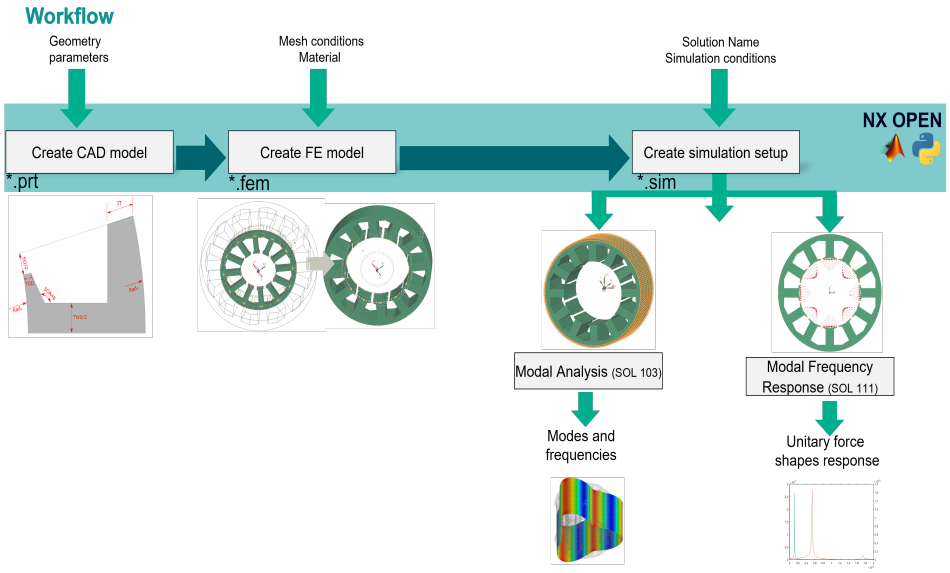

Figure 5.5: Representation of the automated workflow that allows to perform Designs of Experiments on the parametric models.

5.4.3 Losses Analysis

The multi-physical analysis continues with the determination of motor losses, performed within Simcenter Magnet on the 2D parameterised FE electromagnetic model used for the electromagnetic analysis. For this study, the motor losses distribution are quantified using FEA under nominal operating point. The 2D electromagnetic parametric model presented in Fig. 2.9 will be used as reference for the losses analysis, where the losses distribution in the motor components will be generated as a function of imposed input geometry parameters. The analysis of losses is an important step in the design process of an electrical motor, as they affect the machine performances through their heating effect. Exposed to increased temperature, the magnets can demagnetise, the winding resistivity is modified and the efficiency is decreased. For this process, the mesh and boundary conditions will remain the same as in the electromagnetic process. The losses are identified and exported using the same automatic multi-physical process. The geometric parameters are imposed, the simulation conditions consisting in nominal speed and currents are specified and the problem is solved. The final step consist in identifying the losses

and exporting their values. Afterwards, the obtained data is use to build a machine learning model that is able to predict motor losses from input geometrical parameters.

5.4.4 Rotor Stress Analysis

The rotor structure is subject to inertial loads that appear at high speed and that may cause a brake inside the structure that affects the integrity of the structure. The stress values that are developed inside the structure indicate the structure state of health. The stress gives information about the intensity of forces that act on the solid [30] and the analysis of distribution of this value inside the solid is performed for the worst case condition – the maximum rotational speed. The analysis should follow the evolution of stress, especially in the iron bridges, where it is expected to find the stress peaks.

5.4.4.1 3D FE Rotor Structural Model

The structural strength characteristics of the rotor belonging to the machine under study is evaluated through FE analysis. A parameterised CAD model allows to analyze multiples designs. A 3D parameterised structural model of the rotor is developed within Simcenter 3D. The structural analysis relies on the general motion equation expressed in 2.18. A force, consisting in the maximum rotational speed of the motor, is applied to the model. The force applied is considered constant and time invariant. Afterwards, appropriate materials are assigned to the rotor structure, composed of rotor core and magnets. The magnets are represented by a rare earth PM, NeFeB, characterised by the following mechanical properties: Young's modulus of 150 GPa, mass density equal to 7.5 kg.m^3 and the Poisson ratio equal to 0,24. The rotor core material is the isotropic steel with a mass density of 7,829 kg.m^3. The value for Young's modulus is 206.940 GPa and the Poisson ration is equal to 0,288.

Afterwards, the discretisation network is created, taking care to a assign finer mesh in the thin regions (i.e., iron bridges) where the maximum stress appear. In Simcenter 3D, a finer mesh is obtained in an efficient way with mesh controls. This way, the computational cost is not increased by imposing fine mesh in regions that are not that important, while focusing on regions where the possibility to get the highest stress peak is highly increased. Therefore, the expert can have the confidence of getting good stress results. However, even the mesh refinement must be carefully chosen so that the computational time is not increased too much. The 3D structural model and the mesh discretization is displayed

in Fig. 5.6 a) and the mesh refinement in the area of rotor bridges where high stress levels may appear is identified in Fig. 5.6 b).

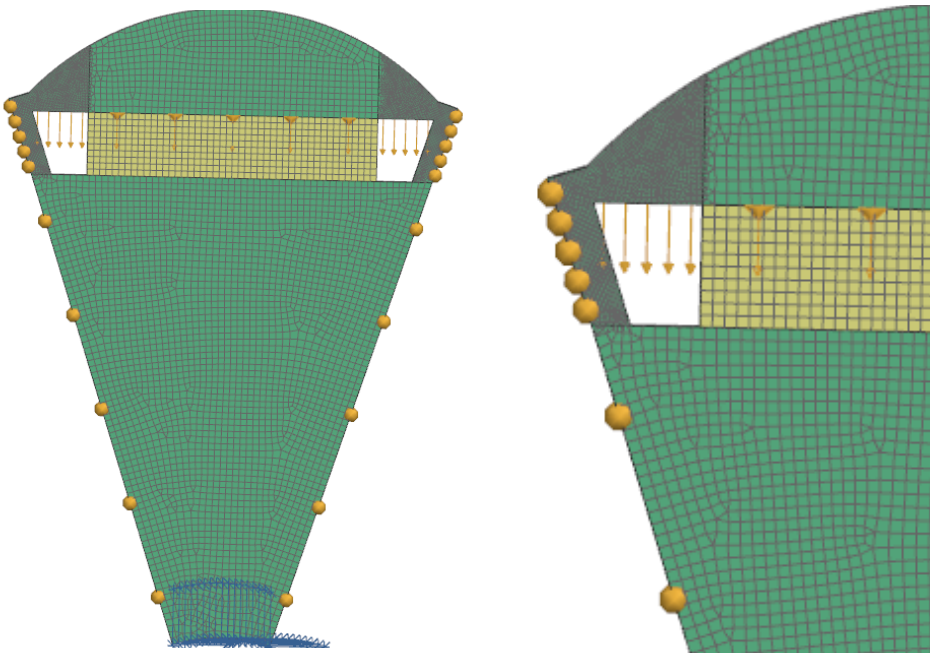

Figure 5.6: a) Rotor 3D mesh discretization, symmetric conditions and surface contact conditions. b) Mesh refinement near the iron bridges.

Once the structure is discretised, the model is represented internally by the connection between node points defined by the value of stiffness between them.The stiffness matrix is a singular matrix and it is constrained by the assigned boundary conditions. If the boundary conditions are set incorrectly, the stiffness matrix remains singular and the solver cannot solve the problem [83]. Therefore, the constraints must be carefully chosen.

The first applied constraint is a cylindrical restriction placed on the rotor inner axis. This allows the structure to deform freely in radial direction and locks the movements in axial and tangential directions. The constraint is applied on the inner circumference of rotor steel. The second boundary conditions is defined by the model type. If a symmetrical model is analysed, a second boundary condition must be applied, while if a full model is modeled, a single boundary limitation is enough. The complexity of a radial flux electrical machine model can be simplified by taking into account its magnetic symmetry and modeling only one symmetry sector. Therefore, a cyclic symmetry condition is applied on the rotor model in order to account for the parts that are not present in the analysis. Therefore, the resources allocated for one evaluation and the computational cost are

diminished. Moreover, surface-to-surface contact between the rotor and magnets are assigned so that any relative change between the two parts is controlled, resulting a compact and unitary structure. The boundary conditions and the surface-to-surface contact between the rotor and magnets can be identified in Fig. 5.6 b) with orange.

The analysis conditions are set for the worst case condition, with the following assumptions: the force applied is a rotational force given by the maximum steady-state speed; the dynamical forces and vibrations coming from the shaft are not considered; the permanent magnets are not subject to a different rotational load and are part of the rotor structure; the effect of temperature on rotor stress is not taken into account.

5.4.4.2 Von-Mises stress results

The values obtained from the stress analysis are the Von-Mises stresses. The stress distribution for the baseline rotor structure is identified in Fig. 5.7. For a 3D isotropic material, the Von-Mises is defined based on the normal stresses values in the x-, y- and z- directions (σ_x, σ_y, σ_z) and the shear stresses on the x face in the y- direction, x face in the z- direction and y face in the z- direction (τ_{xy}, τ_{xz}, τ_{yz}) [83]:

$$\sigma_{VM} = \sqrt{\frac{1}{2}[(\sigma_x - \sigma_y)^2 + (\sigma_x - \sigma_z)^2 + (\sigma_y - \sigma_z)^2 + 6(\tau_{xy}^2 + \tau_{xz}^2 + \tau_{yz}^2)}} \quad (5.1)$$

For the baseline rotor design, the maximum stress value is 128.76 MPa. This value is lower than maximum permitted Von-Mises stress value for steel, 250 MPa. Therefore, the design is valid and the structure keeps its integrity even at maximum speed conditions. Moreover, it can be seen that the maximum stress point appears, as expected, in the iron bridges, where the geometry presents thinner iron represented by the flux barriers.

5.4.5 NVH Multi-Physical Analysis

The radial displacement response is obtained by using a multi-physical workflow that relies on the vibration synthesis method [28] and presented in Section 2.5.2. This multi-physical process uses electromagnetic forces extracted from 2D electromagnetic simulations and unitary force shape responses obtained from a Modal Frequency Response Analysis (SOL 111 in Nastran, Simcenter 3D methodology) performed on the 3D structural stator model.

Therefore, in parallel with the 2D electromagnetic analysis that computes electromagnetic forces, the 3D structural analysis is performed

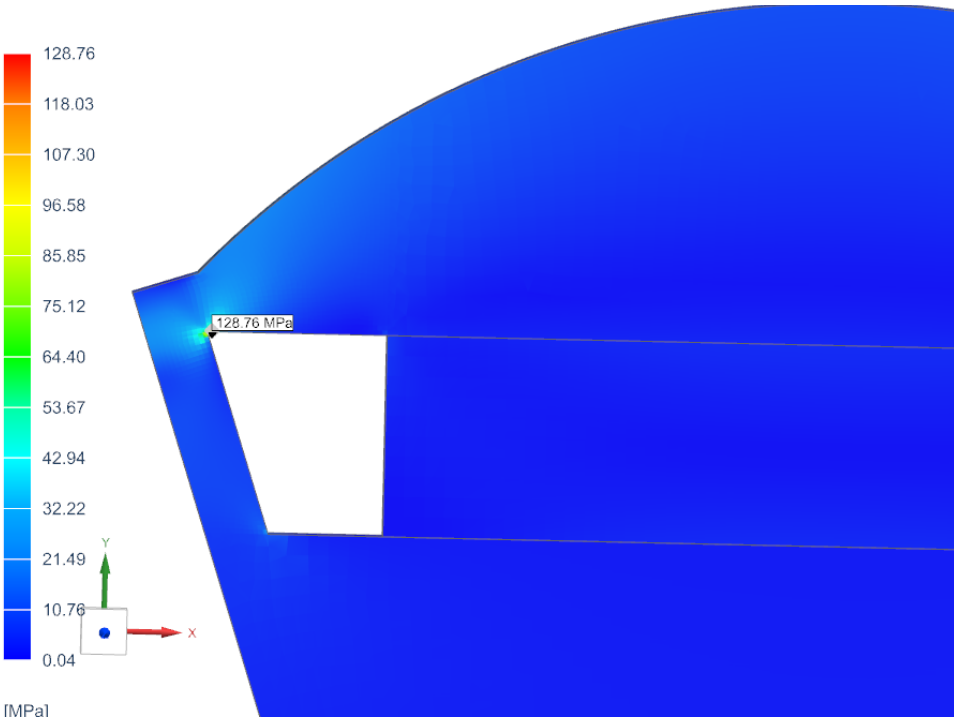

Figure 5.7: Maximum value of von-Mises stress.

on the stator core in order to determine the structure response for unitary force shape excitation. In this analysis, the generic force shapes with total energy per frequency line equal to 1 N are used and transferred to the 3D structural model. For that, the parameterised 3D structural stator model presented in Fig. 5.4 is introduced in simulation loops with different geometrical parameters for the multi-physical vibration synthesis process.

The sator model is discretised by paying special attention to the stator teeth nodes number in radial direction. The unitary force shape is applied on this nodes. As a trade-off between the accuracy and computational time, the stator teeth are divided into 8 equidistant points per tooth. The stator teeth structural mesh together with the nodes where unitary force shapes are applied can be identified in Fig. 5.8. On the left side figure, it is displayed the radial DC unitary force shape applied to stator tooth radial grid consisting in eight nodes, whereas in the right side figure, the tangential DC unitary force shape is identified. For each analysis, the frequency band is from 20 Hz to 20 kHz, corresponding to the human audible spectrum. Six pairs of $sin - cos$ force shapes (from 2 to 12 with a step of 2), together with the DC component, both radial and tangential directions, are applied on the stator structure to catch the effects

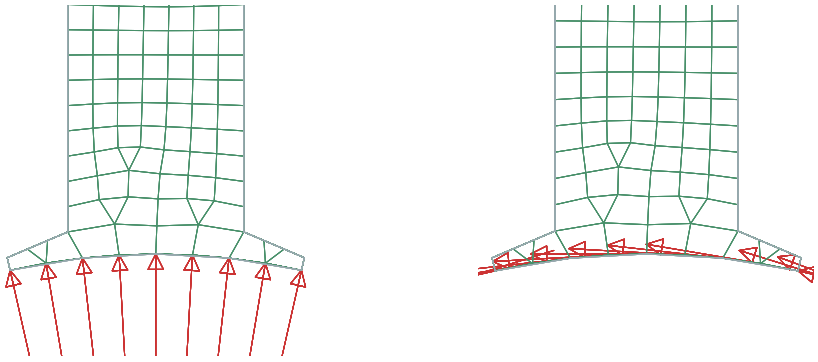

(a) (b)

Figure 5.8: Stator structure excited by (a) Radial DC unitary force shape and (b) Tangential DC unitary force shape.

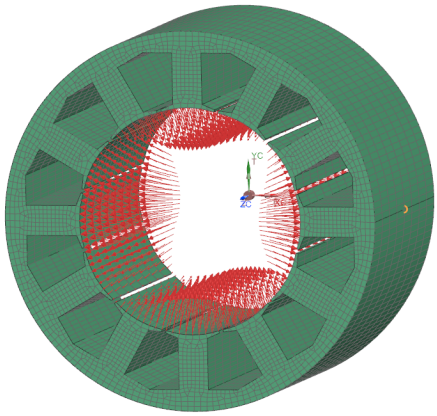

Figure 5.9: The force shape $F_{rad[I],cos2}$ acting on the 3D stator model and the output node O marked with orange, where the forced response is obtained.

of the most important spacial force harmonics. The unitary displacement values in radial direction for significant cases are presented for radial unitary force excitation in Fig. 5.10 (a) and in Fig. 5.10 (b) for tangential unitary force excitation.

5.5 Multi-Attribute Machine Learning Model Selection

The essential part when working with supervised machine learning algorithms used in this study to build surrogate models is to establish the connection between input parameters and output values. The data that is harnessed represents the system responses obtain by imposing

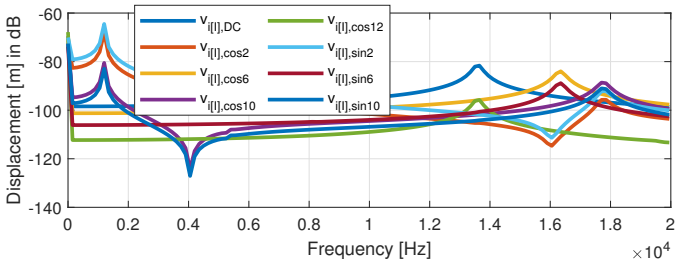

(a) radial direction response for radial unitary force excitation

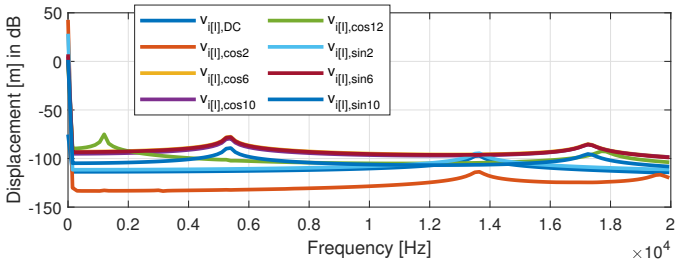

(b) radial direction response for tangential unitary force excitation

Figure 5.10: Displacement response for unitary radial and tangential force excitation.

the predictor variables (i.e., electrical machine geometrical parameters). Afterwards, depending on the feature of the exported system responses (i.e., discrete or time-series), the machine learning algorithm is selected. There are several phases that need to be accomplished when building the machine learning model: training, validation and testing. For each of these three phases, a series of data, obtained by splitting the original into training, validation and test samples is used. In the training phase, the data is harnessed, the model learns data particularities and patterns by fitting the parameters to the targets. This is followed by a validation phase, where the model parameters are tuned and the model capability to fit the training data set is evaluated. Finally, in the testing phase, the testing data, different from training and validation ones, is used to evaluate the final model performances.

It is already known that the machine learning model fidelity is highly dependent on the data type, as well as on the training data dimension. To study how different algorithms behave on the same type of data, three different machine learning algorithms usually implemented for regression problems are evaluated by using the data series acquired during a succession of 2D electromagnetic and 3D structural investigations. Five distinct surrogate models are created for each domain studied: one model

for electromagnetic torque and back emf harmonics, one for the stator eigen-frequencies, another model for motor losses, one for rotor stress and another one for stator forced responses.

For the first four targets, electromagnetic, losses, structural and stress targets, characterised by discrete data sets, three types of algorithms suitable for discrete samples are used. These algorithms are support vector regression (SVR), gradient boosting regressor (GBR) and Gaussian process regressor (GPR). In addition to this, the way a machine learning model benefits from a larger set of training data, its accuracy is tested for data sets that vary from 250 samples to 1000 samples, with a step of 250 samples. The data driven models are created using the Python Scikit-Learn library [84]. For each algorithm, the same steps are followed: the models are firstly trained, then validated and their accuracy is tested. The data set is split in 70% for the training process, while the rest of 30 % is used for testing. For the validation phase, a cross-validation method is applied [85]. The training data is divided in five folds and the model is trained using four of the folds, while the remaining one fold is utilized for the validation.

However, in order to build a machine learning model for stator forced response values, an algorithm dedicated to time series is necessary. The stator forced response is obtained in frequency domain during run-up (i.e., acceleration) and the vibration response depends on the rotor speed. Therefore, an algorithm that can process data with highly non-uniform characteristics (given by the peaks that appear due to resonance) and rotor speed dependency is employed to build the data driven model. In this study, the capacity of a deep learning method, represented by a Long Short-Term Memory (LSTM) network, to fit the vibration characteristics is evaluated.

5.5.1 Support Vector Regression (SVR)

One of the most popular machine learning model with applicability in both data classification for continuous data sets and for regression problems is Support Vector Regression (SVR) algorithm. SVR belongs to the class of supervised learning algorithms and relies on the principles of Support Vector Machine (SVM). An advantage of SVR, that makes it suitable for the data set available in this study, is its capacity to predict discrete values [86]. The algorithm searches for a function that can fit the relationship between input values and output results. In a two dimensional space, the function is a line and SVR finds the best first order function that can approximate the points. In multiple dimensions, the function is a hyperplane. Besides that, SVR allows to introduce a maximum error value,

called error limit or tolerance.

The objective function of this regression algorithm is to minimize the l2 norm, when the maximum error is limited to a maximum value, $min(\frac{1}{2}||w||^2)$.

Although SVR algorithm is simply to implement, there are a couple of aspects that must be taken care of during the training phase. The first one is the training data set size. SVR looses its feasibility when large training sets are used. The increase of learning time is given by a square-function of samples number [87] and the algorithm becomes computational high-priced for massive data sets. SVR becomes infeasible for data sets with more than 10,000 samples, due to the increased computational time. As an alternative, for massive data sets, Linear SVR or SDR regressor are feasible [88]. However, for this study, the classical SVR algorithm is a good candidate to build the machine learning model because the maximum size of available data sets used for training is 1000. For this type of data sets (i.e., small size), the SVR brings noticeable advantages: robustness to outliers, excellent generalization capacity, increased prediction fidelity and its accessibility.

It is worth mentioning that the SVR performance is sensitive to the relationship between number of features and number of training samples. If this value is greater than unity, which translates into a bigger number of features than the number of training samples, the SVR algorithm will not perform as expected. In this case, the situation can be avoided by reducing the dimension of the features. One of the methods that can be used to reduce the features dimensionality is Principal Component Analysis (PCA) [89]. This algorithm extracts the first n principal components with high eigen-values. A disadvantage of this method is that some information is lost and this leads to errors, in particular if the features and data connection is highly non-linear. A feature selection algorithm [90] can be used instead to decrease the dimension of the features. By performing the feature selection, the most relevant attributes of the data are chosen to build the machine learning model. By analysing the data available for training phase, it can be observed that the features number is considerable smaller than the number of samples and it doesn't require feature dimensionality reduction. The data sets under evaluation has a constant number of features, equal to nine for electromagnetic targets (i.e., torque harmonics amplitudes and phases and back emfs harmonics amplitudes), for the structural attributes, it is equal to six, one for stress values, and it is equal to seven for the motor losses data sets. The only number that varies is the number of samples, from 250 to 1000 samples, with a step of 250.

The optimal hyper-parameters used to train the data driven models are equal to C = 3.2 and the chosen kernel is the radial basis function,

rbf.

5.5.2 Gradient Boosting Regressor (GBR)

For discrete datasets, Gradient Boosting is a popular machine learning algorithms [91]. The tree-based algorithms, Random Forest and Gradient Boosting, are more robust to outliers, compared with linear models [92]. Gradient Boosting is a robust machine learning, as well, with features similar to Gradient Descent algorithm and Boosting [93]. The objective function of Gradient Boosting algorithm is to minimise the mean square error (MSE) or the mean average error (MAE).

The Gradient Boosting is characterised by an increased ability to approach the missing data problem, capability to deal with high non-linear data – features relationship, and possibility to use different loss functions. The GB uses multiples decision trees that are trained sequentially. At the beginning of the training process, the first decision tree presents a weak prediction. The model prediction capability is increased at each iteration and the prediction accuracy of the new tree is improved by tuning the weights of the previous tree. The machine learning model is derived by fusing the two decision trees [94] and the model's residual (i.e., the prediction error) is evaluated. If the error value is not acceptable, a new tree is trained for a better data classification, while the error is reduced. This process is recurrent and it stops when the error is minimized and an expected prediction is obtained.

A problem that occurs when working with GBR is that all errors, including the ones computed at extreme points, are minimised, leading to overfitting issues. Nevertheless, this issue can be avoided by using different methods, such as regularization or setting a maximum depth, or early stopping method [95, 96]. Another issue is represented by the fact that this method cannot be scaled, due to the fact that is trained within an iterative process. The process cannot be parallelized, because each decision tree uses knowledge gained during the training process of the previous one. However, a scalable end-to-end tree boosting system named XGBoost can be used for time-consuming processes that need to be scaled up. This method, XGBoost, diminishes the computational time and has scaling capacity of billions of examples in distributed or memory-limited conditions [97].

As already mentioned, the datasets have a discrete nature, characterised by a highly nonlinearity between data – features connection. Therefore, the GBR is an appropriate method for developing a machine learning model able to predict the motor performances. The overfitting problem is avoided in this case by setting a maximum depth of three be-

sides an early stopping constant that stops the learning operation when validation result is not improved after 20 iterations. The squared error function is set as the loss function for the training process.

5.5.3 Gaussian Process Regressor (GPR)

The Gaussian process is a popular non-parametric method that solves regression, probabilistic and classification problems [98]. As in this case the model covariance is imposed by the kernel function, a radial basis function is chosen. Among the most popular kernel functions are the constant kernel and quadratic exponential kernel, known as the radial basis function. The kernels give information to the Gaussian model. The GPR has the ability to perform with increased fidelity even for small datasets and is capable to provide uncertainty measurements on the predictions [99].

Another field where GPR performs well is, as presented in the normative modeling state of the art is the subject heterogeneity characterization [100, 101]. Normative modeling, which is a characteristic of some models to give the deviation of the resultant from the expected value.

GPR is an advanced and redoubtable machine learning algorithm, especially used to predict unseen values. An advantage of GPR is that it requires a small number of hyperparameters, in contrast with other machine learning algorithms. Therefore, it is able to solve different types of problems, even when only a small dataset size of data samples is available [102]. GPR decreases its efficiency if the number of features is more than a few dozens. Despite the presented aspects, the GPR is expected to perform very well for available data, as the number of features is small (i.e, the maximum number of features is nine, for the electromagnetic dataset). Another aspect that must be considered is the computational cost. In general, the Gaussian process is computationally intensive and they become problematical for large datasets. Nevertheless, GP regression is still computationally reasonable in the case of the small datasets under observation. In addition to this, the GPR algorithm was selected based on its features, such as flexibility in implementation, possibility to include a-priori information and details about the model (e.g., smooth, sparse, differentiable) by imposing distinct kernel functions. Again, the radial basis function (rbf) kernel is used for this model.

5.5.4 Long Short Term Memory (LSTM) for sequence-to-sequence prediction

Long short-term memory (LSTM) is a deep learning algorithm, belonging to the recurrent neural network (RNN) class. LSTM is applied in

classification, prediction, anomaly detection problems, being able to process both descrete data and time-dependent sequence data [103].

For sequence-to-sequence prediction problems, the model predicts a sequence based on an input sequence. In a one-to-one problem, the model can fit one input time sample to one output time step. A more difficult situation appears when a many-to-many problem needs to be solved. In this case, the model input consist in more than one samples and the prediction is a time sequence of data. Most of the times, the input size doesn't match the output dimension [104].

The open-source deep learning TensorFlow library is used within Python environment for machine learning surrogate model developing . The workflow is developed using the tf.keras API that ease the machine learning model developing process [105]. Within this framework, the model hyperparameters that need to be optimised are the number of layers, the number of neurons in each layer, the weight optimisation solver and the regularization parameter set to avoiding overfitting. The data set is split in 80% for training and 20 % for testing.

The architecture of the LSTM model consists in one input layer with 100 neurons, one hidden layer with 190 neurons and an output layer equal to the number of orders per each frequency. The model uses tanh function to activate the cell state. The model hyperparameters are set based on Adam optimizer that adapts the learning rate in function of past gradients and momentum [106]. The model is optimised to reduce the mean square of errors between true value and predictions.

5.6 Performance Indicators for Prediction Accuracy Evaluation

To evaluate the performance of each regression model, two statistical indicators are used, the coefficient of determination, denoted with R^2 and the mean squared error, shortly denoted with MSE. The first metric, R^2, gives the variation of the regression model. The model is able to predict with high accuracy when R^2 presents high scores and reduced scores indicate underfitting problems. The model has ideal fitting capabilities when R^2 score is 1. The R^2 coefficient is defined by the relationship between the predicted value of the $i-th$ sample, $\hat{y}_i$ and the corresponding true value, y_i, for a number of n fitted points with the mean value $\bar{y}_i$:

$$R^2 = 1 - \frac{\sum_{i=1}^{n}(y_i - \hat{y}_i)^2}{\sum_{i=1}^{n}(y_i - \bar{y})^2}, \tag{5.2}$$

where $\bar{y}_i = \frac{1}{n}\sum_{i=1}^{n} y_i$.

The second metric introduced to characterise the fitting performances of the machine learning models, MSE, is a risk indicator, that gives the average of the squares errors. The value of MSE is obtained by the square difference between the estimated values and the actual values, $MSE(y,\hat{y}) = \frac{1}{n}\sum_{i=1}^{n}(y_i - \hat{y}_i)^2$. The model fits data with high precision when MSE has values close to 0.

5.7 Machine Learning Models Capabilities Evaluation

Before introducing the developed machine learning models into the decision making process for design or into optimisation loops, they have to be evaluated. The most efficient surrogate models from the point of view of computational cost and accuracy are tested for each physics involved. Choosing the best method is dependent on its applicability. For efficient models, the computational time and the required resources must be cheaper than the FEA. The most laborious task when building machine learning models is the data generation part, the training process being negligible. Therefore, the objective is to find the machine learning model that uses the smallest dataset size that keeps an increased accuracy. Because the developed surrogate models are data-size dependent, their behaviour are evaluated on different database characterised by 250, 500, 750 and 1000 samples.

5.7.1 Electromagnetic values

For the first domain analysed, the electromagnetic domain, the values that are fitted are the torque and back emfs harmonics. The conversion to their corresponding time-dependent waveforms is done by using only the most important harmonic orders. Therefore, the surrogate models were learned to fit only the most influential torque harmonic orders, (i.e., DC TH, 6th TH and 12th TH), and the back emf harmonics (i.e., 1st BmfH, 3rd BmfH and 11th BmfH harmonic orders). The performance metrics that describe the quality of the developed models are presented in Table 5.2. As it can be seen, the R^2 and the MSE scores are identified for each created machine learning models using the discussed SVR, GBR and GPR algorithms successively trained using 250, 500, 750 and 1000 samples.

By observing the results, it is clear that there is a direct correlation between the discussed metrics values and the database size, independent of the used algorithm. The R^2 score is improving and the MSE error is reduced if the dimension of the dataset is enlarged. Besides that, by comparing the metrics obtained for different algorithms, SVR model is superior to

Table 5.2: Prediction capability of the machine learning models for electromagnetic attributes.

Samples/ Models		DC TH		6th TH		12th TH		1st Bmf H		3rd Bmf H		11th Bmf H	
		R^2	MSE	R^2	MSE	R^2	MSE	R^2	MSE	R^2	MSE	R^2	MSE
250	SVR	0.96	4	0.96	4	0.8	19	0.95	6	0.96	4	0.74	26
	GBR	0.92	8	0.94	6	0.82	18	0.93	7	0.94	5	0.76	23
	GPR	1	0	0.98	1	0.86	13	0.99	1	0.99	1	0.89	11
500	SVR	0.98	2	0.98	2	0.87	13	0.97	3	0.98	2	0.88	12
	GBR	0.96	4	0.96	4	0.88	11	0.97	3	0.97	3	0.76	23
	GPR	1	0	0.99	1	0.95	5	1	0	0.99	1	0.94	6
750	SVR	0.98	2	0.98	2	0.9	9	0.97	3	0.98	2	0.9	10
	GBR	0.97	3	0.97	3	0.9	10	0.97	2	0.96	4	0.84	16
	GPR	1	0	0.99	1	0.93	7	1	0	0.99	1	0.94	6
1000	SVR	0.99	1	0.98	2	0.9	9	0.98	2	0.99	2	0.98	2
	GBR	0.97	3	0.94	6	0.9	10	0.98	2	0.98	2	0.97	3
	GPR	1	0	0.99	1	0.95	5	1	0	1	0	0.99	1

the GBR model for all sample sizes. The SVR results are characterised by increased R^2 values, doubled by lower MSEs than the GBR. However, the best solution for this domain is the GPR model. GPR presents the higher accuracy and it is able to maintain a high fitting capability for all training sets. For more than 750 samples, the GPR presents great results, the R^2 score is higher than 0.93 and the MSE lower than 7%. To be more specific, for 750 samples, GPR has an increased score for the 12th TH, the R^2 being raised to 0.93, starting from 0.86 (for the 250 samples case), and the MSE values is decreased from 13% (for 250 samples) to 7%. The results for the 11th BmfH are improved as well, the R^2 value upgrates from 0.89 to 0.94 and the MSE diminishes from 11% to 1%. GPR presents perfect fitting capabilities for the 1000 samples case. The fitting accuracy is the highest in this case even for the third most important torque and back emf harmonics that presented less accurate values in the 750 samples case. Even if the data extraction task is more computationally expensive, the accuracy of the 1000 samples case pays the effort. The metrics scores for the for 12th TH are: R^2 is 0.95 and MSE 5%. At the same time, for the 11th BmfH, the R^2 score is 0.99, while MSE takes a value of 1% . Figure 5.11 shows the dependency between the essential torque and back emf harmonics and their actual target (original) values derived from the GPR 1000 samples machine learning model. Ideally, the dependency is characterised by a first order function (line) that divides the space into two equal parts. As it can be seen, the distribution of the values are closed to an ideal straight line.

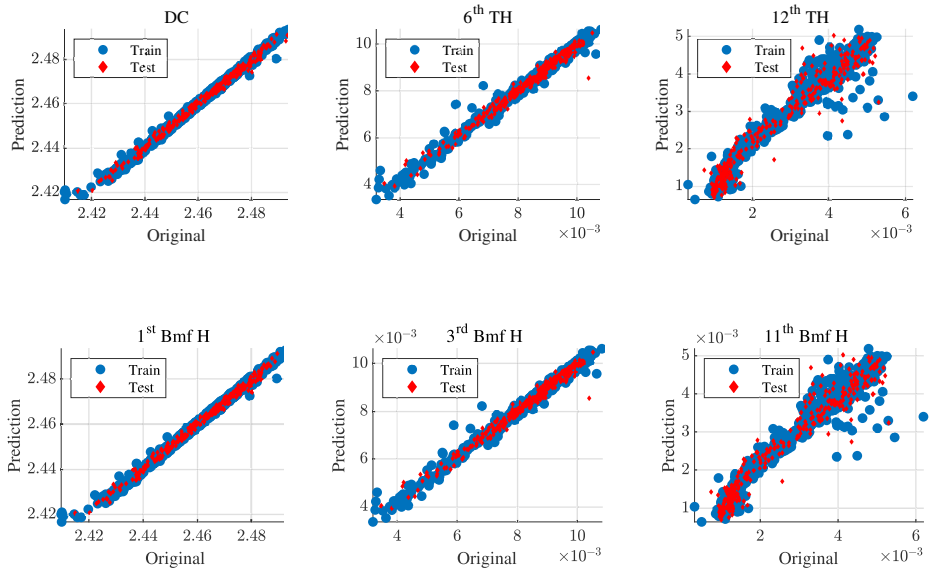

Figure 5.11: The GPR 1000 samples fitting capability for the DC, 6^{th} and 12^{th} torque orders and 1^{st}, 3^{rd} and 11^{th} back emf harmonics orders.

5.7.2 Structural values

The accuracy of the developed surrogate models for prediction of the stator natural frequencies is performed by analysing the obtained R^2 and the MSE scores. Table 5.3 presents these values specific to every regression method, SVR, GBR, GPR, successively trained using 250, 500, 750 and 1000 samples. The results show that all the machine learning models under test present high prediction scores, even when they are trained using the smallest batch size, 250 samples. Comparing the regression models, the SVR and the GBR methods enhance the R^2 score and the MSE with the increasing of the number of samples. On the other hand, the GPR method performs very well at 250 samples and remains robust to the change of the sample size. An important aspect to mention is that the metrics values start to saturate beyond 750 points for SVR and GBR. If data set is increased from 750 to 1000 samples, the R^2 and the MSE remain unchanged and the accuracy is kept constant. However, the computational time is considerable increased. Therefore, there is no need to increase the data set size, the model behaves very well for 750 samples. The R^2 values are 0.99 in the case of SVR and GBR models and GPR has a R^2 value of 1. SVR and GBR present MSE values between 0% and 1%, and GBR performs over them and exhibit a MSE value of 0%. The GPR based model is the best option, fitting the natural frequencies with the highest

precision, compared with SVR and GBR. The 250 samples GPR model is the best option, cosidering both accuracy and computational time. The model is able to perform at its best even for the smallest dataset due to the characteristics of the exported data. The natural frequencies are particularly impacted by the yoke thickness and tooth width and less sensitive to tooth tip angle, tooth tip height and the slot opening changes. Therefore, the complexity of the problem is reduced, compared with the electromagnetic case. Therefore, the dimension of the input data is reduced to 250 designs, obtaining good generalisation capacity and characterisation of new design performances. The prediction quality of the GPR 250 samples machine learning model is presented in Figure 5.12 for the first six global mode-shapes.

Table 5.3: Prediction capability of the machine learning models for structural natural frequencies attributes.

Samples/ Models		**Mode 0**		**Mode 2**		**Mode 3**		**Mode 4**		**Mode 5**		**Mode 6**	
		R^2	**MSE**	**R^2**	**MSE**	**R^2**	**MSE**	**R^2**	**MSE**	**R^2**	**MSE**	**R^2**	**MSE**
250	SVR	0.96	4	0.96	4	0.96	4	0.96	4	0.96	4	0.96	4
	GBR	0.98	2	0.99	0	0.99	1	0.99	1	0.99	1	0.99	1
	GPR	1	0	1	0	1	0	1	0	1	0	1	0
500	SVR	0.98	2	0.98	2	0.98	2	0.98	2	0.98	2	0.98	2
	GBR	0.99	1	1	0	1	0	1	0	1	0	0.99	1
	GPR	1	0	1	0	1	0	1	0	1	0	1	0
750	SVR	0.99	1	0.99	1	0.99	1	0.99	1	0.99	1	0.99	1
	GBR	0.99	1	1	0	1	0	1	0	1	0	1	0
	GPR	1	0	1	0	1	0	1	0	1	0	1	0
1000	SVR	0.99	1	0.99	1	0.99	1	0.99	1	0.99	1	0.99	1
	GBR	0.99	1	1	0	1	0	1	0	1	0	1	0
	GPR	1	0	1	0	1	0	1	0	1	0	1	0

5.7.3 Losses values

The capacity to predict the losses values (i.e., total—Tot, winding losses—Wind, iron—Iron, stator back iron—SBI, rotor back iron—RBI and magnet—Mag) is presented in Table 5.4. The R^2 and MSE indicators demonstrate that SVR has superior fitting accuracy in all cases, compared with GBR. The accuracy of all three regression models is evolving gradually with the increasing of the training set size. The lowest accuracy is obtained at 250 samples in the case of stator tooth losses. For 1000 samples, both SVR and GBR improve the values of R^2 to 1 and 0.99 and the MSE is reduced to a value under 2. The most suitable model to predict correct

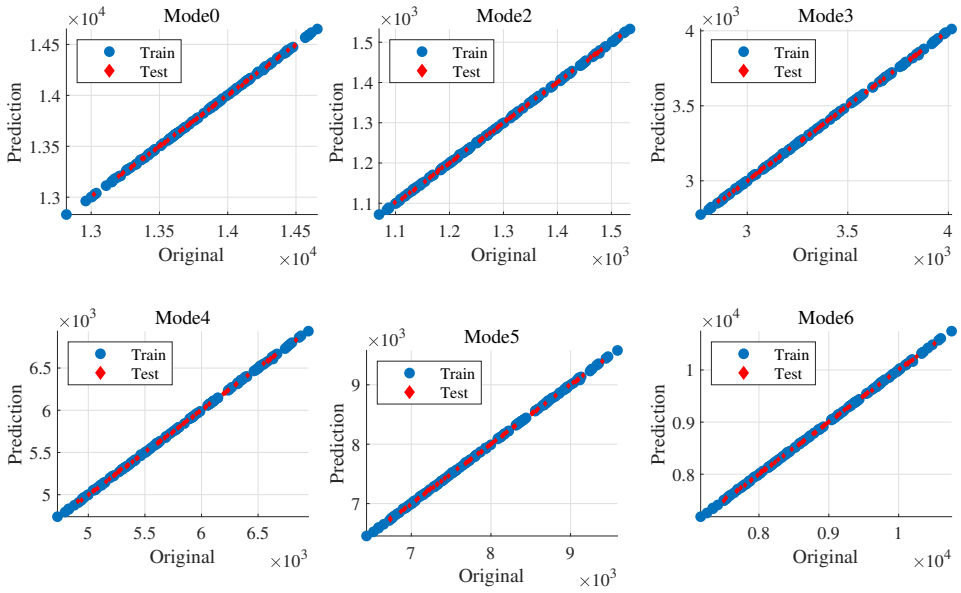

Figure 5.12: GPR 250 samples samples fitting capability for stator modes and frequencies.

the losses is GPR. Even for 250 samples, this method succeeds to predict the losses targets, presenting MSE with the highest value of 9%. The MSE characteristics are minimised to 1% for 500 samples and 750 cases and it drops to 0% for 1000 samples. GPR presents a perfect fitting ability for 1000 samples case, where the accuracy indicators are ideal, R^2 is 1 and MSE is null. The fitting capability of the developed GPR 1000 samples machine learning model for motor losses targets (iron, stator back iron, stator teeth, winding, magnets, rotor back iron and total losses) is identified in Fig. 5.13.

All performance indicators values are specific to the machine learning models build with the described number of stator DOFs. If the number of DOFs is diminished, the number of valid designs necessary for data-driven model development is considerably reduced. Similar, if the number of DOFs is expanded, the number of feasible designs must be increased too in order to keep the same accuracy level.

5.7.4 Stress values

Focusing on the rotor structure, a machine learning model is build to fit the stress results and the corresponding rotor geometry parameters. Due to the fact that the stress analysis is a binary classification problem, where a rotor structure can either resist to the applied inertial load or brake, the FE based results are categorized into one of two classes. There-

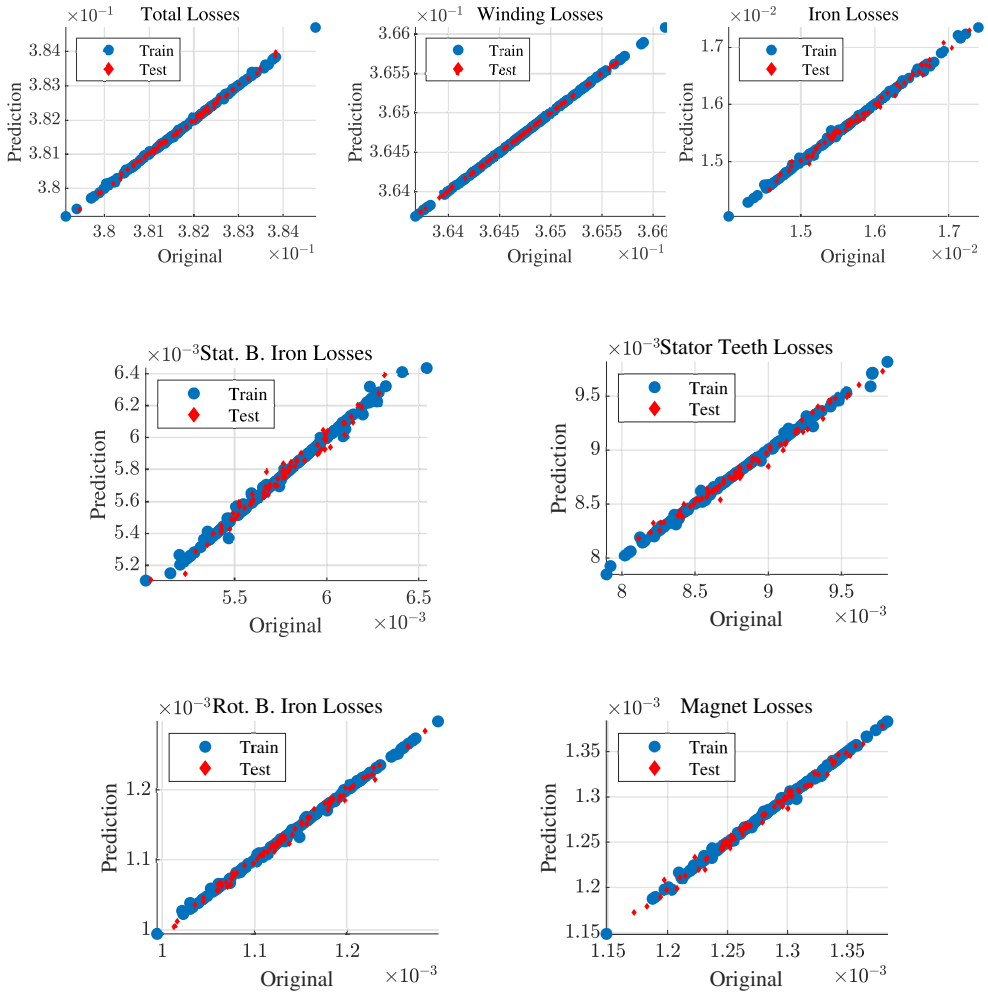

Figure 5.13: GPR 1000 samples samples fitting capability for total motor, winding, iron, stator back iron, stator teeth, rotor back iron and magnets losses.

Table 5.4: Prediction capability of the machine learning models for motor losses

Samples/ Models		Tot		Wind		Iron		SBI		ST		RBI		Mag	
		R^2	MSE	R^2	MSE	R^2	MSE	R^2	MSE	R^2	MSE	R^2	MSE	R^2	MSE
250	SVR	0.97	3	0.97	3	0.97	4	0.97	3	0.96	4	0.97	3	0.97	3
	GBR	0.87	13	0.94	5	0.9	10	0.87	12	0.92	8	0.88	11	0.87	13
	GPR	1	0	1	9	1	9	0.99	1	1	0	1	0	1	0
500	SVR	0.98	1	0.99	1	0.98	2	0.98	2	0.98	2	0.99	1	0.99	1
	GBR	0.92	8	0.96	4	0.93	7	0.9	9	0.94	6	0.93	6	0.92	8
	GPR	1	0	1	0	1	0	0.99	1	1	0	1	0	1	0
750	SVR	0.99	1	0.99	1	0.99	1	0.99	1	0.99	1	0.99	1	0.99	1
	GBR	0.93	6	0.97	3	0.95	5	0.93	7	0.96	4	0.94	6	0.94	6
	GPR	1	0	1	0	0.99	1	1	0	1	0	1	0	1	0
1000	SVR	1	0	1	0	1	0	0.99	1	1	0	1	0	1	0
	GBR	0.99	1	0.99	1	0.99	1	0.98	2	0.99	1	0.99	1	0.98	2
	GPR	1	0	1	0	1	0	1	0	1	0	1	0	1	0

fore, if one design exhibits a stress value beyond 250 MPa, it doesn't meet the stress targets and the value fitted by the algorithm is 1. On the contrary, if the stress value obtained for maximum rotational speed is under 250 MPa, the highest stress permitted for steel, the design is valid and the model learning takes the 0 value as input for this design. In order to decide the best machine learning algorithm for this classification problem, all three presented algorithms, SVR, GBR and GPR are tested successively using different size of data set samples for training: 250, 500, 750 and 1000. The performance metrics that describe the quality of the developed models are presented in Table 5.5.

Due to the fact that the identification of structures that can brake under high loads is a binary classification problem, besides the R^2 indicator, the accuracy and the confusion matrix [107] are analysed. The accuracy gives information about how many cases have been correctly predicted. The confusion matrix evaluates the accuracy of a classification using four categories: True Positive (TP), when the prediction is positive and correct, True Negative (TN), when the prediction is negative and correct and the combination of these two cases, False Negative (FN) and False Positive(FP). These indicators are detailed and discussed in Chapter 8.

Table 5.5 depicts R^2 and accuracy scores for different combination of algorithms and data size. It can be seen that GPR algorithm presents the highest values for both indicators compared with the other two ML algorithms. It can be seen that the R^2 score is low for 250 samples, even if the

Table 5.5: Prediction capability of the machine learning models for maximum rotor stress results.

Samples/ Models		Maximum stress values		
		SVR	GBR	GPR
250	$\mathbf{R^2}$	0.8	0.77	0.79
	Accuracy	0.93	0.92	0.93
500	$\mathbf{R^2}$	0.73	0.75	0.8
	Accuracy	0.95	0.96	0.95
750	$\mathbf{R^2}$	0.81	0.8	0.89
	Accuracy	0.94	0.93	0.97
1000	$\mathbf{R^2}$	0.92	0.84	0.93
	Accuracy	0.98	0.98	0.99

accuracy is high. This is due to the fact that the number of feasible designs (that resist at high inertial loads) is considerable bigger than the ones that are unfeasible (the iron bridge brakes). In the 250 samples dataset, there are 90% feasible designs and 10% unfeasible designs, for 500 samples, 89% feasible and 11% unfeasible. 90% feasible and 10% unfeasible cases appear in the 750 dataset, while for 1000 samples dataset, there are 89.6% feasible and 10.4% unfeasible designs. Therefore, the confusion matrix is useful in this case, where all the predictions can be evaluated.

The confusion matrix of the best classification model, GPR developed using 1000 samples is identified in Fig. 5.14. It can be seen that the model presents high performances, being able to identify 21 out of 23 unfeasible designs in the test set and all 177 feasible designs. From the total of 200 testing samples, the model misclassified only two designs. High values for R^2 and accuracy can be identified for this model in Table 5.5. It can be seen that the R^2 score has the highest value in this case and that it increased its value for every 250 samples added on top of the previous data-set. At the same time, the accuracy of this model is 0.99, higher than the results obtained with this algorithm for different number of sample points.

5.7.5 Vibration response values

For each analyzed design, the vibration response is determined using vibration synthesis for multiple speed values, in the form of run-up spectogram, as identified in Fig. 5.15. From each run-up spectogram, the first ten orders, marked in the figure, are extracted and used to train the machine learning model. Even if for the first order ($10\,f_{mech}$) no resonance occurs, the order is still included in the machine learning model to fully

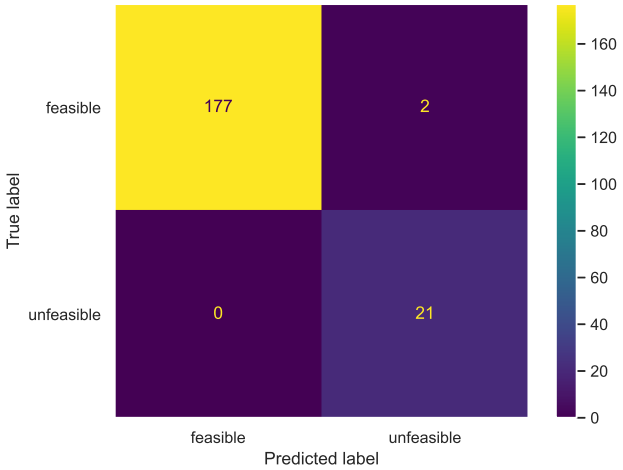

Figure 5.14: Confusion matrix of GPR 1000 classification model.

characterise the vibration behaviour of the motor.

The performance of the LSTM model to predict the vibration response is evaluated in the first phase by analysing the fitting capability given by the R^2 and MSE metrics. Afterwards, the models trained with different datasets are tested by comparing the results with the FEA ones in terms of vibration response highest peak amplitude errors and the speed at which the peak appears.

The test metrics scores are shown in Table 5.6 for each target. It can be seen that the model benefits from additional training data, the model increasing the R^2 values, but most important, decreasing the MSE. The highest mean MSE value is obtained for 250 samples, and the model with the best scores is the one with 1000 samples. For this model, trained with 1000 samples, the R^2 score is close to unity for almost every targets, the lowest value being for order 10, 0.8. Knowing that in this case there no resonance occurs, the result is acceptable. However, the MSE values are still non-negligible. Even if they are under 5% for most of the targets, high values appear for order 30 and order 90 (i.e., 36% and 25.3%). This is because the error is computed as an average value between the displacements errors for every speed value, and not the error for highest peak, where the resonance occurs and the displacement is the biggest. The model could still predict with high accuracy the resonance amplitude.

For a more detailed analysis, the errors in terms of highest peak amplitude and speed at which the resonance peaks appear are obtained by comparing the results in the model testing phase with the vibration synthesis method (based on FEA results). The influence of increasing the sample sizes is also taken into account for this analysis, starting with 250

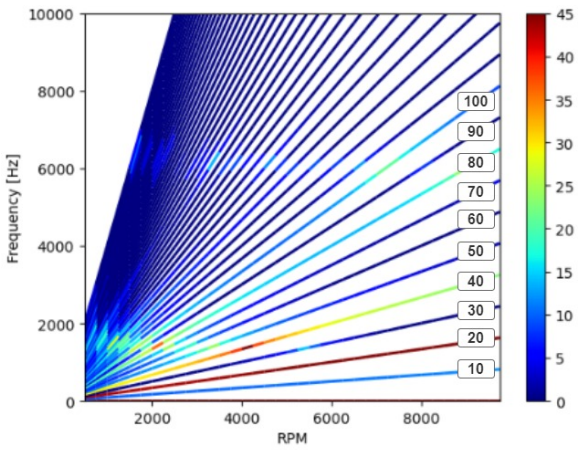

Figure 5.15: Run-up spectogram for one analysed design.

samples, then going to 500, 700 and ending with 1000 samples. The amplitude and speed errors are summarized in Table 5.7 for each order fitted by a machine learning model. As can be seen, for 250 samples, the model experience high amplitude errors of maximum 16% for order 10, but in this case, there is no resonance peak, followed by a highest peak amplitude error of 12.5 % for order 90. The model accuracy is improved for 500 samples, the error of order 90 being reduced to 3.6 %. The model succeeds to reduce the highest peak amplitude error under 5.2% for all mechanical orders. However, like in the previous case, the speed at which the highest peak appears differs in the developed machine learning model, compared with FEA based vibration synthesis. Speed error appear in the case of $20f_{mech}$, $30f_{mech}$ and $40f_{mech}$, the maximum error encounter being 5.55%, obtained in the last case.

The amplitude and speed errors are eliminated for LSTM networks developed with 750 and 1000 samples. For 750 samples, the amplitude error is reduced to under 4 % for all targets and to 11 % for order 30 the speed error is eliminated for order 20 and order 30, while the error for order 40 is still at the same rate. The LSTM network with 1000 samples doesn't present speed errors, meaning that the model succeeds to predict the speed at which the highest vibration occurs (caused by resonance phenomena) with high accuracy. At the same time, the amplitude errors are the lowest in this case, under 3.5 % in all cases, except for order 30, where the amplitude error is 6% (reduced from 11% in the 750 samples case). From the presented results, it can be concluded that the LSTM model developed with 1000 samples presents the highest capabilities to predict the vibration response, exhibiting the closest values to the FEA

Table 5.6: Prediction capability of the machine learning models for vibration response results.

	250		500		750		1000	
	R^2	MSE	R^2	MSE	R^2	MSE	R^2	MSE
Order 10	-	-	0.5	26.7	0.78	5.6	0.814	4.8
Order 20	0.98	20	0.98	6.1	0.979	24	0.998	1.7
Order 30	0.98	21.5	0.72	39	0.9	34	0.956	36
Order 40	0.995	10.5	0.998	3	0.995	8.2	0.999	4.7
Order 50	0.998	2.8	0.997	5.4	0.998	4.6	0.999	1.3
Order 60	0.994	17	0.99	26.5	0.996	12	0.999	2.1
Order 70	0.998	3.8	0.99	1.4	0.998	3.2	0.999	2.6
Order 80	0.99	19.34	0.998	3.85	0.995	7.6	0.998	2.1
Order 90	0.978	55	0.985	37	0.989	25.3	0.989	25.3
Order 100	0.98	35.5	0.993	12.1	0.994	13.1	0.998	3.5

ones. This can be observed also in Fig. 5.16, where the original values are displayed in comparison with the LSTM 1000 samples machine learning model results. The first ten order-cuts for different multiples of the base mechanical rotation frequency are presented for both situations, original and prediction.

5.8 Machine Learning Model Computational Cost. Machine Learning Model versus FEA

The final purpose of developing multi-attribute machine learning models is to integrate them in decision making process in the design stages, for system level analysis and in optimization routines to obtain the best version of a product. The motor performances must be obtained with increased accuracy, in a reduced time. In this section, the best version of the multi-attribute machine learning models are integrated into one optimisation loop in order to characterise their behaviour and quantify the computational cost saving. The best performance machine learning models for each physics analysed that give the prediction of the multi-attribute performances are GPR 1000 for electromagnetic targets, GPR 250 for natural frequencies of modes and GPR 1000 for losses, and from now on denoted with ML1000.

The benefit of using the ML1000 machine learning model over FEA is quantified by conducting an optimization process of the stator geometry that aims to maximise the objective function consisting in the natural frequency of one stator mode-shape with respect to multi-attribute constraints. In parallel, a FE based optimisation process, having the same

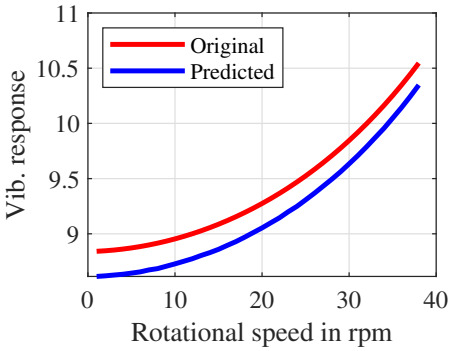

(a) $f = 10 f_{mech}$

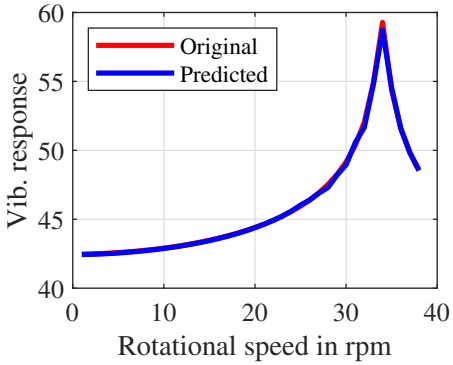

(b) $f = 20 f_{mech}$

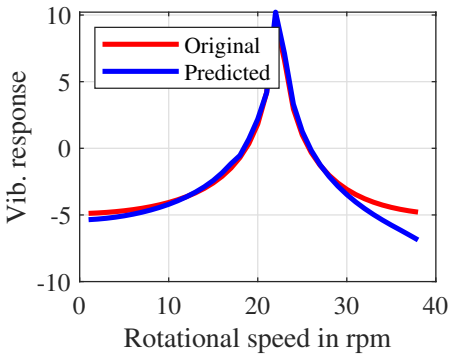

(c) $f = 30 f_{mech}$

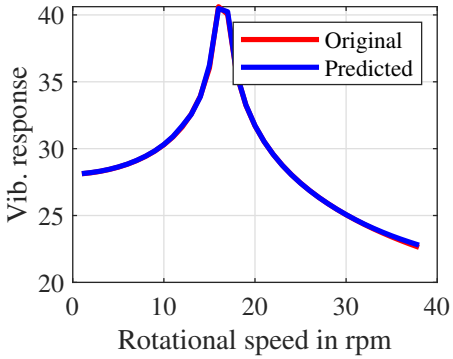

(d) $f = 40 f_{mech}$

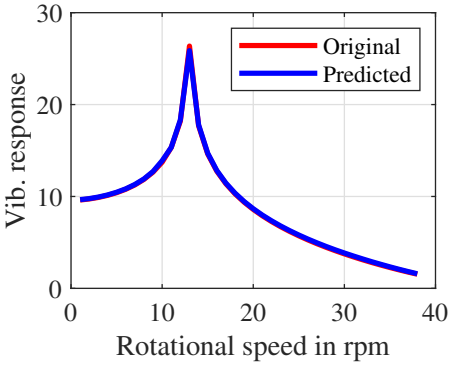

(e) $f = 50 f_{mech}$

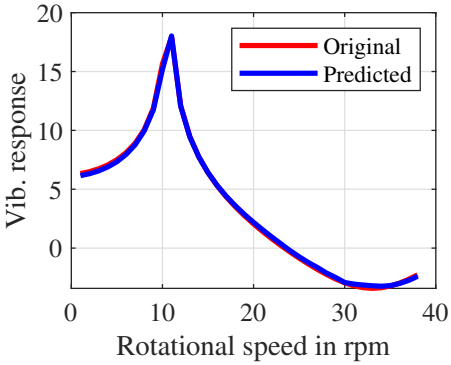

(f) $f = 60 f_{mech}$

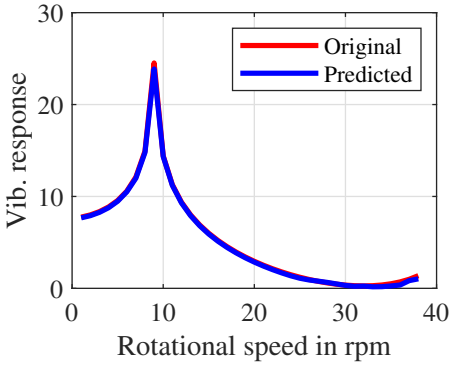

(g) $f = 70 f_{mech}$

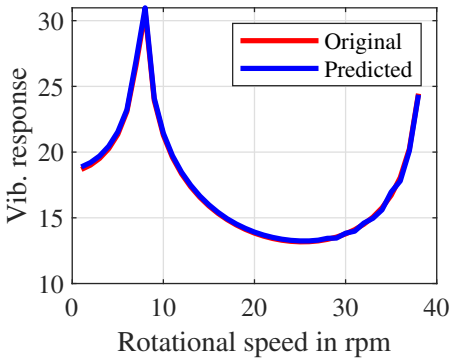

(h) $f = 80 f_{mech}$

Table 5.7: LSTM network prediction capability to predict vibration displacement for different multiples of the base mechanical rotation frequency (orders). Resonance peak amplitude and speed mean relative error evaluation.

	250		**500**		**750**		**1000**	
	A [%]	ω[%]	A [%]	ω[%]	A [%]	ω[%]	A [%]	ω[%]
Order 10	16	0	5.2	0	2.24	0	1.9196	0
Order 20	2.16	2.77	1.64	2.77	0.67	0	0.9361	0
Order 30	9.2	4.16	16	4.16	11	0	6	0
Order 40	2.9	5.55	2.5	5.55	1.24	5.5	0.332	0
Order 50	4.4	0	3.2	0	3.6	0	1.92	0
Order 60	7.5	0	5.2	0	3.1	0	0.52	0
Order 70	2.5	0	4.4	0	3.96	0	2.74	0
Order 80	4.1	0	3.62	0	3.28	0	0.98	0
Order 90	12.5	0	3.6	0	3.44	0	3.5	0
Order 100	2.43	0	2.05	0	1.82	0	1.7	0

goal and characteristics, is performed on the parametric 2D and 3D FE parameterised motor models. For a fair comparison, both accuracy and computational costs of the two methods are analysed and discussed.

5.8.1 Optimisation Process

For the optimisation routine, the HEEDS MDO software package is used. HEEDS MDO was chosen due to its capability to drastically reduce the process time, compared with other optimization software [108], by looking for the perfect and most reliable solution in a specific design space.

The optimisation algorithm was chosen based on the problem application. As HEEDS software is employed for optimisation problem, a dedicated and specific optimization algorithm called SHERPA (simultaneous hybrid exploration that is robust, progressive and adaptive) [108] is exploited. The top benefits of SHERPA are: a fast and simple utilization, even for non-experts; presents multiples approaches used at the same time, and not progressively; a fast and auto adaptation to a particular problem, without needing user action; capacity to identify the global and the local optimum simultaneously; conducts optimisation by evaluating the actual model, rather than using approximate response surface models; high efficiency, saving days or even weeks of CPU time [108].

Due to the fact that the motor has a ten pole twelve slots configuration, the radial electromagnetic forces act on the stator and mainly ex-

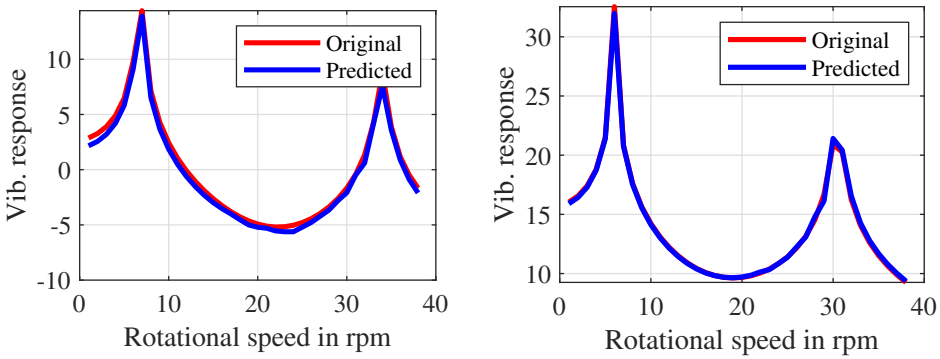

(i) $f = 10 f_{mech}$ (j) $f = 20 f_{mech}$

Figure 5.16: ML LSTM capabilies to fit the machine vibration displacement order-cuts for different multiples of the base mechanical rotation frequency for original and the optimised structures.

cite mode 2, causing deformation. In this context, the optimisation problem is characterised as follows: maximise the function f([x]), consisting of the eigenfrequency of global mode 2, subject to a set of constraints, $C_{min} \leq C([x]) \leq C_{max}$, with $[x]$ denoting the stator geometry parameters vector defined by upper and lower limits vectors [UB], [LB], defined in Table 2.2 from Chapter 2. The C_{min} and C_{max} parameters are the constraints minimum and maximum values.

$$\text{maximise f}([\text{x}]), \text{subject to} \begin{cases} [LB] \leq [x] \leq [UB] \\ C_{min} \leq \text{C}([\text{x}]) \leq C_{max} \end{cases} \tag{5.3}$$

The constraint vector $C([x])$ is defined by restrictions applied on the natural frequency of Mode 2, average torque, torque ripple and total losses. The natural frequency of Mode 2 is shifted with a maximum of 10 % from the Mode 2 natural frequency baseline motor design. In addition to that, the average torque must be higher than the baseline design one, while the total losses and torque ripple are kept under the values obtained for the baseline design.

5.8.2 Machine Learning vs. FEA

In this context, the feasibility and the fidelity of the resulting ML 1000 model is studied by conducting the optimisation for a series of cross section valid designs defined by a range of 250 to 2000, with a step of 250 designs. The results are compared with the FEA based optimisations, taken as reference. The optimisation values derived from the two parallel processes for the case of 500, 1000 and 1500 optimisation designs

are compared in Table 5.8. The presented results, representing the cross-section geometrical parameters corresponding to the optimal design, together with the corresponding Mode 2 natural frequency, average torque, torque ripple and total losses are expressed as the percentage difference from the nominal (reference) motor values. By analysing the results, it can be concluded that the ML1000 based optimisation routine presents high fidelity results, compared with the FEA based optimisation process, for all investigated situations. A negligible difference between the two methods, but this is insignificant due to the limitation of the manufacturing process, as the error appears for the third decimal.

Table 5.8: Optimisation results comparison between ML1000 and FEA.

	500		**1000**		**1500**	
	FEA	**ML1000**	**FEA**	**ML1000**	**FEA**	**ML1000**
JT[%]	8.8	9.1	8.5	8.5	8.56	8.61
SO [%]	97	99	76	78	78	79
SOAng [%]	11.6	11.5	13.98	13.45	13.81	13.45
TGD [%]	8	8.2	8.9	7.2	16	20
TWS [%]	-1.4	-1.47	-2.9	-2	-1.6	-1.7
Mode2 Freq [%]	9.82	9.94	9.7	9.8	9.78	9.97
T_avg [%]	2.35	2.22	2.35	2.35	2.35	2.38
T_rip [%]	-42.6	-30	-43.7	-42.7	-43.2	-42.5
Tot Losses [%]	-0.03	-0.03	-0.03	-0.03	-0.03	-0.03

The computational cost of ML1000 and FEA based optimisations, is depicted in Figure 5.17. Here, the computation time is expressed in function of the number of machine geometric designs generated during the optimisation task (N_O).

The computing cost expressed in seconds for the FEA based optimisation is identified with blue line and with red for the ML1000 model based routine. In order to have a comprehensive analysis, the expression of time for the machine learning model includes both machine learning model developing time and the optimisation time. As it was expected, the most time consuming process of the machine learning model, is the data extraction task, necessary for model identification. Taking into account that the structural and electromagnetic FE analysis are executed simultaneously, the total cost of developing the ML1000 model using data extracted from FEA simulations, reaches 60 h. However, once the simulations are ended and the information is extracted the next steps are fast. The training time is insignificant (i.e., few seconds for 1000 samples), and the model runs instantly. By analysing more in depth the displayed figure, one can identify when the surrogate model becomes feasible over the FEA

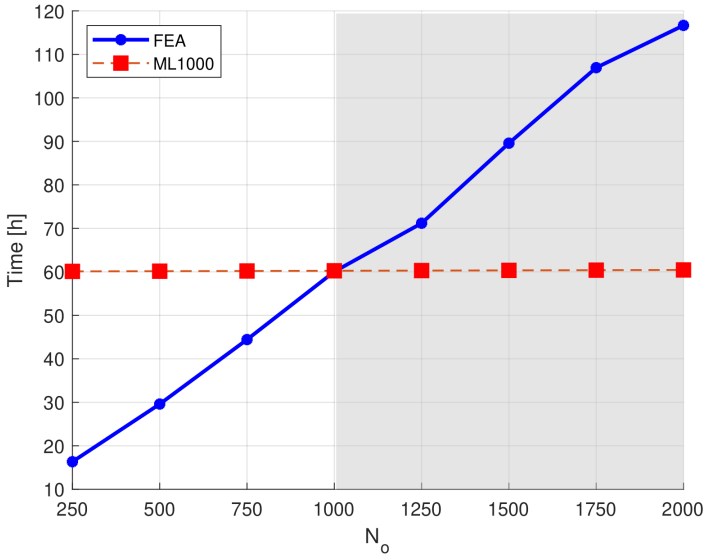

Figure 5.17: Machine learning model vs. FEA computational time.

method. The ML1000 model computational cost is higher than the FEA if the number of simulation needed to get the data to learn the surrogate model are over the number of optimisation runs. From 1000 optimisation runs above, the ML1000 model becomes superior and consumes less computational resources and time than the FEA method. In Figure 5.17, the interval where surrogate model is more efficient than FEA is shaded with gray. Above this limit, the FEA computational cost grows significantly for each new design. In comparison, the computational cost of a new design for the machine learning model approach is insignificant.

The reduction of the computational time introduced by the surrogate model can be quantified by the introduction of the time efficiency factor that gives the relative saving in computational burden [109]. The computational efficiency factor (k_{cr}) is characterized by the simulation design number necessary to train the machine learning model (N_D) divided by the number of designs analysed in the optimisation process (N_O):

$$k_{cr} = \frac{N_D}{N_O} \tag{5.4}$$

The advantage introduce by the machine learning model in the computational time is underlined in Fig. 5.18 and marked with red. The surrogate model is more time efficient that the FEA when k_{cr} is smaller or equal than 1. This situation is marked with grey area in the same figure. The surogate model is more feasible for several case situations. For the extreme case presented in the figure, a computational time reduction of

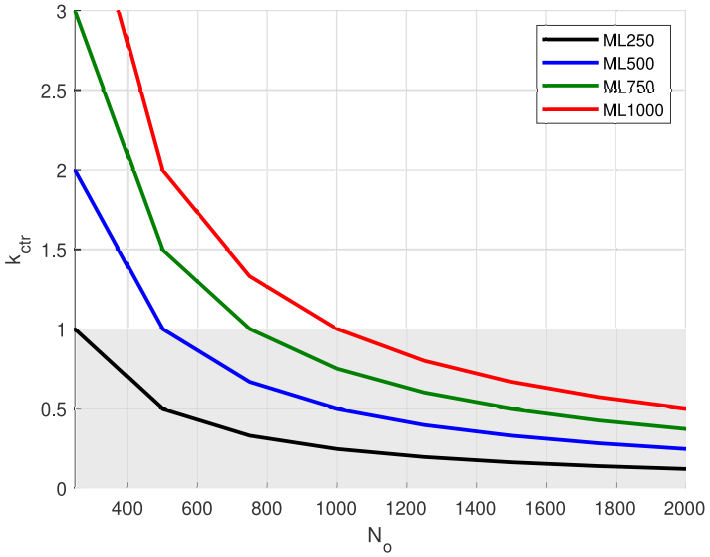

Figure 5.18: Computational efficiency factor.

50% is obtained if 2000 evaluations are performed during the optimisation process. Moreover, different values of the computational efficiency factor obtained for different machine learning models, that rely on 250, 500 and 750 samples are shown with black, blue and green curves. It can be observed that these cases begin save computational time starting with less optimisation evaluations, but they not present the same results accuracy like ML1000 model.

5.9 Intermediate Conclusions

In this chapter, a method that helps in the decision making process during the design stage of an electrical motor and ease the optimisation process to allow a faster time-to-market has been described and validated. The method allows to bring all the machine targets coming from different physics, electromagnetic, thermal, structural earlier in the design cycle, where they can be optimised together and the designer can know if a design meets imposed targets or not. By using the proposed solution, it was shown that the cross-section design can be completely characterized in the early stage design, without being necessary to perform other studies in the late stage design or even in prototyping phase to know the motor characteristics, reducing both costs and time-to-market.

The proposed solution consisted in developing machine learning models that predict the motor performances, such as torque, back emf,

losses, stator natural frequencies, maximum stress experienced by rotor, vibration characteristics from input geometrical parameters, in the early stage design. The multi-attribute model was constructed based on the data achieved by conducting a series of 2D electromagnetic and 3D structural FE analysis on a set of motor models generated by modifying the DOFs consisting in the geometrical parameters of a base parametric motor model. Geometric parametric models were employed to evaluate the multi-physical performances of an electrical machine and generate training data.

The machine learning algorithms used to build the models were support vector regression (SVR), gradient boosting regressor (GBR) and Gaussian process regressor (GPR), for electromagnetic, structural, motor losses and stress targets, and Long Short Term Memory (LSTM) network for NVH targets. The first three algorithms were selected due to their capacity to predict discrete datasets and the LSTM network was chosen due to its increased ability to predict time-dependent sequence data. Moreover, their accuracy was tested for four training datasets, 250, 500, 750 and 1000 samples. The regression models fitting capabilities were individually analysed. Two types of key performance indicator (KPI) are used to measure the fitting capabilities: the coefficient of determination (R_2) and the mean squared error (MSE). Besides that, for the stress classification problem, the classification accuracy and the confusion matrix were employed to test the fidelity of the predictions. The obtained scores showed that GPR algorithm applied on 1000 samples is the most suitable machine learning model to predict the electromagnetic torque and back electromotive force harmonics orders, its R^2 scores being higher than 0.95, while the MSE was less than 5%. For structural targets, the regressor that is able to fit the data with the best scores is the GPR model with 250 samples, R^2 score being 1 and MSE 0%. Regarding the ability of the machine learning models to predict the motor losses, the GPR 1000 samples machine learning model presents the best results, with R^2 scores of 1 and MSE values of 9%. The stress classification model showed the highest accuracy for GPR 1000 samples machine learning model, when the R^2 score was 0.93 and the accuracy was 0.99. More important is that the confusion matrix showed that the model presents high performances, being able to identify 21 out of 23 unfeasible designs in the test set and all 177 feasible designs. From the total of 200 testing samples, the model misclassified only two designs.

The vibration characteristics were successfully predicted using Long Short Term Memory (LSTM) networks. The first ten mechanical orders extracted from the run-up spectogram were predicted from design parameters with high accuracy for a LSTM network model developed with

1000 design samples. The test metrics scores showed that the R^2 score is close to unity for almost every targets, the lowest value being obtained for order 10, 0.8. The MSE results were under 5% for most of the targets with a maximum of 36 % for order 30. However, the most important is the error that appears at the maximum peak, where the resonance occurs. Therefore, the models trained with different datasets were tested by comparing the results with the FEA ones in terms of vibration response highest peak amplitude errors and the speed at which the peak appears. The best results are obtained for 1000 samples, where the speed errors are eliminated and the amplitude errors are the lowest, under 3.5 % in all cases, except for order 30, where the amplitude error is 6% (reduced from 11% in the 750 samples case). The presented results led to the conclusion that the LSTM model developed with 1000 samples presents the highest capabilities to predict the vibration response, exhibiting the closest values to the FEA ones, being able to predict the speed at which the highest vibration occurs (caused by resonance phenomena) with high accuracy as well.

The multi-attribute machine learning model developed was integrated into optimisation routine to enable the design process. The best combination of the most suitable machine learning models for each physics analysed was denoted with ML1000. The benefit of using the ML1000 machine learning model over FEA was quantified by conducting an optimization process of the stator geometry that aimed to maximise the objective function consisting in the natural frequency of one stator mode-shape with respect to multi-attribute constraints. In parallel, a FE based optimisation process, having the same goal and characteristics, was performed on the parametric 2D and 3D FE parameterised motor models. For a fair comparison, both accuracy and computational costs of the two methods were analysed and discussed.

It was shown that the multi-attribute machine learning model developed by combining the best models for each physics involved can provide accurate and significant reduction in computational time, compared with the classical FEA approach. By analysing the results, it was concluded that the ML1000 based optimisation routine presents high fidelity results, compared with the FEA based optimisation process, for all investigated situations. A negligible difference between the two methods appeared, but this is insignificant due to the limitation of the manufacturing process, as the error appears for the third decimal.

Analysing the time costs, the studies showed that the ML1000's computational cost is higher than the FEA one if the number of simulation needed to extract the training data are over the number of optimisation runs. From 1000 optimisation runs above, the ML1000 model becomes

superior and consumes less computational resources and time than the FEA method. Above this limit, the FEA computational cost grows significantly for each new design. In comparison, the computational cost of a new design for the machine learning model approach is insignificant.

6. Asymmetric stator slot opening geometry for PMSM NVH optimisation

The process of designing an electrical motor relies on optimisation. Most of the times, due to economical reasons, especially given by increased costs of rare-earth materials, the electrical motors are optimised to met the lowest production costs [110]. In the last few years, the ability to perform optimisation with thousands of designs has become more accessible. This is mainly due to the innovations in Mathematics and Computer Sciences that increased the computational power and data storage of working stations [111]. Therefore, by increasing the capabilities of computers, more complex tasks can be completed. Multi-objective optimisation, including besides the traditional electromagnetic targets, thermal, structural, NVH attributes are considered for a robust design.

As described in Chapter 5, the process of designing an electrical machine that relies on optimisation consists in a successive number of steps that deals with one physics. The electromagnetic characteristics are fulfilled first, but the same design has to met the structural targets and allow a proper thermal behaviour. The last characteristics that are satisfied in this waterfall process are the NVH characteristics. This means that for an optimised design that meets the electromagnetic, structural and thermal goals, there are limited possibilities to improve the NVH attributes without affecting the electromagnetic ones [112]. Based on the position of the NVH attributes optimisation process in the design journey of an electrical motor, this describes the late-design stage. The other type is the early stage design, thoroughly discussed in the previous chapter, and it is more affected by uncertainty, as the NVH transfer path is still not fully characterised (e.g., the information about the housing is not available yet).

One of the main challenges in the automotive industry that shifts its focus to electromobility is the electric noise, vibration and harshness (NVH) that need to meet quality standards. Even if the electrical motors are less noisy compared with combustion engines, the user perceives the sound as tonal and uncomfortable. For a PMSM, the mechanical and aerodynamic sources of noise and vibration can be easily diminished, but reducing the contribution coming from electromagnetic causes is more demanding, as it is more related to the machine operation and will inevitably impact the machine performances at the same time. The air-gap electromagnetic forces created by a fluctuating magnetic field, together with the torque ripples are the main causes of noise and structure vibrations in an electrical machine. In particular, the radial forces are the ones that excite the stator structure, cause the stator core to deform and determine air -

borne noise. A diminished affect is coming from the tangential component of air-gap forces that cause stator teeth bending modes. The NVH characteristics are traditionally reduced in the design phase by choosing a combination of slots-pole numbers that presents reduced torque ripples or by introducing skewing of stator or rotor cores. However, even if the torque ripples are reduced, both continuous and step skewing increase the manufacturing complexity and reduces the machine performances, such as the average torque and back-EMF [113].

In the late-stage design, however, the force density harmonics that act on the stator tooth tip and cause vibrations, can be minimised by introducing irregularities in the motor cross-section and modifying the air-gap permeance. The air-gap force spectra is changed by optimizing the machine cross-section, resulting in diminished NVH levels [114]. This procedure is thoroughly investigated in literature. In [115], elliptical notches introduced on top of saliency shape the rotor cross-section of a permanent magnet assisted synchronous reluctance machine (PMASyn RM). The designs are optimised to reduce the most dominant force harmonics, the results showing improvements in the final vibration response. The impact of elliptical notches introduced in the rotor shape on the stator noise caused by the most important force harmonics is studied in [116], considering the effects on core losses and electromagnetic torque in order to avoid a significant reduction of performances. The same approach is discussed also in [118], while the magnet shaping technique is presented in [117]. By shaping the magnet surfaces with different harmonic functions, sine harmonic compensation (SHC), inverse cosine harmonic compensation (ICHC), and tangent harmonic compensation (THC), it is intended to improve the vibration levels and torque ripples, while monitoring the average torque characteristics.

Recent studies focus on the impact of motor geometry, especially the stator slots geometry, on the machine performances. For PMSM, two types of asymmetry can be introduced: skewing or geometry modification. The first one improves the cogging torque attributes but diminishes the motor performances, but the second one can improve the torque characteristics if local saturation is considered. If focusing on the latter, the stator slot opening geometry can be modified by introducing asymmetry. This results into an asymmetric stator structure and could be beneficial to both electromagnetic and NVH characteristics. A PMSM with asymmetric stator geometry is investigated in [119], where the tooth-tip is modified, while its saturation levels are monitored. The results are focused on electromagnetic values and the machine performances in function of the direction of rotation. Other studies that focus on the impact of asymmetries on electromagnetic attributes are presented in [120] and [121].

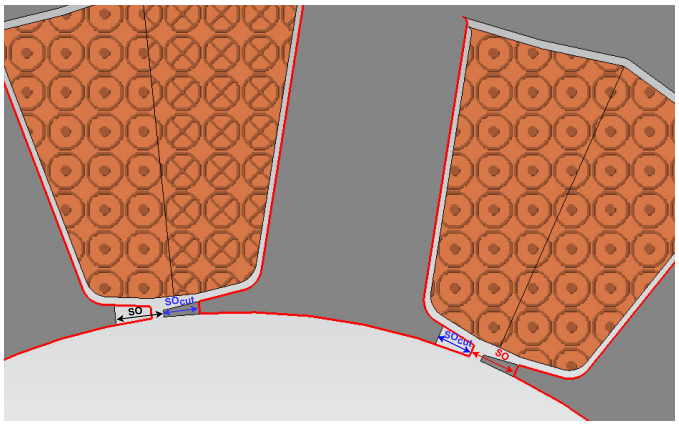

Figure 6.1: Stator slot opening modification introduced in the optimisation routine, where the original structure is represented with red lines.

They focus on adjusting the teeth widths with the objective to reduce local saturation. It is shown that by increasing the width of teeth that are saturated, the torque ripples are diminished with up to 33 % compared with the symmetrical design.

In industry, a motor with asymmetrical geometry is used for traction on the General Motors' Chevrolet Bolt Gen2 (2^{nd} generation) vehicle. For this motor, the size and placement of stator slot openings under each pole are modulated and individually modified to optimise the torque ripple and radial force [122]. In this case, the stator core made of soft magnetic material, is cut in an optimisation process. The analysis show beneficial changes in the torque ripple and radial force harmonic spectrum.

However, none of the above studies focused on the NVH characteristics improvement, but payed attention only to the electromagnetic side. In this chapter, an investigation of the impact of stator slot opening asymmetry on the NVH characteristics of the machine under study is performed. The slot cross section geometry is introduced in an optimisation loop in order to reduce the stator vibration levels, while keeping the electromagnetic average torque under observation so that the machine characteristics are not highly affected. The asymmetry is introduced in the conventionally symmetrical slot opening geometry by cutting one side of the stator tooth tip with the value SO_{cut}, while on the other side of the tooth, the tooth tip experience additional soft magnetic material in order to keep the original slot opening width (SO) constant, as presented in Fig. 6.1.

This chapter starts with the multi-physical workflow employed to extract the vibration response of the motor. The optimisation process that allows to change the stator cross-section together with the optimisation

NVH costs are then discussed, leaving the final section for interpreting the results and quantifying the NVH improvements.

6.1 PMSM Multi-Physical Analysis

The stator vibration response is obtained using the multi-physical analysis workflow presented in Section 2.5.2. The workflow relies on the vibration synthesis method [28] that couples the 2D electromagnetic analysis with the 3D structural evaluation. For that the FEA models developed for the machine under study and presented in Section 2.6 are used. For the electromagnetic analysis, the model is analysed within Simcenter Magnet software that allows introduction of asymmetry through parameterised values. The electromagnetic analysis is performed at steady state conditions, for a constant rotating speed of 1800 rpm and i_{d}=0 A and i_{q}=10 A.

The unitary forced response is obtained using the structural 3D FE stator model developed in Simcenter 3D, identified in Section 5.4.2, Fig. 5.4. Six pairs of $sin-cos$ force shapes (from 2 to 12 with a step of 2), together with the DC component, both radial and tangential directions, are applied on the stator structure to catch the effects of most important spacial force harmonics. An asymmetrical stator structure with the force shape $F_{rad[I],cos2}$ acting on the 3D stator tooth tip model is identified in Fig. 6.2.

Ultimately, the final vibration response, $v_{[I]}(f)$, is given by the superposition of all frequency vibration responses $v_{[I],m}(f)$, obtained for each individual unitary force shape (m), scaled with the corresponding sin-cos frequency domain amplitude factors.

6.2 Electrical Machine NVH Optimisation

The NVH characteristics of various machine designs having cross-sections with different degrees of asymmetry are assessed during an optimisation process.

6.2.1 Asymmetric Stator Slot Opening

For this process, the air-gap forces harmonic content is modified by adjusting the stator tooth tip geometry. Figure 6.1 presents the the original slot geometry marked with a red profile solid and the modified asymmetric design with gray surface. In the same figure, the quantity that is removed from one side of tooth tip and inserted on the symmetrical side is marked with blue and introduced by SO_{cut} parameter. Therefore, the

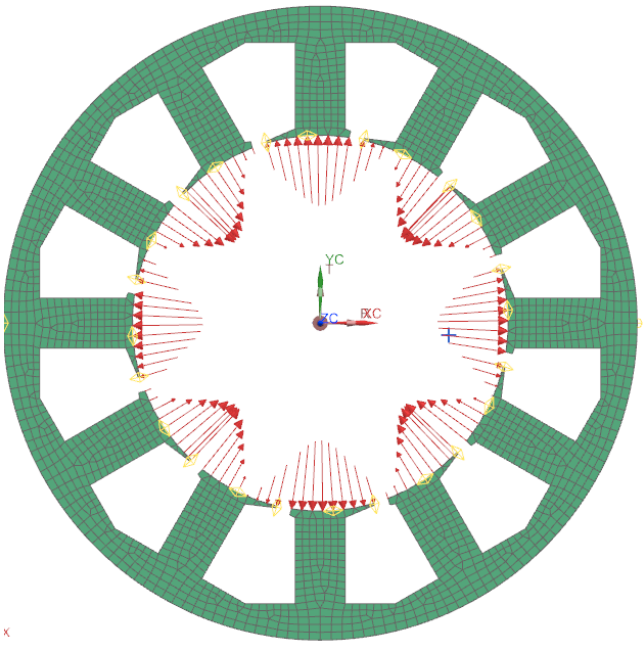

Figure 6.2: Asymmetric 3D stator model and he force shape $F_{rad[I],cos3}$ acting on the stator tooth tips.

stator width corresponding to the symmetrical slot geometry, SO, keeps its value unchanged during the optimisation procedure.

In order to be suitable for optimisation loop, the electromagnetic model is parameterised, allowing for introduction of the SO_{cut} parameter. This parameter is used as DOF in the optimisation routine. For this parameter, an upper and lower limit of its variation interval is assigned considering that the generated designs must be feasible.

6.2.2 Optimisation Problem

In order to perform the optimization routine, the parametric electromagnetic model is coupled to the optimisation algorithm. This connection is assured by an optimisation software, Simcenter HEEDS MDO. Using this tool, the exploration of the design space and the optimization routine is employed using a specific algorithm to solve the problem, SHERPA (simultaneous hybrid exploration that is robust, progressive and adaptive) [108]

The optimisation problem is defined mathematically through an optimisation function: minimise the function f([x]) that represents the vibration response of the motor. The function is dependent on SO_{cut}. The variation interval of the variable SO_{cut} is from 0 [mm] (symmetrical case) to 2.5 [mm] (maximum level of introduced asymmetry). On top of that, a

set of constraints, $C_{min} \leq C([x]) \leq C_{max}$, impose some limits in the searching space. The constraints are referring to the machine's performances (i.e., average value of electromagnetic torque and torque ripples). Therefore, in order to limit a high decrease of machine's performances, the average torque, $[x]$, is allowed to vary between defined upper and lower boundaries, 0 and 23%.

$$\text{minimise f}([\text{x}]), \text{ subject to } \begin{cases} [LB] \leq [x] \leq [UB] \\ C_{min} \leq \text{C}([\text{x}]) \leq C_{max} \end{cases} \tag{6.1}$$

6.2.3 Results

The results obtained during the optimisation procedure are presented. For that, the optimistation results are displayed together with the original design behaviour. Figure 6.3 presents the order cuts for multiples of the base mechanical frequencies of the original design (with blue lines) and three optimised structures selected based on their impact on the electromagnetic torque. The reduction of electromagnetic torque was limited to 8%, 15% and 23%.

By analysing the results presented in Fig. 6.3, it can be observed that the vibration response modifies for different degrees of introduced asymmetry. A significant increase in the vibration response can be identified when stator slot opening asymmetries of $\text{SO}_{\text{cut}} = 1.2$ mm and $\text{SO}_{\text{cut}} = 1.76$ mm are introduced. It is notable that all order cuts present an increase of the displacement response. The first order-cut ($f = 10 f_{mech}$) presents an increase of the vibration response with 1.5 % for $\text{SO}_{\text{cut}} = 1.2$ mm asymmetry case. A more substantial increasing rate is obtained for $\text{SO}_{\text{cut}} = 1.76$ mm, 16.1 %, whereas for the first case, with $\text{SO}_{\text{cut}} = 0.71$ mm, the vibration response is enlarged with 0.2 %.

The same applies for other order-cuts. For example, by analysing the third order-cut, an increase of 0.3 % is identified for the first case of asymmetry. Again, a more substantial increase is acquired for the second asymmetry case, 3.1 % and for the third case of geometrical shaping, 21 %. Similar results are obtained for the eighth order-cut, the vibration response is enlarged with 1.2 % in the $\text{SO}_{\text{cut}} = 1.2$ mm case and with 9.6 % for the last example, $\text{SO}_{\text{cut}} = 1.76$ mm.

On top of Increasing the NVH levels, the electromagnetic torque is also affected. The change in torque expressed in percents can be identified in Fig. 6.4. For the first asymmetric case, $\text{SO}_{\text{cut}} = 0.71$ mm, the electromagnetic torque is reduced, compared with the symmetrical design, with 8 %. The average torque is decreased with 15 % for the second asymmetric example, whereas for the third one, the average torque

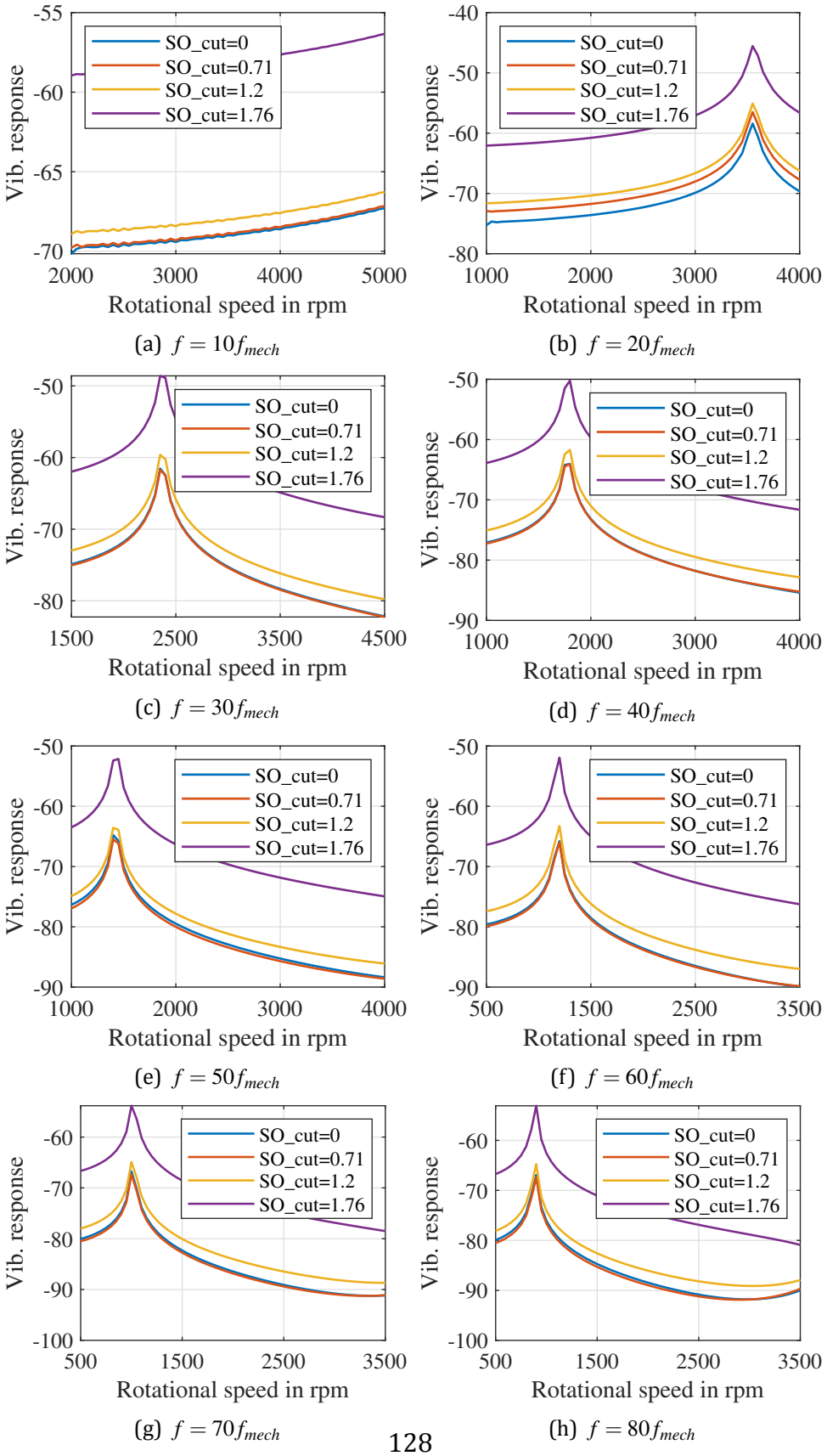

Figure 6.3: Machine vibration displacement (scaled) order-cuts for different multiples of the base mechanical rotation frequency for original and the optimised structures.

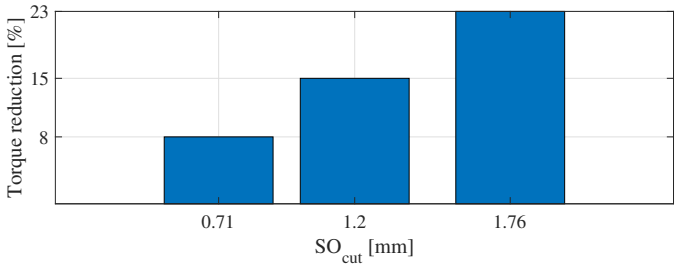

Figure 6.4: Torque reduction [%] obtained for asymmetric optimised structures.

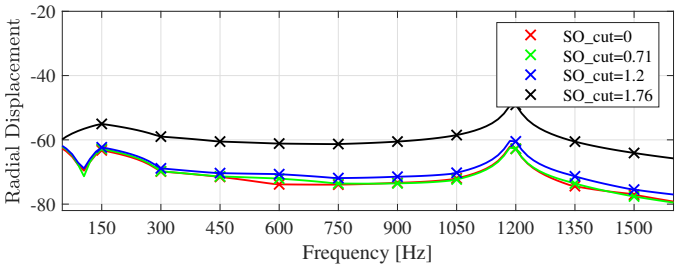

Figure 6.5: Radial displacement ($10Log_{10}$ scale) for the original design (red) and optimised designs at 1800 [rpm].

is reduced with 23 %. These values are higher than the torque reduction values obtained with other methods of cross-section modification for vibration response reduction available [115], [116].

For the steady-state conditions, at a rotational speed set at 1800 rpm, the vibration values are identified in Fig. 6.5. Here, the original design results are compared with the optimisation ones. Based on the different degree of asymmetry introduced, the radial displacement values varies. To quantify the reduction of the vibration response for different frequencies peaks, the relative change between the optimised designs and the original one is computed. The resulting changes expressed in percents are presented, for 1800 rpm, in Fig. 6.6. An increase of the vibration levels with 2 % is obtained for the first optimisation design defined by $SO_{cut} = 0.71$ [mm], at 600 Hz. A more significant enlarging in the vibration response is derived for the second asymmetry case, represented with blue line in Fig. 6.5, where a vibration amplification with up to 4 % is obtained. The most significant vibration response amplification is obtained for the third optimised structure defined by $SO_{cut} = 1.76$ mm, where the values are increased with 17 %.

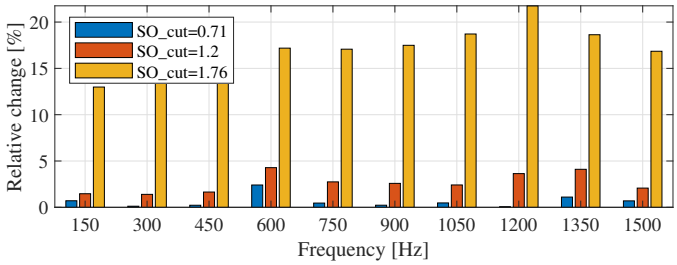

Figure 6.6: Relative change expressed in percents between the original design frequency peaks and the optimised ones at 1800 [rpm].

6.3 Intermediate Conclusions

A method to improve the NVH characteristics of the electrical machine under study in the late stage design was thoroughly studied. By showing a comparison between radial displacements obtained for original motor design and three other optimisation results, it was demonstrated that the proposed method increases the noise and vibration levels. For that, the original design was modified during the optimisation process by introduction of different degrees of asymmetries in the stator slot opening geometry.

The asymmetry was introduced in the conventionally symmetrical slot opening geometry by cutting one side of the stator tooth tip with the value SO_{cut}, while on the other side of the tooth, the tooth tip experienced additional soft magnetic material in order to keep the original slot opening width (SO) constant. The optimisation workflow focused on the NVH attributes, while keeping the electromagnetic average torque under observation so that the machine characteristics are not highly affected. On top of that, constraints conditions were imposed related to the maximum value of torque ripple.

The multi-physical workflow employed to extract the vibration response of the motor relies on the vibration synthesis method, where the unitary force-shapes responses were scaled with force factors in order to obtain the final vibration response. The stator corss-section geometry, focusing on stator tooth-tip geometry, was changed with the objective to decrease the radial displacement amplitudes. The optimisation results showed that the vibration response is increased if constant asymmetry is introduced. Three asymmetry cases were selected and discussed. The asymmetry cases were selected based on the impact of geometric changes on the average torque values. The imposed torque tresholds were 8 %, 15 % and 23 %. By comparing the symmetrical and asymmetrical cases, it was shown that the vibration response was increased for all three cases.

Focusing on the full RPM-frequency range vibration response of multiples of the base mechanical frequency, the first order-cut ($f = 10 f_{mech}$) was increased with 1.5 % for $\mathrm{SO_{cut}} = 1.2$ mm asymmetry case and for the third case, defined by $\mathrm{SO_{cut}} = 1.76$ mm , the radial displacement was amplified with 16.1 %, compared with original symmetric design. The same pattern applies if the motor is analysed at constant speed. For a rotational speed of 1800 rpm, the vibration response was increased with up to 23 % for the third asymmetric case.

7. Condition Monitoring of an Industrial Elevator

The electrical motor under study was analyzed intensively thorough the previous chapters for automotive applications. In this chapter, a PMSM with a different architecture is integrated within an industrial system in order to drive the system and assure the movement of the mobile parts. Therefore, the PMSM is integrated within an industrial application and analyzed at system level.

The application considered in this chapter is an industrial electromechanical elevator. Because the elevator is a complex system that operates constantly, it requires periodic maintenance. Studies show that more than 12 million lifts work daily and their number is rapidly increasing. These systems must always operate in safe conditions and dedicated safety devices need to be included and a frequent maintenance must be scheduled in order to take care of this aspects. However, a daily maintenance of these systems means an effort of half a million hours of human labor, considering a failure rate of over 164,000 times per day [124].

A more efficient way of scheduling the elevator maintenance is by monitoring the states conditions and decide whether the system operates under normal, warning or faulty conditions, and if it is necessary or not to stop the operation and intervene. This concept is called condition monitoring and helps in the early detection of faults by giving continuous information about the system conditions. Once the system actual state is known, if a fault is identified in its incipient phase, the system can be rapidly disconnected without risking the safe and integrity of passengers [125]. Besides this, the maintenance costs also benefits from condition monitoring and predictive maintenance by lowering the operational costs, as the corrective maintenance is performed only if necessary and by increasing the components life expectancy [126].

Predictive maintenance evolved together with the new development of Internet of Things (IoT), artificial intelligence, machine learning, predictive analytics and increase in the computational power. The core of this method is the AI or machine learning model trained with prerecorded data that provides the real state of the system and identifies a potential fault based on the data collected from system's sensors [127].

Extending the application of predictive maintenance in different technology domains opens new opportunities for improvement: immersive technologies (e.g., VR) can be used for visual appreciation of the system state, IoT will allow remote inspection, making the technology more affordable and accessible. The ongoing evolution of this technology is illustrated in studies from both academia and industry. The traditional

approaches for fault diagnosis in electrical machines are based on non-invasive signal processing by analyzing the stray flux or using the Park's vector approach [128]. IoT applied for remote monitoring of vibration and acoustic characteristics of elevators using remote data acquisition from sensors, identifies trends and reports when a fault is possible is presented in [129]. Moreover, in [124] the remote condition monitoring of the elevator is described, together with the challenges of developing a wireless intelligent multi-sensor module used to monitor the cabin position. The occurrence of faults caused by the passengers is considered by an intelligent monitoring system composed by high-definition camera and smoke alarm in [130] in order to assure a safety operation.

The present-day evolved methods that make use of AI and IoT rely on the digital twin of the system under test. The digital twin generates the data needed for machine learning under different operation conditions imposed by the user without risking the system integrity. This way, faulty conditions can be observed through simulations scenarios. The testing results come into the picture to support the virtual representation, when the validation and refinement processes are performed [131], [132].

This chapter starts by giving an overview about the architecture of the elevator under test and its corresponding dynamic model developed within Simcenter Amesim. The developed virtual model is described and the validation process using experimental data is performed in order to have a high accuracy model. Two faulty situations that may appear during the system operation and the simulations conditions that are imposed in order to characterize the faulty operation are discussed. The two possible faults that are described are the rope sliding on the sheave and the sheave ageing. For each situation, for faulty and non-faulty case, data is generated from the virtual representation of the system and used to train a machine learning model. The capabilities of the developed machine learning model are tested in the end.

7.1 System Architecture

An electro-mechanical elevator system uses an electrical motor to drive the sheave-rope transmission that allows to move the passenger cabin in a controlled manner. The elevator system is mainly composed by a cabin frame that is used to carry the passengers, a counterweight that helps to lift the cabin, an electrical motor, the control unit, cables, sheaves, guiding rails, a brake system, gear. The counterweight is introduced to assure a balance of the weight and stability of the whole system by applying a force of opposite direction to that of the cabin. In this way, the load is lifted easier and faster, reducing the motor torque and saving

energy. The brake system works as a safety element when the power is lost. The brake consists of a pair of elements that apply pressure to a pulley or disc placed on the motor shaft. When the brake force/pressure is applied, the friction increases and the electric loss brake is created. The gear works as a reducer for the motor speed. The motor rotates the gear that is connected to the sheave and the speed is reduced with the gear ratio. The cabin is chosen based on the maximum allowed mass and volume restrictions; it presents an automated door system and the possibility to impose the desired floor. The cabin is connected to the system through the guiding rails and the ropes.

The elevator is actuated by a PMSM that is connected to the mechanical system together with an inverter a control unit. The cables characteristics are: strength class of 1570 $[N/mm^2]$, rope diameter of 8 [mm], Young's module of 95 $[kN/mm^2]$ and a metallic section of 23 mm^2 [133]. The attached control unit relies on the repetitive control technique. It is a suitable method for applications with periodic references [134]. Integrated into the elevator system, the repetitive control maximizes the elevator speed while keeping the comfort constraints unchanged [135]. This an important feature for lift applications because during its operation, disturbances caused by torque ripples, eccentricities of bearings, pulleys and rail guides appear and this type of control helps to compensate them. At the same time, the control takes into account the system non-lineartites, such as the modification of rope stiffness and mass with the length.

A schematic representation of the system under study, where the main components are identified, is presented in Fig. 7.1. The most relevant parameters of the system can be identified in Table 7.1. [135].

Table 7.1: Relevant parameters of the system under study

Parameter	**unit**	**value**
Cabin mass	kg	600
Counterweight mass	kg	1650
Sheave Radius	m	0.5
Gear ratio	-	1/10
Cabin Viscous Friction	N/m/s	1
Sheave Viscous Friction	Nm/rad/s	15
Rope Youngś Module	N/m^2	$2.1\ 10^9$
Maximum reachable height	m	75

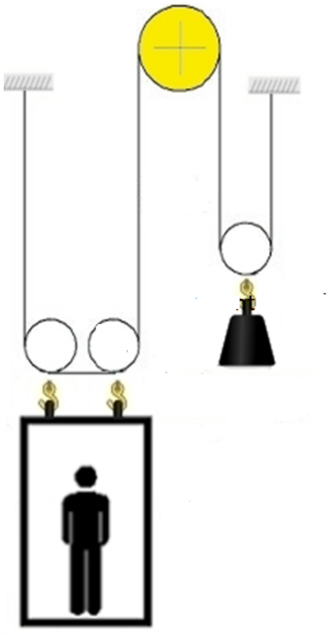

Figure 7.1: Elevator schematic representation.

7.2 Electrical Motor for Driving

The elevator uses an electrical motor to drive the system and move the cabin. The electrical motor used is a Permanent Magnet Synchronous Machines (PMSM) with ten pole pairs topology. The stator windings are connected in a star configuration. The parameters of the machine integrated within the system is presented in Table 7.2.

Table 7.2: Relevant parameters of the electric motor

Parameter	**unit**	**value**
Rated Voltage	V	340
Rated Current	A	16.2
Rated Speed	rpm	191
Pole pairs	-	10
Phase resistance	Ω	1.2
L_{d}	H	0.015
L_{Q}	H	0.009

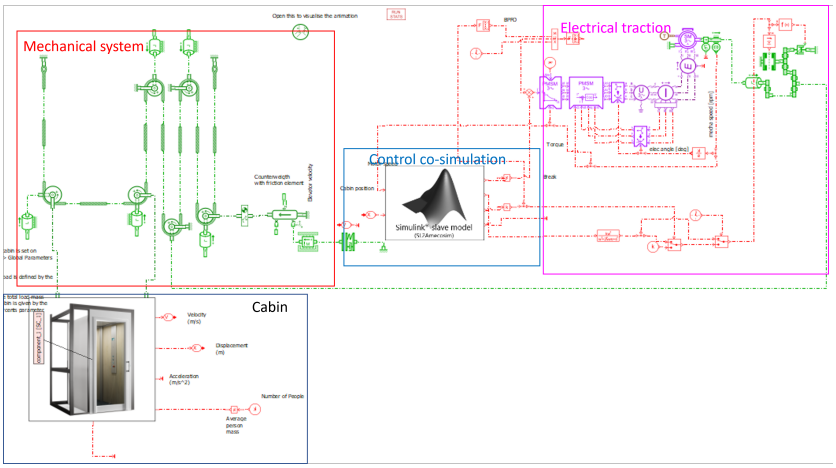

Figure 7.2: Elevator virtual model.

7.3 Virtual Model Implementation

The elevator system is modeled at system level with the help of Simcenter Amesim, a software that allows advanced modeling of mechatronic systems in a dynamical environment. Starting from the characteristics of the real system, a virtual representation is implemented. This way, the designer uses only important features of the system under study, leaving the unnecessary details aside. The resulting reduced order model has to find a trade off between accuracy and computational time because it will work in parallel with the real system to support its operation and monitor the working conditions.

The elevator model developed in Simcenter Amesim is presented in Fig. 7.2. The functional representation of the system is obtained here. The mechanical system consists in ropes, sheaves, guiding rails, counterweight, inertial loads, friction elements. The ropes present variable stiffness, elasticity and damping, as the active cable length modifies with the position of cabin. A real cable modifies its viscous friction during operation. Therefore, to include this effect, the dynamic model of the cables contains a variable mass too. The cabin model includes two parts: a fixed mass representing the frame and a variable mass that represents the fluctuation of people inside the cabin.

The electrical traction system consists in the electrical motor, attached power electronic modules, the reducer and the brake system. The PMSM is represented by an average model, using a linear inductance based electromagnetic model. The brake is represented using a rotary friction torque generator that works only when the power is lost.

Due to the fact that Simcenter Amesim is specialized into model-

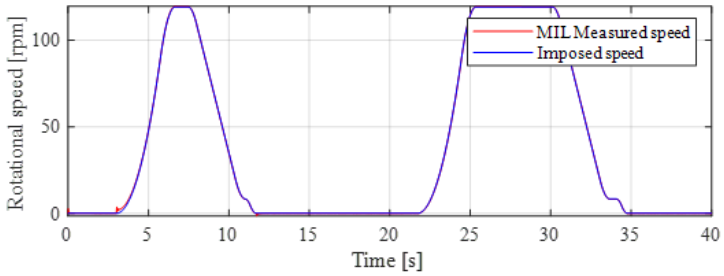

Figure 7.3: Speed Imposed by the controller vs. Simulated Motor speed.

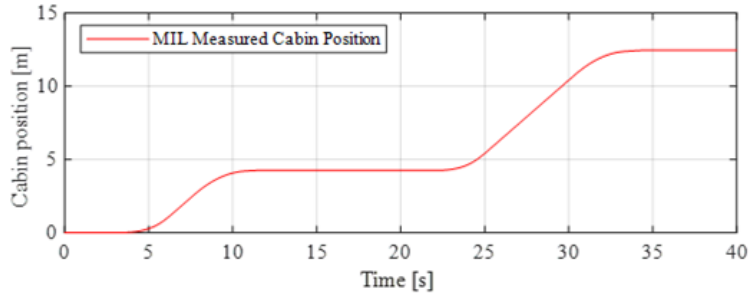

Figure 7.4: Simulated Cabin position.

ing of mechatronic system, the control is developed in Matlab/Simulink, known for its performances into the field of control. The repetitive control method is implemented within Matlab/Simulink in order to control the cabin trajectory, while keeping some key performance indicators (KPIs) under a specific threshold. These KPIs are set in order to assure a comfortable ride: maximum speed of 1 [m/s], maximum acceleration of 0.6 $[m/s^2]$, initial jerk of 0.2 $[m/s^2]$. The control capacity to meet the plant demands are is tested within a co-simulation environment. This configuration allows to use Simcenter Amesim as Master and Simulink as Slave and import the Simulink model into Simcenter Amesim. The problem is solved using Amesim's solver. The capacity of the controller to perform well under different conditions is tested using a Model In the Loop (MIL) configuration. Firstly, the controller is verified by imposing a reference motor speed. Then other KPIs (e.g., acceleration values, cabin position, cabin speed, torque values) are kept under observation to see if the model works properly and the controller behaves as intended.

Figure 7.3 displays the reference motor speed imposed and the model measured shaft speed. As it can be seen, both curves are overlapped, meaning that the controller succeeds to perform well. Moreover,

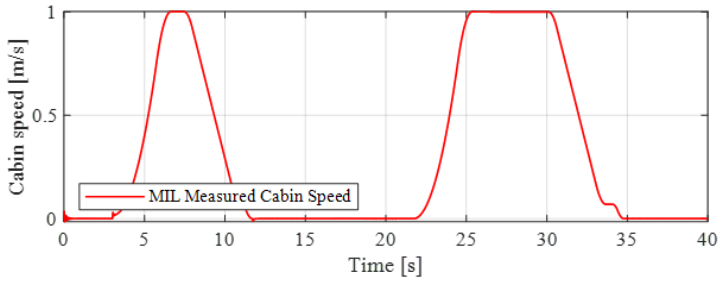

Figure 7.5: Simulated Cabin speed.

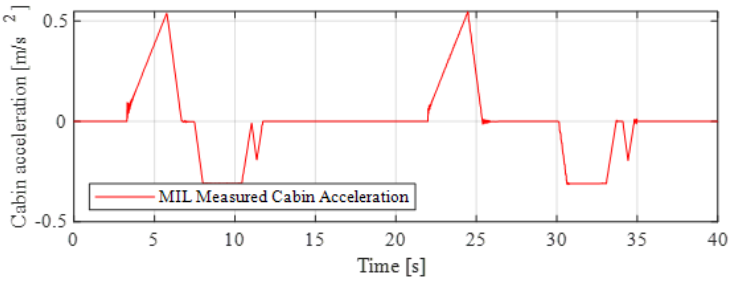

Figure 7.6: Simulated Cabin acceleration.

the cabin reaches desired floors, as presented in Fig. 7.4, while keeping the maximum value of velocity under 1 [m/s] and a maximum acceleration peak of 0.6 $[m/s^2]$. Figures 7.5 and 7.6 depict the values of cabin velocity and acceleration, respectively.

7.4 Virtual Model Validation

The accuracy of the developed elevator virtual model is tested by comparing the results obtained from simulations with the experimental ones. For the validation, the controlled value is the motor speed and the observed values are the torque developed by the motor, cabin speed and cabin position.

Two scenarios are presented here. The first one is characterized by an ascending ride of the cabin, from the ground floor to an intermediate floor, carrying a load equal to 400 [kg]kg. The second tested scenario is defined by the ascending ride of the cabin from the intermediate floor to the ground floor with the same load. The rotor speed is imposed for both model and the real system. The motor speed imposed in both cases is displayed in Fig. 7.7 (a) for the first validation scenario and in 7.7 (b) for the second validation scenario. The figures present with blue the im-

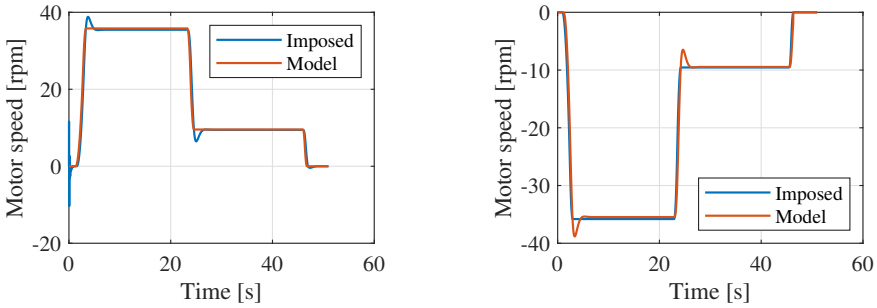

Figure 7.7: Imposed and modeled motor speed a) Ascending ride, b) Descending ride.

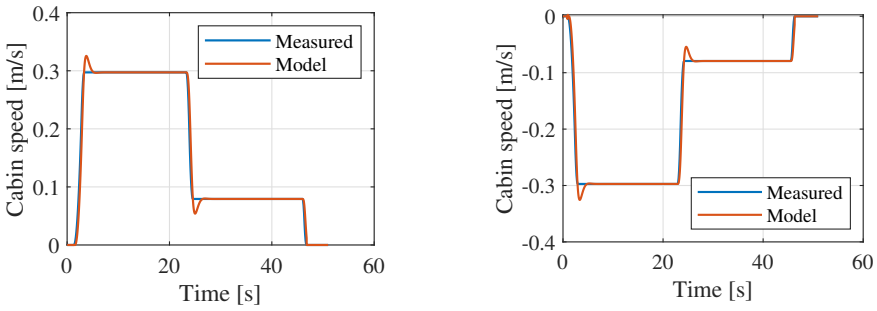

Figure 7.8: Measured and modeled cabin speed: a) Ascending ride, b) Descending ride.

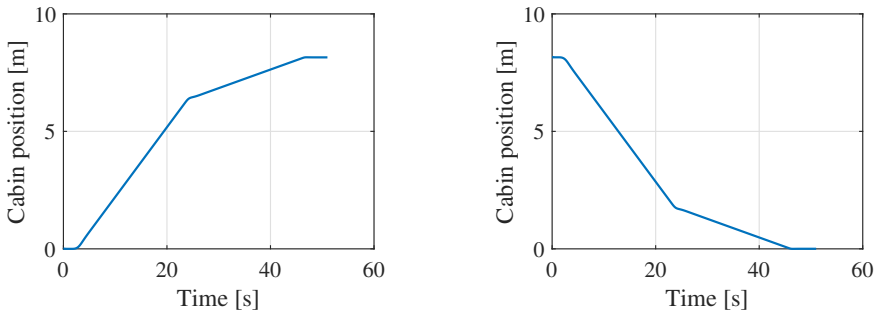

Figure 7.9: Cabin position: a) Ascending ride, b) Descending ride.

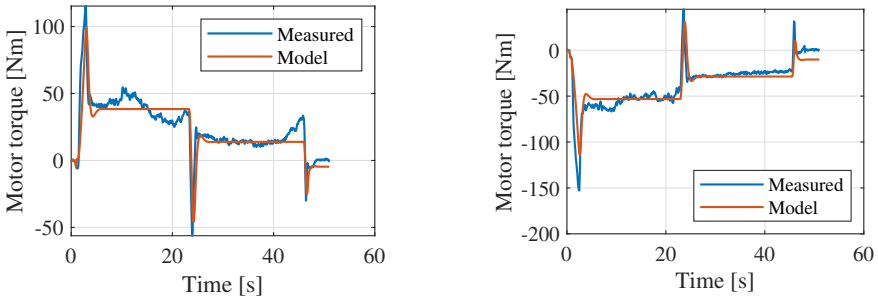

Figure 7.10: Measured and modeled motor torque: a) Ascending ride, b) Descending ride.

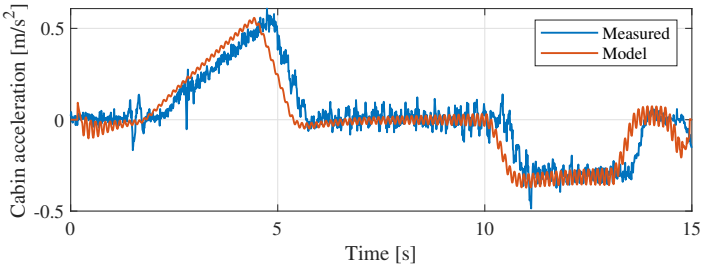

Figure 7.11: Measured and modeled cabin acceleration.

posed values and with red the values from control loop. As the motor operates, the sheave-rope transmission system moves the cabin. Therefore, the cabin moves with a speed displayed in Fig. 7.8 (a) for ascending case and in Fig. 7.8 (b) for descending validation scenario. In both cases, the speed is expressed in m/s and the waveform obtained from measurements is displayed with blue and the modeled cabin speed is displayed with red. For both simulation scenarios, it can be observed that the modeled values match the measured ones. The cabin presents several states: at the beginning, the lift accelerates at a constant rate, then it reaches a speed of 0.3 $[m/s]$ and keeps this speed constant until it reaches a certain vertical position. This is followed by a deceleration at a constant rate until the cabin speed is small enough so that it can reach with high precision the desired floor. Based on these states, the cabin trajectory is established. The cabin trajectories for elevator ascension is presented in Fig. 7.9 (a). It is visible that the cabin goes up faster in the first 25 sec when the motor accelerates and operates at constant speed. After this interval, the cabin goes up slower in order to reach the desired floor and reduce the position error. The same applies for cabin descent, identified in Fig. 7.9 (b), when the cabin goes from a higher floor to the ground floor.

The electromagnetic torque developed by the motor at imposed load and rotor speed is presented in Fig. 7.10 (a) and (b) for the two validation conditions. When comparing the measured and simulated values, it is seen that in both cases, the electromagnetic torque is obtained as an average value from simulations. This is a direct consequence of the way the virtual model is built in Simcenter Amesim, where an average model is used for electrical motor. However, it can be seen that the obtained electromagnetic torque values are able to follow the track of the measured values with increased accuracy, even when high peaks appear. These observations are valid for both ascending and descending tests.

7.5 System Faults Description

The elevator systems are subject to many types of faults. A fault can damage the system and determine the removal from service, but mild faults affect the system's performances and they can be perceived by the user. Some main performances that should be monitored during the operation of a system are the continuity of service (monitor the health state of invertor, motor, brake), vibrations and oscillations, trajectory shape, distance error at the arrival floor, travel time, energy consumption. These are just few characteristics of the system that are affected by faults that appear in different components.

These faults usually lead to severe economic problems related to repair costs or production shutdowns, delays or reduced efficiency. For this work, two faults are investigated and a machine learning model is developed in order to perform condition monitoring. As the sheaves and the ropes are the most worn elements from elevators, the two faults that are taken into account are the slip of the cable, when the rope is shifting on the pulley and an cabin is not able to reach the desired vertical position, and the degradation of the sheave.

The normal (i.e., non-faulty) operation of the system for no-load case, when the cabin moves from the ground floor to the maximum floor can be identified in Fig. 7.12. For the no-load case, it is considered that there are no passangers inside the cabin and the system lifts only the cabin own weight. Therefore, a negative electromagnetic torque is encountered in Fig. 7.12 b) because the cabin is lifted by the counterweight. The trajectory of the cabin is presented in 7.12 c). The cabin moves with the velocity displayed in 7.12 d), having a maximum value of 1 [m/s].

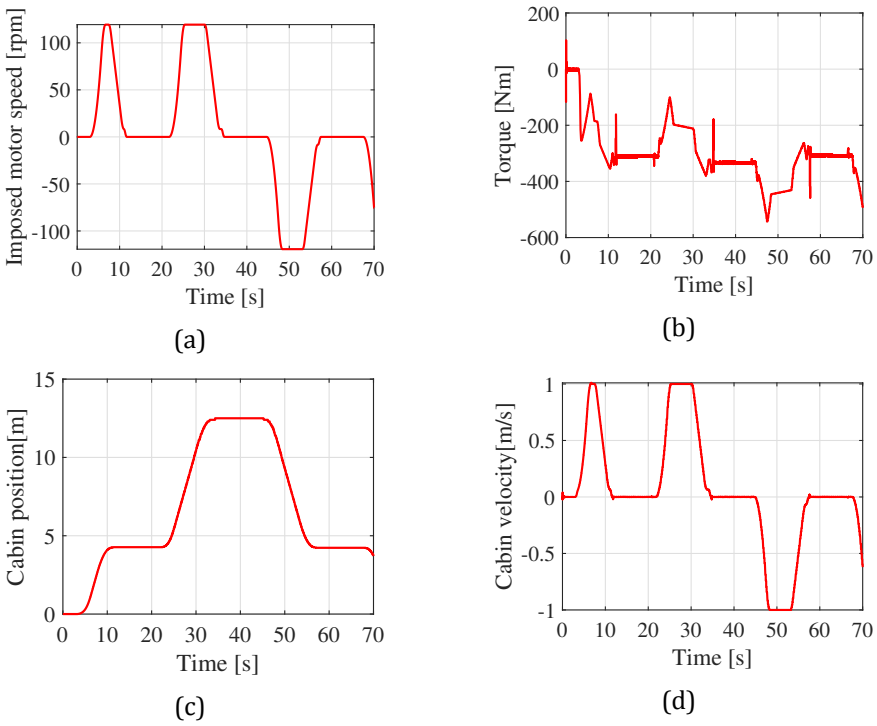

Figure 7.12: Elevator results for load 0 case a) Imposed motor speed, b) Simulated electromagnetic torque, c) Cabin position and d) Cabin velocity.

7.5.1 Fault 1: Cable Slip

A non faulty system operation requires a proper contact between the rope and sheaves. The rope – sheave connection coefficient of friction is a dominant factor in controlling the traction driving force. Most of the times, this coefficient is affected by improper operations. An oversized counterweight used to reduce the operational costs (i.e., the motor will develop less power) or a cabin overloading lead to slippage. A hard braking intervention can shake the system and cause rope slippage as well [136]. However, these aspects are already known and can be diminished through optimization in the design stage. More interesting and harder to forsee in the design stage is the slipping caused by external factors. In time and under action of increased tensions, the rope diameters can be affected, or the oil that assures the cotact between the ropes and the sheaves looses its properties, or even the lubrication is affected by either using excessive oil or by having an oil leak. These situations translate into a modification of the friction coefficient, the cable slips on the surface of sheave and the cabin motion cannot be controlled.

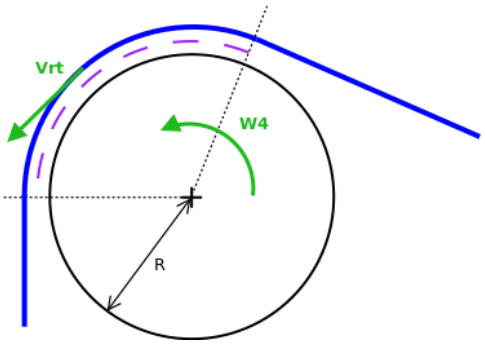

Figure 7.13: Sheave and rope schematic representation [138].

A graphical representation of the rope – sheave system is identified in Fig. 7.13. Here, the contact between the two entities is marked with purple dashed line. When the dry friction force is changed due to one of the causes described above, the rope is decoupled from the rotation of sheave. A rope tangential velocity, v_{rt}, appears and the rope slides. The value of tangential force is determined using the capstan equation [137]:

$$\mathrm{F_{rope}} = \mathrm{F_{resistance}} e^{\mu\beta} \tag{7.1}$$

$$\mathrm{F_{resistance}} = \min(|\mathrm{F_{end_1}}|, |\mathrm{F_{end_2}}|) \tag{7.2}$$

where μ stands for the coefficient of friction, β is the wrap angle of the rope that is wrapped around the sheave and $F_{resistance}$ defines the smallest value between the rope ends forces.

In order to build a machine learning model for condition monitoring and fault identification, a series of data must be generated and used in the model learning phase. The data base is easily generated from the developed high fidelity model. Due to the fact that the model is parameterised, the simulation conditions are straightforwardly modified. A full factorial design of experiments is used to vary the friction coefficient from 1 (ideal case) to 0.1 with a step of 0.1 and the cabin load from 100% of maximum load to 0% with a step of 25 %, where 0% means that the cabin travels empty and 100% means that the cabin travels maximum loaded.

7.5.2 Fault 2: Sheave Degradation

Among the most commonly problems encountered during an elevator inspection is the sheave properties degradation mainly caused by war and tear [139]. The sheaves are in action every time when the elevator operates and need to support the system weight. In time, the sheaves are inevitably affected and degradation appears. If the sheave is damaged,

the integrity of whole traction system is threatened. If the sheaves deteriorate up to this point, the safety is highly affected, with immense impact on the maintenance costs [140]. This type of fault should be addressed early, when incipient signs of degradation appear. In time, the sheave diameter its diminished due to wear and tear and the transmission efficiency is affected. A corrosive medium, humidity, operation conditions such as a hard brake, driving under overload conditions or unbalance problems accentuate the fault. The torque, T, and the sheave efficiency, e, are computed in function of the state mode (i.e., braking or accelerating) with respect to the rotating velocity, ω:

$$\begin{aligned} \mathrm{T} &= \mathrm{T}_{\mathrm{sheave}}\mathrm{e}, \mathrm{when}(\mathrm{T}\omega < 0) \\ \mathrm{T} &= \mathrm{T}_{\mathrm{sheave}}/\mathrm{e}, \mathrm{when}(\mathrm{T}\omega > 0) \end{aligned} \tag{7.3}$$

For a continuous system operation, the transition from one state to another is done through a hyperbolic function.

As the objective is to develop a machine learning model that supports the system during its operation in order to monitor the states and predict faults in their incipient phase, a series of data is needed to be generated and harnessed. The data is obtained from a series of simulations performed on the parametric model build in Simcenter Amesim. The advantage of using this model is that the actual system is not subject to thousands of operations under risky conditions. The simulations are performed for different conditions, both normal (i.e., non-faulty) and faulty. The input space is generated through a full factorial design of experiments that takes into account the sheave efficiency, sheave diameter and cabin load. The sheave efficiency is varied from 1 (ideal case) to 0.1, with a step of 0.1. The sheave diameter is modified from its nominal value to a reduction of -14% from its nominal value, with a step of 1.25% from the nominal value. Besides this, the load available in the cabin is varied from 0% of its maximum value to its maximum value with a step of 25%.

7.6 Machine Learning Model Development

A machine learning model is used to process the data coming from the system, decide if the system works under normal or faulty conditions, evaluate the faulty level and distinguish between different faults. The data obtained from the two situations considered above, rope slip and sheave degradation, are post-processed and harnessed. They are split in training, testing and validation data a machine learning model is developed. But before that, an appropriate machine learning algorithm is chosen based on the obtained data set. Because the information is in a form

of time-series waveforms that comes in sequences and with dependencies between data, Long Short-Term Memory (LSTM) algorithm is selected to build the fault identification module.

7.6.1 Long Short-Term Memory for Classification

Long Short-Term Memory Networks belong to the class of recurrent neural networks (RNN) that are specialised in classifying sequential data with long-term dependencies between time steps [141]. The LSTM keeps information about previous data for a time interval defined by the input data type. This method is highly applied in data classification, language analysis, sentiment analysis, speech recognition, translation or image processing. LSTM is part of the deep lerning class and its key features are: possibility to memorize past information for a random time, robustness to input noise and reduced training time [142].

LSTM has a structure formed of four neural networks and multiples memory blocks, known as cells. The LSTM architecture is graphically represented in Fig. 7.14. The cells are the ones that keep the information during time and the manipulation on the stored data is done by three gates: forget, update and output gates [142]. The first one, forget gate helps to remove the information that is no longer necessary. It receives two input signals, the input at time t, x_t, and the output given by the previous cell, $h_(t-1)$. The two inputs are multiplied with the weight matrices, w_f, and the final results is given by adding the bias, b_f. Afterwards, the result is processed by an activation function, f, the most commonly being the sigmoid function. The function outputs a binary value, 0 if the data is forgotten and 1 if it is still used. The forget equation, f_f, is:

$$f_f = f(w_f[h_{t-1}, x_t] + b_f) \tag{7.4}$$

The input gate adds new relevant information to the model. The new information is passed through an activation function using inputs $h_(t-1)$ and x_t. Afterwards, all the values between the input $h_(t-1)$ and the input at time t, x_t are passed through a tanh function, resulting data with a range between -1 and 1. These are multiplied with the activation function results. This is described mathematically as follows:

$$f_i = i(w_i[h_{t-1}, x_t] + b_i) \tag{7.5}$$

The output response is given by the model through the output gate. The tanh activation function is used firstly, resulting in a vector. Afterwards, the information is passed through a sigmoid function and filtered by the values to be remembere using the same inputs, $h_(t-1)$ and x_t. The

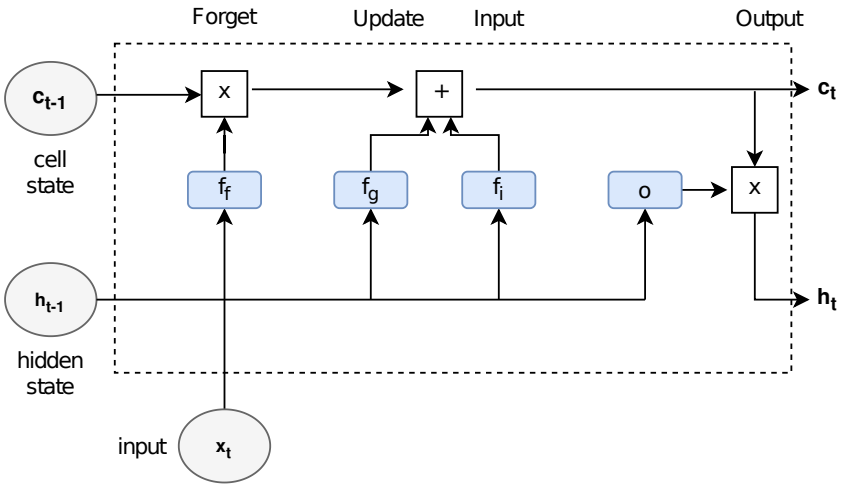

Figure 7.14: LSTM architecture [141].

result of this operation is multiplied with the vector and exported as the output. The output function is defined by the output activation function, output weights and biases:

$$f_o = o(w_o[h_{t-1}, x_t] + b_o) \tag{7.6}$$

One of disadvantages of LSTM is the increased learning time, compared to simpler algorithms, like feed-forward neural networks or SVMs. This is due to their complex structure that may require larger data set size and may impose scalability limits. At the same, because the model is trained in a sequential process, the tasks cannot be parallelized.

7.7 Fault Detection Model

Two data sets are obtained by performing design of experiments, as presented in previous sections. The data is harnessed using two LSTM, one for each fault. The two LSTMs are trained with the time-dependent extracted values in order to learn the long-term data dependencies, considering the multivariate time series input. The two developed LSTMs are then connected together to monitor the condition states of the elevator and identify the faults in their early stages. This way, all three situations defined by the presence of one fault or another, both faults or normal operation can be identified. The machine learning model defined by the connection between the two LSTMs is presented in Fig. 7.15. It can be seen that the the two models are connected using a dropout layer. Dropout is a common regularization method used in deep learning that sets to zero

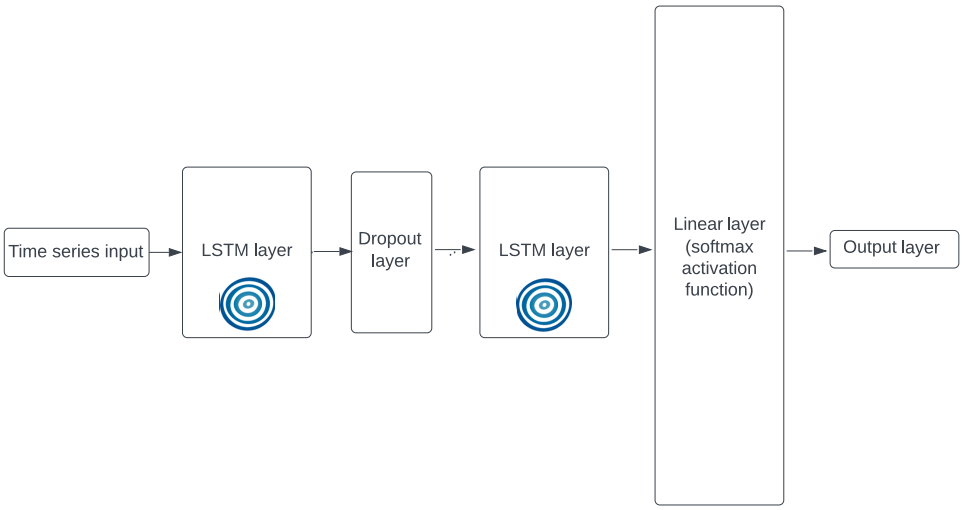

Figure 7.15: Neural network structure.

a percent of nodes from the input and hidden layers [143]. It is introduced to avoid issues created by overfitting. The first LSTM network uses as input the last hidden layer state of the first LSTM network. Afterwards, the result obtained from the last LSTM network is transferred tp a linear layer and processed by a SoftMax activation function. The SoftMax function transforms the response into the probability of failure. Therefore, a classification of the response into normal or faulty condition and the type of faults is performed.

The LSTMs structures are developed by learning the time dependencies of the data that is post-processed in order to get the best accuracy – computational trade-off. In both cases, the values extracted from simulations are elevator brake condition (it can be either coupled or decoupled), motor speed, motor electromagnetic torque, cabin position, cabin velocity and cabin acceleration. Based on their evolution in time, the machine learning model identifies a fault pattern. The learning process follows a pre-defined workflow:

1. Collect the time-series datasets obtained for the two investigated faulty situations.
2. Impose the constraints and limits for each fault that are used during the classification process.
3. Standardize samples.
4. Random split the samples based on their destination in 60% for training, 20% for validation and 20% for testing.
5. Train the model using different batch-sizes in order to obtain an optimal cost time – generalization capacity trade-off.

6. Evaluate the model behavior by computing the classification metrics on the test dataset.

The developed machine learning model identifies the faults by classifying them into three classes. The three cases are described by a specific behaviour of the extracted performances and user-defined thresholds. The three classes used for training are:

Class 1 : Non-faulty operation.

Class 2 : Fault 1 – Cable slip.

Class 3 : Fault 2 – Sheave Degradation.

After the classes are defined, each input is labeled and categorized into a single class. The extracted dataset is formed of 50 multivariate time series samples for the first fault and 110 multivariate time series samples (both normal and abnormal elevator operation) for the characterisation of the second fault. Each time series is defined by 70000 time steps, from 0 to 70 seconds.

As presented in the above described workflow, the third step in building the machine learning model consists in data standardisation. The sandardisation helps reducing the data range, usually between -1 and 1, as in this case, and reducing the training time [144]. Standardisation is a common method to scale the data by converting the probability distribution of an input variable to a Gaussian distribution with zero mean and unit variance. The process consists in computing the mean value for the training samples, u and dividing it with the standard deviation of the training samples, s. This allows to have all the features centered around 0 and corresponding variances of the same orders. This leads to a faster learning process and an increased model accuracy, as all the variances are on a similar scale and the optimisation function is not impacted by some values more than by others. The Adam gradient descent algorithm, selected for this study, has a faster convergence rate in this case. Data is standardised by making use of Sklearn's StandardScaler [145], where the standard score of every sample x is:

$$z = \frac{x - u}{s} \tag{7.7}$$

A very common problem that appears when building a machine learning model is overfitting. This is defined by a model with good performance on the training set but poor generalization capacity. To avoid overfitting, the dataset is divided into training, validation and test samples, and used in different stages to learn and evaluate model capabilities. For the presented study, the dataset is randomly divided into 60% for training, 20% for validation and 20% for testing. Because the dataset size is small (under 160 samples), the batch size is chosen to be equal to training

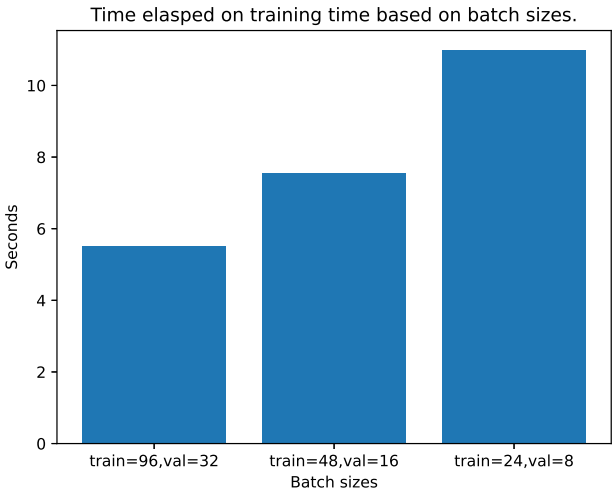

Figure 7.16: Training Time.

and validation dataset sizes, 96 for training and 32 for validation. This is the best configuration, as it can be observed in Fig. 7.16, where the training time versus batch sizes is displayed. For the batch size of 96 for train and 32 for validation, the training time is shorter compared with other configurations because back propagation is performed only one time for each training epoch.

Moreover, because the fault identification task is a classification problem with multiple classes, in the training phase, an Adam optimization function [146], with Cross Entropy loss function is introduced.

7.7.1 Model Metrics

The performances of a classification model can be quantified using several metrics. For the LSTM model developed for faults classification, confusion matrix is used to obtain the loss, accuracy, F1 score of the model.

Confusion matrix gives a classification of the resulting model predictions based on their real class. A True Positive (TP) appears when the model predicts a normal condition (Positive) and it is true. A True Negative(TN) appears when the model predicts a faulty operation (Negative) and this is true. The False Positive(FP) is defined by a normal operation prediction, but its real state is faulty. The False Negative(FN) is defined by a faulty prediction and this is false [147]. The crucial performances derived from the confusion matrix are the precision and recall.

The precision gives information about how many true positive cases are in all the positive predicted. The precision is a value between 0 and 1,

as follows:

$$Precision = \frac{TP}{TP+FP} \tag{7.8}$$

Recall is computing how many positive cases have been predicted correctly from all positive classes:

$$Recall = \frac{TP}{TP+FN} \tag{7.9}$$

Based on the described notions, the loss, accuracy and F1 scores can be defined. The loss is computed as the absolute difference between the real values and predicted ones. The accuracy gives information about how many cases have been predicted correctly from the total ones:

$$Accuracy = \frac{TP+TN}{TP+TN+FP+FN} \tag{7.10}$$

The F1 score measures both Recall and Precision at the same time. It defines the harmonic mean of Recall and Precision:

$$F_1 = \frac{2}{\frac{1}{Precision} + \frac{1}{Recall}} = \frac{2 \cdot Recall \cdot Precision}{Recall + Precision} \tag{7.11}$$

7.7.2 Results

The model accuracy is tested for different combination of model hyperparameters. An optimisation process is performed in order to obtain the highest model accuracy given by a suitable hyperparameters configuration. The model hyperparameters needed to be optimised and their variation interval are displayed in Table 7.3. The sampler procedure is based on TPESampler that uses Tree-structured Parzen Estimator algorithm [148]. The best hyperparameters configurations are obtained in a sequential process. Firstly, for each iteration, for each parameter, TPE fits two Gaussian Mixture Models (GMM). One GMM fits the best hyperparameters values, producing the density l(x) and the other GMM fits the remaining hyperparameter values, producing the density g(x). Afterwards, the algorithm selects the parameter value x that maximizes the ratio l(x)/ g(x).

The objective function consists in accuracy and F1 score maximisation. The best hyperparameters obtained from an optimisation with 500 trials are presented in Table 7.4.

The model accuracy, F1 Score and validation/training loss obtained for 200 epochs obtained for the LSTM network trained using the best

Table 7.3: Hyperparameters and domains.

Hyperparameter	Variation Interval
LSTM layers	[1,9]
Learning rate	[1 e^{-1},e^{-5}]
Dropout probability	[0.10,0.75]
Hidden size for LSTM networks	[32,512]

Table 7.4: Best Hyperparameters.

Hyperparameter	Best value
LSTM layers	2
Learning rate	0.01
Dropout probability	0.20
Hidden size for LSTM networks	32

combination of hyperparameters are displayed in Fig. 7.17. The model presents an accuracy of 96.75% and the F1 score is 0.96 in the testing phase, as it can be identified in Fig. 7.18). The evaluation metrics present some spikes caused by the stochastic gradient descent algorithm and epochs, where a large number of neurons are ignored in the model because of the dropout layer.

7.8 Intermediate Conclusions

In this chapter, a PMSM was integrated within an industrial system in order to drive the system and assure the movement of the mobile parts. The application considered in this chapter is an industrial electromechanical elevator. A efficient way of scheduling the elevator maintenance by monitoring the states conditions and decide whether the system operates under normal, warning or faulty conditions, and if it is necessary or not to stop the operation and intervene was presented. This method, condition monitoring, helps in the early detection of faults by giving continuous information about the system conditions. Once the system actual state is known, if a fault is identified in its incipient phase, the system can be rapidly disconnected without risking the safe and integrity of passengers.

The presented method consists in developing a Long Short-Term Memory Network based model for fault identification. Two common elevator faults were taken into account for this study, the rope sliding on the sheave and the sheave degradation, due to their impact on the system operation and maintenance costs. The data necessary to develop the

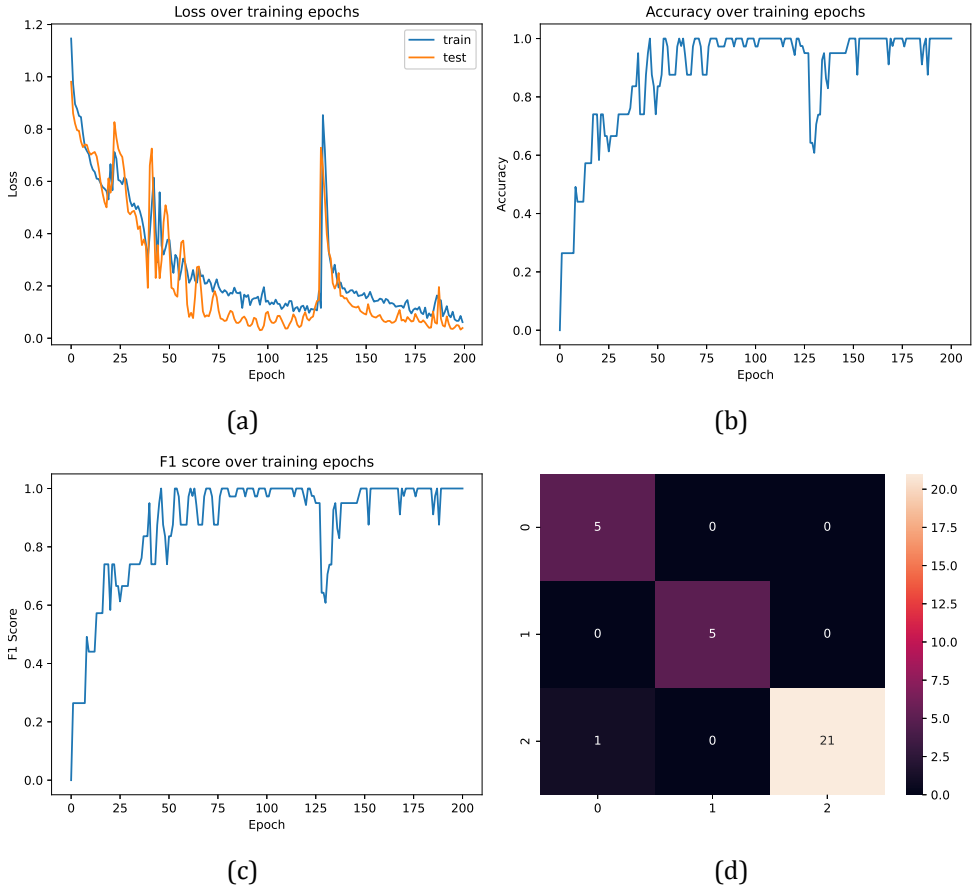

Figure 7.17: LSTM developed model metrics: (a) Loss, (b) accuracy, (c) F1 Score (d) and confusion matrix over the testing dataset.

model is generated from the elevator's digital twin created in Simcenter Amesim. The digital twin is able to provide all the necessary information under different operation conditions imposed by the user without risking the system integrity.

The model accuracy is tested for different combination of model hyperparameters using an optimisation proces in order to obtain the highest model accuracy given by a suitable hyperparameters configuration. The model presents, for the best hyperparameters, an accuracy of 96.75% and a F1 score of 0.96 in the testing phase. It was concluded that the LSTM model is able to monitor the system states and predict with high accuracy a fault in incipient phase.

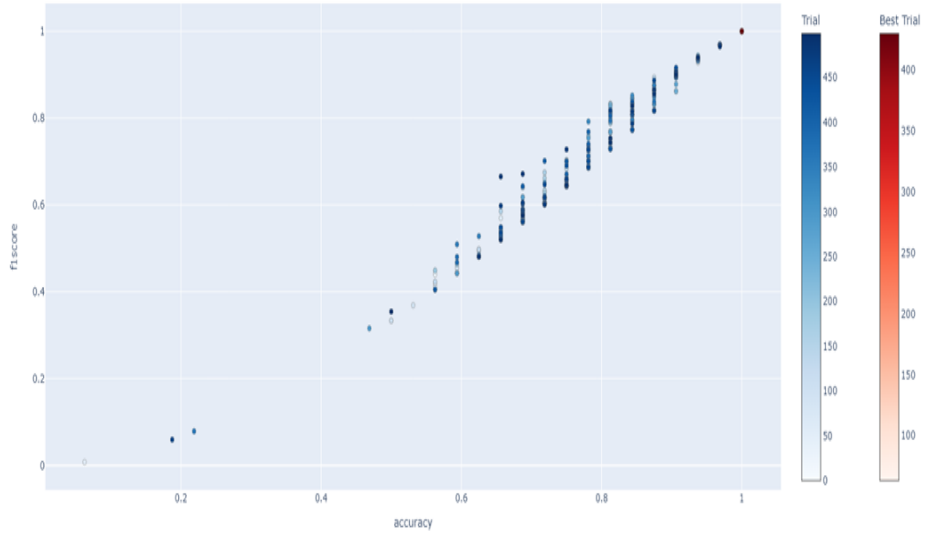

Figure 7.18: Trials and values based on accuracy and F1 Score.

8. Final conclusions and future work

The main objective of this thesis was to propose solutions to predict multi-physical characteristics of electrical machines and ease the design process. Surrogate models were introduced in the designing phase of an electrical motor, known as a complex problem due to the highly nonlinear nature of the system caused by the saturation of iron at high magnetic field strength values and to the requirements coming from different physics that come into conflict. Numerical, mathematical and machine learning based methods were proposed to predict the multi-physical characteristics of electrical machines and improve the decision making process during the design stage. The methods were analysed taking into consideration computational costs and accuracy during the optimisation routines , mandatory when designing an electrical machine.

The thesis is divided into four main parts:

- the multi-physical phenomena that arises during the operation of electrical machines and the best methods to predict them.
- modeling at the component-level of the multi-physical behaviour using mathematical and machine learning methods.
- methods to reduce the noise vibration and harshness of electrical.
- prediction of different faults of an industrial system

8.1 The multi physical characteristics of electrical machines

Chapter 2 has presented a comprehensive description of the fundamental multi-physic phenomena that arise in an electrical machine and the methods suitable for prediction and estimation of these attributes. At the same time, the interior permanent magnet synchronous machine used as application for this study was presented. The parametric models employed for structural and electromagnetic analysis were introduced in the same chapter. The degrees of freedom of each parameterised model, construction specifications, analysis details and parameter variation limits were thoroughly discussed.

8.2 Electromagnetic modeling of electrical machines

Chapter 3 has discussed a way to emulate the electromagnetic behaviour of electrical machines through model order reduction obtained using either mathematical or machine learning based approaches. The solution came as an alternative solution to the time consuming Finite El-

ement Analysis that are not suitable for system level analysis or for real time applications. During this chapter, several methods commonly used in the technical literature were presented. These models, based on the general voltage equations expressed in different forms, based on the values exported from FE analysis (i.e., inductances or fluxes), are presented in comparison with a reduced order model developed using an artificial neural network model. The developed ANN module fits the relationships between currents and fluxes and between currents and electromagnetic torque.

It has been demonstrated that the combination of the developed machine learning model with an adaptive learning model with the objective to reduce the data dimension improves the computational time costs. Compared with the time requested by the traditional method to model the electromagnetic behaviour of electrical machines based on variables stored into LUTs, the ANN method reduced the time costs with 50%, including the time necessary to train the model. This value is obtained by generated data through Sobol sequence when the data generation and machine learning process stopped when a prediction error under 1 [%] was reached.

The capacity of the resulting machine learning model obtained by generated data with the Sobol sequence to compete with FE method was tested by comparing the currents and electromagnetic torque obtained from both methods, taking as reference the FE analysis. The results showed that the model is higly accurate in every conditions, even if the machine operates under high saturation conditions.

The model accuracy was further demonstrated by comparing the results obtained by running the developed machine learning model integrated within the dynamic model that has attached the motor control based on Field Oriented Control (FOC) with real experimental measurements. By comparing the torque, currents and the motor speed, it was proven that the dynamic model performs precisely like the test-bench. During this test, it was also proven that the proposed ANN model is precise and suitable for HiL integration, having instant running time.

8.3 Analytical modeling and prediction of motor vibrations

Chapter 4 presents analytical methods to evaluate the structural and vibro-acoustic characteristics of electrical machines. Although FE analysis allows to obtain accurate results of electrical machines complicated geometries, the evaluation time is high and memory consuming. On the other hand, analytical methods allow a fast evaluation of structural

characteristics, without needing to provide a detailed description of the machine. This is beneficial, especially in the design stage, when a first evaluation of motor performances is performed, or when the product is introduced in an optimization loop where thousand of designs are evaluated and the time cost is crucial.

The analytical methods were used to predict the stator deformations that occur at specific frequencies, called natural frequencies and the stator forced response. To compute these values, the analytical method uses a ring model to determine the structural characteristics. By analysing the natural frequencies results in comparison with the FE method, some conclusions can be drawn. The analytical method tend to underestimate the values of the global eigen-frequencies. The analytical method is not precise, the relative error being high. The maximum eigen-frequency relative error, $f_{(x,0)_{err}}$, between analytical method results, $f_{(x,0)_a}$, and FE based analysis eigen-frequencies, $f_{(x,0)_{FE}}$, is 26.62% for mode 2 of vibration. The method is able to predict the natural frequency of mode 0, the error being under 2%.

Considering the high obtained errors of the stator natural frequencies, for the vibration response, a semi-analytical method was involved. In this case, the natural-frequencies obtained from a FE analysis were included in the analytical formulation of displacement computation. Besides that, two improvements in the semi-analytical formulation were considered. The first one is the introduction of tangential forces as radially exciters, besides the radial forces, and the second one is the inclusion of the tooth modulation effect in the displacement formula. The displacement relative error $Y_{m,err}$ for each significant mechanical order m between the vibration-synthesis and semi-analytical results ($Y_{m,VS}$ and $Y_{m,SA}$) showed that the analytical method tends to overestimate the vibration displacement values, compared with the FE method based on vibration synthesis. The lowest displacement errors were encountered in the case where the tangential forces were considered as exciters, besides the radial components, where a maximum error of 27% was encountered. The comparisons were done during both steady state conditions and run-up.

Finally, the computational time was assessed on a workstation with Intel Core i7-9850H CPU, 9^{th} generation, running at a frequency of 2.6 GHz, with 32 GB of RAM. For both analysis, it was noticed that the computational cost of FE method is higher. In the case of stator mode shapes evaluation, the analytical method takes 0.2 seconds to compute the first six global modes of vibration. On the other hand, the FE based analysis requires 102 seconds. For the vibration computation, considering that the force computation was done a-priori, the analytical method exhibits a result in less than 0.6 seconds, whereas the FE based method indicate the

results in 183 seconds.

To conclude, analytical methods are fast, easy to implement and do not require design details to evaluate the structural characteristics. This is important in the early design stage, where limited information about design are available. On the other hand, they are less accurate, compared with FE models. The analytical methods can be used to evaluate the characteristics of a motor design, when the computational time is crucial, while a margin of error for the results is still acceptable.

8.4 Surrogate models to ease the design process

Chapter 5 has presented an original solution to the traditional design workflow of an electrical machine. Within this chapter, it has been demonstrated that the targets coming from different physics, electromagnetic, thermal, structural, NVH can be assessed and predicted in the early stage design, where the designer identifies the system sensitivities and decides if the designs meets imposed multi-physical performance targets.

The time cost of traditional optimisation routine based on FE models is reduced by building multi-attribute machine learning model, capable of predicting with high accuracy the multi-physical behaviour of electrical machines. The performances identified by the multi-attribute machine learning model from input geometrical parameters were electromagnetic torque, back electromotive force, motor components losses, stator natural frequencies, maximum stress experienced by rotor, vibration characteristics of the stator core. Parametric models of the motor were employed in design of experiments conducted through Latin Hypercube Sampling to generate the training data. Parametric 2D electromagnetic FE model was build to assess the electromagnetic targets, while parametric 3D structural FE models were developed for both rotor and stator in order to characterise their structural and NVH behaviour. For each physics analysed, individual machine learning model were developed, which were latter integrated into optimisation routine to enable the design process.

Different machine learning algorithms were tested in order to get the most suitable machine learning model for one physics involved. The models were trained with different data sets to get accurate results at the lowest computational time. The advantage of using the ML1000 machine learning model over FEA was quantified by conducting a stator geometry optimization routine. The improvement given by using the developed multi-attribute model in the optimisation process was demonstrated by analysing both accuracy and computational costs of the two methods. The obtained reults showed that the multi-attribute machine learning model provides accurate results, while significantly reducing the computational

time. Focusing on the computational costs, the studies showed that the machine learning model's computational cost is higher than the FEA one if the number of simulation needed to extract the training data are over the number of optimisation runs. Above this value, the multi-attribute model consumes less computational resources and time than the FEA method.

The advantages of this solution are:

- The optimisation process is performed in a reduced time, allowing to design a robust electrical machine with high performances faster, enhancing time to market. At the same time, the designer can perform more complex optimisation routines, as the method presents high accuracy at a low computational and memory cost.
- The multi-physical performances of electrical machines, including electromagnetic, losses, rotor stress and NVH characteristics, can be assessed in the early design stage.
- The NVH characteristics of the electrical machines can be predicted for run-up conditions.

8.5 Asymmetric stator slot opening geometry for PMSM NVH optimisation

Chaper 6 has introduced a method to reduce the NVH characteristics of the machine under study by introduction of slot opening geometrical asymmetry in the late design stage. The presented method consists in cutting one side of the stator tooth tip, while the other side of the tooth experiences additional soft magnetic material in order to keep the original slot opening width constant. By showing a comparison between radial displacements obtained for original motor design and three other optimisation results, it was demonstrated that the proposed method increases the noise and vibration levels.

The evolution of the NVH characteristics with the asymmetry introduced in the stator tooth tip was assessed through an optimisation process with the objective of reducing the NVH levels, while constraining the electromagnetic average torque value. It has been shown that the force density harmonics are changed when asymmetries are introduced and the vibration response is influenced by this change. Three optimisation results, defined by a reduction of electromagnetic torque of 8 %, 15 % and 23 %, were discussed. By comparing the symmetrical and asymmetrical cases, it was shown that the vibration response was increased for all three cases. Focusing on the full RPM-frequency range vibration response of multiples of the base mechanical frequency, the first order-cut ($f = 10 f_{mech}$) was increased with 1.5 % for $\mathrm{SO_{cut}} = 1.2$ mm asymmetry case and for the third case, defined by $\mathrm{SO_{cut}} = 1.76$ mm , the radial dis-

placement was amplified with 16.1 %, compared with original symmetric design. The results have indicated that the vibration response obtained at run-up was increased for all three cases. For a rotational speed of 1800 rpm, the vibration response was increased with up to 23 % for the third asymmetric case.

8.6 Condition Monitoring of an Industrial Elevator

Chapter 7 has introduced the system-level analysis of an industrial system equipped with a PMSM. For this industrial system (i.e., an electromechanical elevator), the whole assembly was analised in order to perform condition monitoring and fault identification. For that, the elevator was modeled at system level within Simcenter Amesim. The accuracy was tested using experimental data and the high accuracy model was validated.

The state conditions of the industrial elevators are monitored by a machine learning model in order to detect the faults in an incipient phase and improve the maintenance service. Two faults that frequently appear during the system operation were considered in this study: the rope sliding on the sheave and the ageing of the sheave.

The condition monitoring system was created using a Long Short-Term Memory Network model used for fault classification. The data necessary to build the condition monitoring model was obtained by conducting a series of simulations on the dynamic virtual model under faulty and normal conditions. On the parametrerised elevator model, the simulation conditions were directly modified, allowing for faulty conditions introduction. A full factorial design of experiments was used to vary the friction coefficient to simulate the rope sliding fault. The friction coefficient was varied from 1 (ideal case) to 0.1 with a step of 0.1 and the cabin load from 100% of maximum load to 0% with a step of 25 %, where 0% means that the cabin travels empty and 100% means that the cabin travels maximum loaded. For the sheave ageing situation, the sheave efficiency, sheave diameter and cabin load were modified through the same full factorial design of experiments. The sheave efficiency was varied from 1 (ideal case) to 0.1, with a step of 0.1, the sheave diameter was reduced with up to 14% from its nominal value, with a step of 1.25%. Besides this, the load available in the cabin was changed from 0% of its maximum value to its maximum value with a step of 25%.

Afterwards, the model accuracy was tested under different operation conditions and its high capability to predict faults in their incipient phase was demonstrated. The best model, developed by optimizing the hyperparameters, presents an accuracy of 96.75% and a F1 score of 0.96

in the testing phase. It was concluded that the LSTM model is able to monitor the system states and predict with high accuracy a fault in incipient phase.

8.7 Future work

The prediction of the multi-physical characteristics of electrical machines in the concept phase is a challenging task, where various innovations can be introduced in future research works.

The developed multi-attribute machine learning solution presented in this work is composed of a combination of various machine learning models that focus on individual targets coming from one physics domain. Therefore, each machine learning predicts the characteristics of a single physics. An interesting future research subject would be to develop a single machine learning models able to predict all the characteristics at a single run.

Another interesting future subject would be to include also the effect of manufacturing tolerances in the multi-attribute machine learning workflow. The electromagnetic values are highly influenced by such deviations and a prediction of their evolution in the early stage design could eliminate some sensitivities that can diminish the machine's performances.

Additionally, it would be valuable if the methods used to diminish the NVH characteristics by shaping the motor cross-section would be integrated in the analytical method for natural frequencies and noise and vibration characteristics prediction.

Another aspect that can be further explored is the introduction of different parametric stator and rotor models that allow for more complicated geometries with higher number of degrees of freedom.

Bibliography

[1] https://www.firestonecompleteautocare.com/blog/maintenance/electric-vs-hydraulic-power-steering/. (Accesed on 1.09.2023)

[2] T. Herold, S. Böhmer, "Data analysis in the production process of electrical drive systems," in Conference on Future Automotive Technology, 2017.

[3] https://iosh.com/health-and-safety-professionals/improve-your-knowledge/occupational-health-toolkit/noise/sound-levels-and-their-relevance/. (Accesed on 1.09.2023)

[4] Principal Laws and Methods in Electrical Machine Design, John Wiley & Sons, Ltd, 2013.

[5] P. S. Ghahfarokhi, A. Kallaste, A. Belahcen, T. Vaimann and A. Rassõlkin, "Review of thermal analysis of permanent magnet assisted synchronous reluctance machines," 2016 Electric Power Quality and Supply Reliability (PQ), Tallinn, Estonia, 2016, pp. 219-224, doi: 10.1109/PQ.2016.7724116.

[6] M. Popescu, D. A. Staton, A. Boglietti, A. Cavagnino, D. Hawkins and J. Goss, "Modern Heat Extraction Systems for Power Traction Machines—A Review," in IEEE Transactions on Industry Applications, vol. 52, no. 3, pp. 2167-2175, May-June 2016, doi: 10.1109/TIA.2016.2518132.

[7] Popescu, M.; Staton, D.; Dorrell, D.; Marignetti, F.; Hawkins, D. Study of the thermal aspects in brushless permanent magnet machines performance. In Proceedings of the 2013 IEEE Workshop on Electrical Machines Design, Control and Diagnosis (WEMDCD), Paris, France, 11–12 March 2013; pp. 60–69.

[8] Chiodetto, N.; Bianchi, N.; Alberti, L.; Improved Analytical Estimation of Rotor Losses in High-Speed Surface-Mounted PM Synchronous Machines. IEEE Trans. Ind. Appl. **2017** 53, 3548–3556.

[9] N. Bianchi, M. Barcaro, and S. Bolognani, 'Electromagnetic and Thermal Analysis of Permanent Magnet Machines', Finite Element Analysis - From Biomedical Applications to Industrial Developments, InTech, Mar. 30, 2012. doi: 10.5772/38777.

[10] G. Bertotti, "Hysteresis in Magnetism: For Physicists, Materials Scientists, and Engineers," Academic Press, New York, 1998

[11] D. M. Ionel, M. Popescu, S. J. Dellinger, T. J. E. Miller, R. J. Heideman and M. I. McGilp, "On the variation with flux and frequency of the core loss coefficients in electrical machines," in IEEE Transactions on Industry Applications, vol. 42, no. 3, pp. 658-667, May-June 2006,

doi: 10.1109/TIA.2006.872941.
[12] M. Popescu and D. M. Ionel, "A Best-Fit Model of Power Losses in Cold Rolled-Motor Lamination Steel Operating in a Wide Range of Frequency and Magnetization," in IEEE Transactions on Magnetics, vol. 43, no. 4, pp. 1753-1756, April 2007, doi: 10.1109/TMAG.2006.892291.
[13] A. Boglietti, A. Cavagnino, M. Lazzari and M. Pastorelli, "Predicting iron losses in soft magnetic materials with arbitrary voltage supply: an engineering approach," in IEEE Transactions on Magnetics, vol. 39, no. 2, pp. 981-989, March 2003, doi: 10.1109/TMAG.2003.808599.
[14] M. Barcaro, N. Bianchi and F. Magnussen, "Rotor Flux-Barrier Geometry Design to Reduce Stator Iron Losses in Synchronous IPM Motors Under FW Operations," in IEEE Transactions on Industry Applications, vol. 46, no. 5, pp. 1950-1958, Sept.-Oct. 2010, doi: 10.1109/TIA.2010.2060175.
[15] B. Funieru and A. Binder, "Simulation of electrical machines end effects with reduced length 3D FEM models," 2012 XXth International Conference on Electrical Machines, Marseille, France, 2012, pp. 1430-1436, doi: 10.1109/ICElMach.2012.6350066.
[16] D. E. Pinto, A. -C. Pop, J. Kempkes and J. Gyselinck, "Consideration of 3-D end-effects of surface permanent - magnet synchronous-machines through 2-D finite-element analysis," IECON 2019 - 45th Annual Conference of the IEEE Industrial Electronics Society, Lisbon, Portugal, 2019, pp. 957-962, doi: 10.1109/IECON.2019.8926662.
[17] A. Dalcali, and M. Akbaba, "Comparison of 2d and 3d magnetic field analysis of single-phase shaded pole induction motors," Engineering Science and Technology, an International Journal, June, 2015.
[18] Long, S. A., Zhu, Z. Q., and Howe, D. "Vibration behaviour of stators of switched reluctance motors," IEE Proceedings - Electric Power Applications 148, 3 (May 2001), 257–264.
[19] F. Chauvicourt, "Vibro-acoustics of rotating electric machines. Prediction, validation and solution", PhD Thesis.
[20] J. Le Besnerais, "Reduction of magnetic noise in PWM-supplied induction machines - low-noise design rules and multi-objective optimization", PhD Thesis, Ecole Centrale de Lille, 2008. English. NNT : . tel-00348730
[21] E. Devillers, M. Hecquet, J. Le Besnerais and M. Régniez, "Tangential effects on magnetic vibrations and acoustic noise of induction machines using subdomain method and electromagnetic vi-

bration synthesis," 2017 IEEE International Electric Machines and Drives Conference (IEMDC), Miami, FL, USA, 2017, pp. 1-8, doi: 10.1109/IEMDC.2017.8002072.

[22] F. Chauvicourt, S. Ciceo and H. Van der Auweraer, "On the Use of Vibration Synthesis to Ease Electric Machine Powertrain Design," 2019 IEEE International Electric Machines & Drives Conference (IEMDC), San Diego, CA, USA, 2019, pp. 1118-1125, doi: 10.1109/IEMDC.2019.8785108.

[23] H. Lan, J. Zou, Y. Xu and M. Liu, "Effect of Local Tangential Force on Vibration Performance in Fractional-Slot Concentrated Winding Permanent Magnet Synchronous Machines," in IEEE Transactions on Energy Conversion, vol. 34, no. 2, pp. 1082-1093, June 2019, doi: 10.1109/TEC.2018.2881043.

[24] H. Fang, D. Li, J. Guo, Y. Xu and R. Qu, "Hybrid Model for Electromagnetic Vibration Synthesis of Electrical Machines Considering Tooth Modulation and Tangential Effects," in IEEE Transactions on Industrial Electronics, vol. 68, no. 8, pp. 7284-7293, Aug. 2021, doi: 10.1109/TIE.2020.3000137.

[25] James R. Melcher, Continuum Electromechanics. Cambridge, MA: MIT Press, 1981. Copyright Massachusetts Institute of Technology. ISBN: 9780262131650

[26] Wheeler, R.; Dorfi, H.; Keum, B. Vibration Modes of Radial Tires: Measurement, Prediction, and Categorization Under Different Boundary and Operating Conditions. SAE Technical Paper **2005**.

[27] F. L. M. dos Santos, J. Anthonis, F. Naclerio, J. J. C. Gyselinck, H. Van der Auweraer and L. C. S. Góes, "Multiphysics NVH Modeling: Simulation of a Switched Reluctance Motor for an Electric Vehicle," in IEEE Transactions on Industrial Electronics, vol. 61, no. 1, pp. 469-476, Jan. 2014, doi: 10.1109/TIE.2013.2247012.

[28] M. Boesing, T Schoenen, K. A. Kasper, and R. W. De Doncker, "Acoustic modeling of electrical drives: Noise and vibration synthesis based on force response superposition," in IEEE Transactions on Magnetics, vol. 46, no. 8, Aug. 2010.

[29] N. Bianchi, S. Bolognani, D. Bon and M. Dai Pre, "Rotor Flux-Barrier Design for Torque Ripple Reduction in Synchronous Reluctance and PM-Assisted Synchronous Reluctance Motors," in IEEE Transactions on Industry Applications, vol. 45, no. 3, pp. 921-928, May-june 2009, doi: 10.1109/TIA.2009.2018960.

[30] O.A. Bauchau, J.I. Craig, "Structural Analysis", Springer Science Publication, 2009, p. 3

[31] M. Barcaro, G. Meneghetti and N. Bianchi, "Structural Analysis of the

Interior PM Rotor Considering Both Static and Fatigue Loading," in IEEE Transactions on Industry Applications, vol. 50, no. 1, pp. 253-260, Jan.-Feb. 2014, doi: 10.1109/TIA.2013.2268048.

[32] A.-C. Pop, J.J.C. Gyselinck, D. E. Pinto, I. Vintiloiu, "Optimization of low-power brushless PM-machines for automotive applications with focus on high-volume mass production," IEEE Trans. Ind. Electron. **2017**, 64, 9767–9775.

[33] S. Ciceo, F. Chauvicourt, J. Gyselinck and C. Martis, "Data-Driven Electrical Machines Structural Model Using the Vibration Synthesis Method," in IEEE Transactions on Transportation Electrification, vol. 8, no. 3, pp. 3771-3781, Sept. 2022, doi: 10.1109/TTE.2022.3164644.

[34] Digital Engineering Available online: `https://digitalengineering247.com/article/intersection-of-ai-and-simulation-in-the-automotive-industry/Artificial-Intelligence-AI`. (Accesed on 1.09.2023)

[35] S. Ciceo, F. Chauvicourt, J. Gyselinck and C. Martis, "A comparative study of system-level PMSM models with either current or flux-linkage state variables used for vibro-acoustic computation," 2019 IEEE International Electric Machines & Drives Conference (IEMDC), San Diego, CA, USA, 2019, pp. 1881-1888, doi: 10.1109/IEMDC.2019.8785326.

[36] M. R. Raia, M. Ruba, R. O. Nemes and C. Martis, "Artificial Neural Network and Data Dimensionality Reduction Based on Machine Learning Methods for PMSM Model Order Reduction," in IEEE Access, vol. 9, pp. 102345-102354, 2021, doi: 10.1109/ACCESS.2021.3095668.

[37] D. E. Pinto, A. -C. Pop, J. Kempkes and J. Gyselinck, "dq0-modeling of interior permanent-magnet synchronous machines for high-fidelity model order reduction," 2017 International Conference on Optimization of Electrical and Electronic Equipment (OPTIM) & 2017 Intl Aegean Conference on Electrical Machines and Power Electronics (ACEMP), Brasov, Romania, 2017, pp. 357-363, doi: 10.1109/OPTIM.2017.7974996.

[38] S. Ciceo, F. Chauvicourt, J. Gyselinck and C. Martis, "A comparative study of system-level PMSM models with either current or flux-linkage state variables used for vibro-acoustic computation," 2019 IEEE International Electric Machines & Drives Conference (IEMDC), San Diego, CA, USA, 2019, pp. 1881-1888, doi: 10.1109/IEMDC.2019.8785326.

[39] A. Gebregergis, M. H. Chowdhury, M. S. Islam, and T. Sebastian, "Modeling of permanent-magnet synchronous machine including torque

ripple effects," IEEE Transactions on Industry Applications, vol. 51, no. 1, pp. 232–239, Jan 2015.

[40] S. Rojas, M. A. Pérez, J. Rodríguez and H. Zelaya, "Torque ripple modeling of a permanent magnet synchronous motor," 2010 IEEE International Conference on Industrial Technology, Via del Mar, Chile, 2010, pp. 433-438, doi: 10.1109/ICIT.2010.5472761.

[41] M. R. Raia, A. -C. Pop and C. Martis, "Scalable abc-Modelling of Permanent Magnet Synchronous Machines for Model Order Reduction," 2019 IEEE Workshop on Electrical Machines Design, Control and Diagnosis (WEMDCD), Athens, Greece, 2019, pp. 83-88, doi: 10.1109/WEMDCD.2019.8887775.

[42] C. C. Aggarwal, Neural Networks and Deep Learning, Springer, 2018, NY, USA.

[43] S. Songa, L. Ge, S. Ma, and M. Zhang, "Accurate modeling of switched reluctance machine based on hybrid trained WNN," AIP Advances, vol. 4, no. 4, 2014.

[44] Y. Yan, J. Liang, T. Sun, J. Geng, Gang-Xie and D. Pan, "Torque Estimation and Control of PMSM Based on Deep Learning," 2019 22nd International Conference on Electrical Machines and Systems (ICEMS), Harbin, China, 2019, pp. 1-6.

[45] M. M. Saafan, A. Y. Haikal, S. F. Saraya, F. F.G. Areed, "Artificial Neural Network Control of Permanent Magnet Synchronous Motor," International Journal of Computer Applications, Volume 37– No.5, January 2012.

[46] M. Tahkola, J. Keränen, D. Sedov, M. F. Far and J. Kortelainen, "Surrogate Modeling of Electrical Machine Torque Using Artificial Neural Networks," in IEEE Access, vol. 8, pp. 220027-220045, 2020.

[47] H. Wu, S. Niu, Y. Zhang, X. Zhao and W. Fu, "Fast Magnetic Field Approximation Method for Simulation of Coaxial Magnetic Gears Using AI," in IEEE Journal of Emerging and Selected Topics in Industrial Electronics, vol. 4, no. 1, pp. 400-408, Jan. 2023, doi: 10.1109/JESTIE.2022.3185558.

[48] M. Kubat, An Introduction to Machine Learning, 2nd ed., Springer, 2017.

[49] S. Haykin, "Neural Networks and Learning Machines," vol. 3, 3rd ed. London, U.K.: Pearson Prentice-Hall, 2008.

[50] Koziel, S.; Leifsson, L.P. Surrogate-Based Modeling and Optimization: Applications in Engineering; Springer: New York, NY, USA, 2013.

[51] Yu, Hao and Bogdan M. Wilamowski , "Levenberg—Marquardt Training," in The Industrial Electronics Handbook ed. Bogdan M.

Wilamowski and J. David Irwin (Boca Raton: CRC Press, 28 Feb 2011), accessed 22 Mar 2021, Routledge Handbooks Online.

[52] R.C.P. Silva, Surrogate Problem Evaluation and Selection for Optimization with Expensive Function Evaluations, Ph.D. Dissertation, Department of Electrical and Computer Engineering, McGill University, Montreal, QC, Canada, 2018.

[53] L. Prechelt, Early Stopping - But When?, G. B. Orr and K.-R. Muller, Eds. Berlin, Germany: Springer, 1998.

[54] Silva, R.C.P.; Rahman, M.; Li, T.; Lowther, D.A. Surrogate-Based MOEA/D for Electric Motor Design With Scarce Function Evaluations. IEEE Trans. Magn. **2017**, 53, 7400704

[55] N. Bianchi and S. Bolognani, "Magnetic models of saturated interior permanent magnet motors based on finite element analysis," Conference Record of 1998 IEEE Industry Applications Conference. Thirty-Third IAS Annual Meeting (Cat. No.98CH36242), St. Louis, MO, USA, 1998, pp. 27-34 vol.1. Doi: 10.1109/IAS.1998.732255.

[56] D. E. Pinto, A.-C. Pop, J. Kempkes and J. Gyselinck, "Reduced-Order Eddy-Current Loss Modelling of Electrical Machines Using Lookup Tables Obtained via 2D Finite-Element," International Conference on Electrical Machines (ICEM), September 2018.

[57] M. Ruba, R. O. Nemes, S. M. Ciornei, C. Martis, A. Bouscayrol and H. Hedesiu, "Digital Twin Real-Time FPGA Implementation for Light Electric Vehicle Propulsion System Using EMR Organization," 2019 IEEE Vehicle Power and Propulsion Conference (VPPC), Hanoi, Vietnam, 2019, pp. 1-6, doi:10.1109/VPPC46532.2019.8952428

[58] S. Ciornei, R. Nemeş, M. Ruba, C. Marţiş and H. Hedeşiu, "Performance analysis of urban light electric vehicle propulsion system's multi-level modelling," 2020 IEEE International Conference on Automation, Quality and Testing, Robotics (AQTR), Cluj-Napoca, Romania, 2020, pp. 1-6, doi: 10.1109/AQTR49680.2020.912993.

[59] KC. Maliti, "Modelling and analysis of magnetic noise in squirrel-cage induction motors: doctoral dissertation," 2000.

[60] Gieras, J.F., Wang, C., & Lai, J.C. (2006). Noise of Polyphase Electric Motors (1st ed.). CRC Press. https://doi.org/10.1201/9781420027730

[61] H. Jordan, Electric motor silencer - formation and elimination of the noises in the electric motors. W. Giradet-Essen editor, 1950.

[62] H. Wang and K. Williams, "Vibrational Modes of Thick Cylinders of Finite Length," Journal of Sound and Vibration, vol. 191, no. 5, pp. 955-971, 1996.

[63] S. Ciceo, M. R. Raia, and C. Martis, "On the use of parametric sta-

tor models for electrical machine vibration computation," accepted at 2023 IEEE Transportation Electrification Conference and Expo, Asia-Pacific, Chiang Mai, Thailand.

[64] J. Roivainen, "Unit-wave response-based modeling of electromechanical noise and vibration of electrical machines," Ph.D. dissertation, Dept. Elect. Eng., Helsinki Univ. Technol., Helsinki, Finland, 2009.

[65] H. Yang and Y. Chen, "Influence of Radial Force Harmonics With Low Mode Number on Electromagnetic Vibration of PMSM," in IEEE Transactions on Energy Conversion, vol. 29, no. 1, pp. 38-45, March 2014, doi: 10.1109/TEC.2013.2290304.

[66] S. Wang, J. Hong, Y. Sun and H. Cao, "Analysis of Zeroth-Mode Slot Frequency Vibration of Integer Slot Permanent-Magnet Synchronous Motors," in IEEE Transactions on Industrial Electronics, vol. 67, no. 4, pp. 2954-2964, April 2020, doi: 10.1109/TIE.2019.2910046.

[67] H. Fang, D. Li, R. Qu and P. Yan, "Modulation Effect of Slotted Structure on Vibration Response in Electrical Machines," in IEEE Transactions on Industrial Electronics, vol. 66, no. 4, pp. 2998-3007, April 2019, doi: 10.1109/TIE.2018.2847639.

[68] W. Liang, J. Wang, P. C. -K. Luk and W. Fei, "Analytical Study of Stator Tooth Modulation on Electromagnetic Radial Force in Permanent Magnet Synchronous Machines," in IEEE Transactions on Industrial Electronics, vol. 68, no. 12, pp. 11731-11739, Dec. 2021, doi: 10.1109/TIE.2020.3029462.

[69] R. Pile, Y. Le Menach, J. Le Besnerais and G. Parent, "Study of the Combined Effects of the Air-Gap Transfer for Maxwell Tensor and the Tooth Mechanical Modulation in Electrical Machines," in IEEE Transactions on Magnetics, vol. 56, no. 1, pp. 1-4, Jan. 2020, Art no. 7502004, doi: 10.1109/TMAG.2019.2948228.

[70] A. -C. Pop, D. E. Pinto, J. Tüchsen and M. Koch, "Robustness to Large-Scale Mass Production Manufacturing Tolerances by Means of Sensitivity and Statistical Analysis for IPMSMs," in IEEE Transactions on Energy Conversion, vol. 35, no. 4, pp. 2201-2209, Dec. 2020, doi: 10.1109/TEC.2020.3004695.

[71] A. -C. Pop, Z. Cai and J. J. C. Gyselinck, "Machine-Learning Aided Multiobjective Optimization of Electric Machines— Geometric-Feasibility and Enhanced Regression Models," in IEEE Journal of Emerging and Selected Topics in Industrial Electronics, vol. 4, no. 3, pp. 844-854, July 2023, doi: 10.1109/JESTIE.2023.3252404.

[72] S. Giurgea, H. S. Zire and A. Miraoui, "Two-Stage Surrogate Model for Finite-Element-Based Optimization of Permanent-Magnet Syn-

chronous Motor," in IEEE Transactions on Magnetics, vol. 43, no. 9, pp. 3607-3613, Sept. 2007, doi: 10.1109/TMAG.2007.902348.

[73] G. Tsekouras, S. Kiartzis, A. G. Kladas and J. A. Tegopoulos, "Neural network approach compared to sensitivity analysis based on finite element technique for optimization of permanent magnet generators," in IEEE Transactions on Magnetics, vol. 37, no. 5, pp. 3618-3621, Sept. 2001, doi: 10.1109/20.952675.

[74] G. Bramerdorfer and A. -C. Zăvoianu, "Surrogate-Based Multi-Objective Optimization of Electrical Machine Designs Facilitating Tolerance Analysis," in IEEE Transactions on Magnetics, vol. 53, no. 8, pp. 1-11, Aug. 2017, Art no. 8107611, doi: 10.1109/TMAG.2017.2694802.

[75] Y. You, "Multi-Objective Optimal Design of Permanent Magnet Synchronous Motor for Electric Vehicle Based on Deep Learning," Applied Sciences, vol. 10, no. 2, p. 482, Jan. 2020, doi: 10.3390/app10020482.

[76] H. Dhulipati, E. Ghosh, S. Mukundan, P. Korta, J. Tjong and N. C. Kar, "Advanced Design Optimization Technique for Torque Profile Improvement in Six-Phase PMSM Using Supervised Machine Learning for Direct-Drive EV," in IEEE Transactions on Energy Conversion, vol. 34, no. 4, pp. 2041-2051, Dec. 2019, doi: 10.1109/TEC.2019.2933619.

[77] S. Ciceo, F. Chauvicourt, J. Gyselinck and C. Martis, "Data-Driven Electrical Machines Structural Model Using the Vibration Synthesis Method," in IEEE Transactions on Transportation Electrification, vol. 8, no. 3, pp. 3771-3781, Sept. 2022, doi: 10.1109/TTE.2022.3164644.

[78] M. H. Mohammadi, T. Rahman, R. C. P. Silva, B. Wang, K. Chang and D. A. Lowther, "Effect of Acoustic Noise on Optimal SynRM Design Regions," in IEEE Transactions on Magnetics, vol. 54, no. 3, pp. 1-4, March 2018, Art no. 8101304, doi: 10.1109/TMAG.2017.2760859.

[79] I. Ibrahim, R. Silva, M. H. Mohammadi, V. Ghorbanian and D. A. Lowther, "Surrogate-Based Acoustic Noise Prediction of Electric Motors," in IEEE Transactions on Magnetics, vol. 56, no. 2, pp. 1-4, Feb. 2020, Art no. 7509304, doi: 10.1109/TMAG.2019.2945407.

[80] V. Parekh, D. Flore and S. Schöps, "Deep Learning-Based Prediction of Key Performance Indicators for Electrical Machines," in IEEE Access, vol. 9, pp. 21786-21797, 2021, doi: 10.1109/ACCESS.2021.3053856.

[81] Towards Data Science. Available online: `https://towardsdatascience.com/how-not-to-use-machine-learning-for-time-s`

eries-forecasting-avoiding-the-pitfalls-19f9d7adf424. (Accessed on 28.11.2022).
[82] P. Heckbert, "Fourier Transforms and the Fast Fourier Transform (FFT) Algorithm", Course Notes, Computer Graphics 2, 15-463, Feb. 1995, Revised 27 Jan. 1998. Available online: https://www.cs.cmu.edu/afs/andrew/scs/cs/15-463/2001/pub/www/notes/fourier/fourier.pdf. (Accessed on 26.07.2023).
[83] Simcenter Nastran User's Guide
[84] Machine Learning in Python. Available online: https://scikit-learn.org/stable/. (Accessed on 28.11.2022).
[85] https://scikit-learn.org/stable/modules/cross_validation.html
[86] Towards Data Science. Available online: https://towardsdatascience.com/an-introduction-to-support-vector-regression-svr-a3ebc1672c2. (Accessed on 28.11. 2022).
[87] Towards Data Science. Available online: https://towardsdatascience.com/when-do-support-vector-machines-fail-3f23295ebef2. (Accessed on 9.01.2023).
[88] Machine Learning in Python. Available online: https://scikit-learn.org/stable/modules/generated/sklearn.svm.SVR.html (Accessed on 9.01.2023).
[89] Lee, J.A.; Verleysen, M. Nonlinear Dimensionality Reduction; Springer Science & Business Media: New York, NY, USA, 2007.
[90] Machine Learning in Python. Available online: https://scikit-learn.org/stable/modules/feature_selection.html. (Accessed on 9.01.2023).
[91] Towards Data Science. Available online: https://towardsdatascience.com/all-you-need-to-know-about-gradient-boosting-algorithm-part-1-regression-2520a34a502. (Accessed on 28.11.2022).
[92] KDnuggets. Available online: https://www.kdnuggets.com/2018/08/make-machine-learning-models-robust-outliers.html. (Accessed on 9.01.2023).
[93] Analytics India Magazine. Available online: https://analyticsindiamag.com/adaboost-vs-gradient-boosting-a-comparison-of-leading-boosting-algorithms/. (Accessed on 9.01.2023).
[94] Towards Data Science. Available online: https://towardsdatascience.com/understanding-gradient-boosting-machines-9be756fe76ab. (Accessed on 28.11.2022).
[95] Data Science. Available online: https://datascience.eu/machine-learning/regularization-in-machine-learning/. (Accessed on 9.01.2023).

[96] KDnuggets. Available online: https://www.kdnuggets.com/2022/08/avoid-overfitting.html. (Accessed on 9.01.2023).

[97] Chen, T.; Guestrin, C. Xgboost: A scalable tree boosting system. In Proceedings of the 22nd ACM SIGKDD International Conference on Knowledge Discovery and Data Mining (KDD '16), San Francisco, CA, USA, 13–17 August 2016; pp. 785–794.

[98] Machine Learning in Python. Available online: https://scikit-learn.org/stable/modules/gaussian_process.html. (Accessed on 28.11.2022).

[99] Rasmussen, C.E.; Williams, C.K.I. Gaussian Processes for Machine Learning; MIT Press: Cambridge, MA, USA, 2006.

[100] Seyed Mostafa, K.; Marquand, A. Normative modeling of neuroimaging data using scalable multi-task Gaussian processes. In International Conference on Medical Image Computing and Computer-Assisted Intervention; Springer: Cham, Switzerland, 2018.

[101] Xu, B.; Kuplicki, R.; Sen, S.; Paulus, M.P. The pitfalls of using Gaussian Process Regression for normative modeling. PLoS ONE **2021**, 16, e0252108. https://doi.org/10.1371/journal.pone.0252108.

[102] Towards Data Science. Available online: https://towardsdatascience.com/gaussian-process-regression-from-first-principles-833f4aa5f842. (Accessed on 9.01.2023).

[103] https://medium.com/@nutanbhogendrasharma/simple-sequence-prediction-with-lstm-69ff0f4d57cd. (Accessed on 9.01.2023).

[104] https://medium.com/@nutanbhogendrasharma/simple-sequence-prediction-with-lstm-69ff0f4d57cd. (Accessed on 9.01.2023).

[105] https://machinelearningmastery.com/tensorflow-tutorial-deep-learning-with-tf-keras/. (Accessed on 9.01.2023).

[106] https://www.aiplusinfo.com/blog/what-is-the-adam-optimizer-and-how-is-it-used-in-machine-learning/. (Accessed on 9.01.2023).

[107] https://scikit-learn.org/stable/modules/generated/sklearn.metrics.confusion_matrix.html. (Accessed on 1.09.2023).

[108] HEEDS MDO User Manual.

[109] Salameh, M.; Singh, S.; Li, S.; Krishnamurthy, M. Surrogate vibration modeling approach for design optimization of electric machines, IEEE Trans. Transp. Electrif. **2020**, 6, 1126–1133.

[110] Y. Duan and D. M. Ionel, "A Review of Recent Developments in Electrical Machine Design Optimization Methods With a Permanent-

Magnet Synchronous Motor Benchmark Study," in IEEE Transactions on Industry Applications, vol. 49, no. 3, pp. 1268-1275, May-June 2013, doi: 10.1109/TIA.2013.2252597.

[111] G. Bramerdorfer, J. A. Tapia, J. J. Pyrhönen and A. Cavagnino, "Modern Electrical Machine Design Optimization: Techniques, Trends, and Best Practices," in IEEE Transactions on Industrial Electronics, vol. 65, no. 10, pp. 7672-7684, Oct. 2018, doi: 10.1109/TIE.2018.2801805.

[112] J. Nägelkrämer, A. Heitmann and N. Parspour, "Multi-Objective Optimization of the Rotor Design to Improve the Acoustic Behavior of High Power Density Interior Permanent Magnet Synchronous Machines," International Electric Vehicle Symposium (EVS), 2017, Stuttgart.

[113] N. Lenin and S. Orloval, "Methods to Reduce the Cogging Torque in Permanent Magnet Synchronous Machines," in Electronics and Electrotechnics, vol. 23, no. 1, 2007.

[114] M. R. Raia, S. Ciceo, F. Chauvicourt and C. Martis, "Influence of Stator Teeth Harmonic Shaping on the Vibration Response of an Electrical Machine," 2020 International Conference and Exposition on Electrical And Power Engineering (EPE), Iasi, Romania, 2020, pp. 193-199, doi: 10.1109/EPE50722.2020.9305587.

[115] S. Ciceo, F. Chauvicourt, B. Varaticeanu, J. Gyselinck and C. Martis, "PMASynRM late design-stage rotor shape NVH optimization," 2020 IEEE ICEM, Gothenburg, August, 2020.

[116] A. Andersson and T. Thiringer , "Electrical machine acoustic noise reduction based on rotor surface modifications," 2016 IEEE Energy Conversion Congress and Exposition (ECCE), pp. 1-7, 2016.

[117] Y. Zeng, M. Cheng, G. Liu and W. Zhao, "Effects of Magnet Shape on Torque Capability of Surface-Mounted Permanent Magnet Machine for Servo Applications," in IEEE Transactions on Industrial Electronics, vol. 67, no. 4, pp. 2977-2990, April 2020.

[118] G.-W. Cho, W.-S. Jang, K.-B. Jang, and G.-T. Kim, "The Optimal Design of Fractional-slot SPM to Reduce Cogging Torque and Vibration," Journal of Electrical Engineering and Technology, vol. 7, no. 5, pp. 753–758, Sep. 2012.

[119] H. T. Canseven, I. Petrov and J. Pyrhonen, "Magnetic Asymmetry in Stator Tooth Tips of a High Specific Power PMSM," 2022 International Conference on Electrical Machines (ICEM), Valencia, Spain, 2022, pp. 1424-1429, doi: 10.1109/ICEM51905.2022.9910927.

[120] P. Ponomarev, I. Petrov and J. Pyrhönen, "Torque ripple reduction in double-layer 18/16 TC-PMSMs by adjusting teeth widths to min-

imize local saturation," 2014 International Conference on Electrical Machines (ICEM), Berlin, Germany, 2014, pp. 1461-1467, doi: 10.1109/ICELMACH.2014.6960374.

[121] A. E. Hoffer, I. Petrov, J. J. Pyrhönen, J. A. Tapia and G. Bramerdorfer, "Analysis of a Tooth-Coil Winding Permanent-Magnet Synchronous Machine With an Unequal Teeth Width," in IEEE Access, vol. 8, pp. 71512-71524, 2020, doi: 10.1109/ACCESS.2020.2987872.

[122] F. Momen, K. Rahman, Y. Son and P. Savagian, "Electrical propulsion system design of Chevrolet Bolt battery electric vehicle," 2016 IEEE Energy Conversion Congress and Exposition (ECCE), Milwaukee, WI, USA, 2016, pp. 1-8, doi: 10.1109/ECCE.2016.7855076.

[123] N. Chase, M. Rademacher, E. Goodman, R. Averill and R. Sidhu, "A Benchmark Study of Optimization Search Algorithms", Red Cedar Technology, MI, USA, pp. 1-15, 2010.

[124] M. B. Marinov, D. N. Nikolov, B. T. Ganev and T. S. Djamiykov, "Smart Multisensor Node for Remote Elevator Condition Monitoring," 2020 21st International Symposium on Electrical Apparatus & Technologies (SIELA), Bourgas, Bulgaria, 2020, pp. 1-4, doi: 10.1109/SIELA49118.2020.9167049.

[125] H. Henao et al., "Trends in Fault Diagnosis for Electrical Machines: A Review of Diagnostic Techniques," in IEEE Industrial Electronics Magazine, vol. 8, no. 2, pp. 31-42, June 2014, doi: 10.1109/MIE.2013.2287651.

[126] https://www.tibco.com/reference-center/what-is-predictive-maintenance. (Accesed on 1.09.2023).

[127] https://www.ibm.com/topics/predictive-maintenance (Accesed on 1.09.2023).

[128] H. Henao et al., "Trends in Fault Diagnosis for Electrical Machines: A Review of Diagnostic Techniques," in IEEE Industrial Electronics Magazine, vol. 8, no. 2, pp. 31-42, June 2014, doi: 10.1109/MIE.2013.2287651.

[129] I. O. Olalere, M. Dewa and B. Nleya, "Remote Condition Monitoring of Elevator's Vibration and Acoustics Parameters for Optimised Maintenance Using IoT Technology," 2018 IEEE Canadian Conference on Electrical & Computer Engineering (CCECE), Quebec, QC, Canada, 2018, pp. 1-4, doi: 10.1109/CCECE.2018.8447771.

[130] S. Feng, K. Niu, Y. Liang and Y. Ju, "Research on elevator intelligent monitoring and grading warning system," 2021 IEEE International Conference on Computer Science, Electronic Information Engineering and Intelligent Control Technology (CEI), Fuzhou, China, 2021, pp. 145-148, doi: 10.1109/CEI52496.2021.9574579.

[131] H. Van Der Auweraer, T. Tamarozzi, E. Risaliti, M. Sarrazin, J. Croes, B. Forrier, F. Naets, and W. Desmet, "Virtual sensing based on design engineering simulation models." ICEDyn2017, Date: 2017/07/03-2017/07/05, Location: Ericeira, Portugal. 2017.

[132] M. Čech, A. -J. Beltman and K. Ozols, "Digital Twins and AI in Smart Motion Control Applications," 2022 IEEE 27th International Conference on Emerging Technologies and Factory Automation (ETFA), Stuttgart, Germany, 2022, pp. 1-7, doi: 10.1109/ETFA52439.2022.9921533.

[133] http://www.metalpress-wireropes.com/products/lifts-and-elevators/elevator-ropes/198-8x19s-fc.. (Accessed on 1.09.2023)

[134] G. Ramos and R. Costa-Castelló, "Comparison of Different Repetitive Control Architectures: Synthesis and Comparison. Application to VSI Converters," Electronics, vol. 7, no. 12, p. 446, Dec. 2018, doi: 10.3390/electronics7120446.

[135] R. Fausti, M. Beschi, D. Colombo and A. Visioli, "Comparing repetitive control strategies in lift applications," 2022 IEEE 27th International Conference on Emerging Technologies and Factory Automation (ETFA), Stuttgart, Germany, 2022, pp. 1-6, doi: 10.1109/ETFA52439.2022.9921429.

[136] http://www.wireropeworks.com/pdf/EL_TB_04.pdf. (Accessed on 1.09.2023).

[137] https://www.sciencedirect.com/topics/engineering/capstan-equation (Accesed on 8.06.2023).

[138] Simcenter Amesim User Guide.

[139] https://www.premierelevatorcabs.com/3-issues-commonly-found-during-an-elevator-inspection/. (Accessed on 1.09.2023).

[140] https://elevatorworld.com/article/traction-sheave-maintenance/. (Accessed on 1.09.2023).

[141] https://www.mathworks.com/discovery/lstm.html. (Accessed on 1.09.2023).

[142] https://machinelearningmastery.com/gentle-introduction-long-short-term-memory-networks-experts/. (Accessed on 1.09.2023).

[143] https://towardsdatascience.com/dropout-in-neural-networks-47a162d621d9. (Accessed on 1.09.2023).

[144] https://www.geeksforgeeks.org/what-is-standardization-in-machine-learning/. (Accessed on 1.09.2023).

[145] https://scikit-learn.org/stable/modules/generated/skle

arn.preprocessing.StandardScaler.html. (Accesed 8.06.2023).
[146] https://machinelearningmastery.com/adam-optimization-algorithm-for-deep-learning/. (Accesed on 8.06.2023).
[147] https://towardsdatascience.com/understanding-confusion-matrix-a9ad42dcfd62. (Accesed on 1.09.2023).
[148] https://optuna.readthedocs.io/en/stable/reference/samplers.html. (Accesed 8.06.2023).

List of Figures

List of Tables

LIST OF PUBLICATIONS

Articles in international refereed journals

1. M. R. Raia, S. Ciceo, F. Chauvicourt, and C. Martis, "Multi-Attribute Machine Learning Model for Electrical Motors Performance Prediction," Applied Sciences, vol. 13, no. 3, p. 1395, Jan. 2023, doi: 10.3390/app13031395.
2. M. R. Raia, M. Ruba, R. O. Nemes and C. Martis, "Artificial Neural Network and Data Dimensionality Reduction Based on Machine Learning Methods for PMSM Model Order Reduction," in IEEE Access, vol. 9, pp. 102345-102354, 2021, doi: 10.1109/ACCESS.2021.3095668.
3. R. O. Nemeş, M. Ruba, M. R. Raia, C. Marţiş and C. A. Oprea, "X-in-the-Loop-Based High Accuracy Test Facility for Industrial Development of Electric Vehicles," in IEEE Transactions on Transportation Electrification, vol. 9, no. 2, pp. 2778-2791, June 2023.

Articles in proceedings of international conferences

1. M. R. Raia, S. Ciceo, F. Chauvicourt and C. Martis, "Influence of Stator Teeth Harmonic Shaping on the Vibration Response of an Electrical Machine," 2020 International Conference and Exposition on Electrical And Power Engineering (EPE), Iasi, Romania, 2020, pp. 193-199, doi: 10.1109/EPE50722.2020.9305587.
2. M. R. Raia, M. Ruba, C. Martis, C. Husar and G. M. Sirbu, "Battery electric vehicle (BEV) powertrain modelling and testing for real-time control prototyping platform integration," 2021 23rd European Conference on Power Electronics and Applications (EPE'21 ECCE Europe), Ghent, Belgium, 2021, pp. P.1-P.10, doi: 10.23919/EPE21ECCEEurope50061.2021.9570616.
3. M. R. Raia, M. Ruba, R. A. Inte, C. Martis, G. M. Sirbu and C. Husar, "Modelling and Virtual Testing of a Wound Rotor Synchronous Machine for Electrical Vehicles Propulsion System," 2021 International Aegean Conference on Electrical Machines and Power Electronics

(ACEMP) & 2021 International Conference on Optimization of Electrical and Electronic Equipment (OPTIM), Brasov, Romania, 2021, pp. 129-134.

4. M. R. Raia, A. -C. Pop and C. Martis, "Scalable abc-Modelling of Permanent Magnet Synchronous Machines for Model Order Reduction," 2019 IEEE Workshop on Electrical Machines Design, Control and Diagnosis (WEMDCD), Athens, Greece, 2019, pp. 83-88.

5. R. Nemes, S. Ciornei, R. Raia, M. Ruba, H. Hedesiu, C. Martis, C. Husar, M. Grovu, "Hardware in the Loop Testing of an Urban Electric Vehicle Model Supplied with Supercapacitors," 2021 International Aegean Conference on Electrical Machines and Power Electronics (ACEMP) & 2021 International Conference on Optimization of Electrical and Electronic Equipment (OPTIM), Brasov, Romania, 2021, pp. 123-128.

6. A. A. Pop, M. Ruba, R. O. Nemeş, R. Raia, C. Marţiş and C. Husar, "Benchmarking methods for parameters identification of supercapacitors using Typhoon HiL," 2022 IEEE 20th International Power Electronics and Motion Control Conference (PEMC), Brasov, Romania, 2022, pp. 167-173, doi: 10.1109/PEMC51159.2022.9962871.

7. M. Ruba, R. O. Nemeş, R. Raia, C. Marţiş, D. Zuber and C. Husar, "Hardware in the loop analysis of urban utility electric vehicle powered from supercapacitors," 2022 International Symposium on Power Electronics, Electrical Drives, Automation and Motion (SPEEDAM), Sorrento, Italy, 2022, pp. 838-843.

8. M. Ruba, R. O. Nemeş, T. Moldovan, R. Raia, C. Marţiş, C. Husar and M. Ciocan, "Validation of EMR simulation platform of a permanent magnet synchronous machine used for electric propulsion," 2021 IEEE Vehicle Power and Propulsion Conference (VPPC), Gijon, Spain, 2021, pp. 1-4, doi: 10.1109/VPPC53923.2021.9699226.

9. R. Nemeş, M. Ruba, R. Raia, C. Marţiş and H. Hedeşiu, "HiL testing of Li-Ion battery pack based on real-time virtual vehicle model," 2021 IEEE Vehicle Power and Propulsion Conference (VPPC), Gijon, Spain, 2021, pp. 1-6, doi: 10.1109/VPPC53923.2021.9699355.

10. M. R. Raia, S. Ciceo, F. Chauvicourt, and C. Martis, "Asymmetric stator slot opening geometry fro PMSM NVH Optimisation," accepted at IECON 2023, Singapore.

11. S. Ciceo, M. R. Raia, and C. Martis, "On the use of parametric stator models for electrical machine vibration computation," accepted

at 2023 IEEE Transportation Electrification Conference and Expo, Asia-Pacific, Chiang Mai, Thailand.

12. M. R. Raia, A. Ailincai, A. Baicoianu, C. Husar and C. Irimia, "Condition Monitoring of Industrial Elevators Based on Machine Learning Models" presented at ETFA 28th Annual Conference of the IEEE Industrial Electronics Society (IES), September 2023, Sinaia, Romania